# Arbitrary-wavelength, dynamic-strong-flow gyrokinetics

Amil Yograj Sharma

Doctor of Philosophy

University of Warwick

Department of Physics

February 2016

# Contents

# List of Tables

# List of Figures

# Acknowledgements

I would like to thank Ben McMillan, my supervisor, for providing the ideas that have shaped this work.

I would like to thank my family, friends, colleagues and the EPSRC for their support.

Computational facilities were provided by the MidPlus Regional Centre of Excellence for Computational Science, Engineering and Mathematics under EPSRC grant EP/K000128/1.

# Declaration

This thesis is submitted to the University of Warwick in support of my application for the degree of Doctor of Philosophy. It has been composed by myself and has not been submitted in any previous application for any degree. Parts of this thesis have been published by the author: Sharma and McMillan (2015a).

# Abstract

Gyrokinetics is a maximally optimal description of low-frequency magnetised plasma turbulence.

We present a generalisation of gyrokinetic theory that allows dynamic strong flows and is valid for arbitrary-wavelength electrostatic potential perturbations in slab magnetic geometry. We obtain a substantially simpler gyrocentre Lagrangian than that of Dimits (2010a,b). We present a symplectic strong-flow generalisation of gyrokinetic field theory such that, unlike Dimits (2010a,b), our Vlasov-Poisson system is manifestly conservative as, ultimately, we obtain it as a whole, directly from our gyrocentre particle Lagrangian (Scott and Smirnov, 2010). Despite the symplectic representation of our strong-flow theory, our Poisson equation is consistent with that for weak flows (Hahm, 1988) at all wavelengths and the fluid equation obtained from our Vlasov-Poisson system is consistent with fluid theory.

Again, despite our symplectic representation, we demonstrate numerical tractability by solving implicit dependences using an iterative scheme. Weak- and strong-flow code verification are performed in limits that admit analytic comparison.

Simulations show strong-flow symmetry breaking of the Kelvin-Helmholtz instability of a shear layer and blobs that manifest as asymmetries in the growth rate and propagation, respectively, that depend on the sign of the parallel vorticity.

# Abbreviations

| | |
|---|---|
| FLR | Finite-Larmor-radius |
| MHD | Magnetohydrodynamics |

# Chapter 1

# Introduction

An increasing population is leading to a net increase in global energy demand and climate change that cannot be tolerated. Fusion energy (EUROfusion, 2013) may be a pertinent future resource.

Fusion energy is the unconventional but superior harnessing of nuclear binding energy. The obstacles for its realisation include reactor material procurement and, for the leading tokamak magnetic confinement approach, *transport*.

Confined plasma fuels are associated with gradients in physical quantities and related instabilities and, on relatively small scales, microinstabilities and related microturbulence. This leads to energy transport and a loss of confinement (Horton, 1999).

An additional layer of complexity comes in the form of self-organisation (Diamond et al., 2005). As such, theoretical study is warranted. Simple, classical and neoclassical collisional transport theory are not appropriate (ITER, 1999b). A fundamental theoretical understanding of magnetised plasma dynamics is necessary.

## 1.1 Plasma theory

The relevant domain is that of classical electrodynamics. For simplicity, this thesis will consider electrostatic potential perturbations in slab magnetic geometry (Dubin et al., 1983; Dimits, 2010a). The appropriate equations are the coupled Lorentz force and Poisson equations. The numerical solution of these nonlinear equations for the Avogadro's number of particles found within a tokamak plasma is currently infeasible.

The description can be simplified by taking a more statistical approach and utilising a smooth particle probability density function or *distribution function*, which, in the absence of particle collisions, yields a coupled Vlasov-Poisson *kinetic* system.

Charged particles in a magnetic field undergo a helical *gyromotion* along magnetic field lines. The space-time scale of the tokamak confinement system is large compared to that of the gyromotion. This restricts direct numerical solution and necessitates further simplification of the kinetic description.

The characteristic frequency of tokamak microturbulence is small compared to that of the gyromotion. As a result, the gyromotion in the plane perpendicular to the magnetic field exhibits quasi-circular symmetry on the gyromotion timescale. This *gyrosymmetry* can be utilised to maximally optimise the theoretical description by keeping the physics to the minimum of what is required.

In relatively long-wavelength fields, the drifting of the particle gyration or *guiding* centre can be followed and the circular gyromotion adiabatically ignored. This guiding-centre theory (Cary and Brizard, 2009) can be generalised (Brizard and Hahm, 2007; Krommes, 2010) for arbitrary-wavelength perturbations by instead only following the drifting of the particle *gyrocentre*, as shown in Figure 1.1, and adiabatically ignoring the gyromotion due to the generalised field. This is described in the next section.

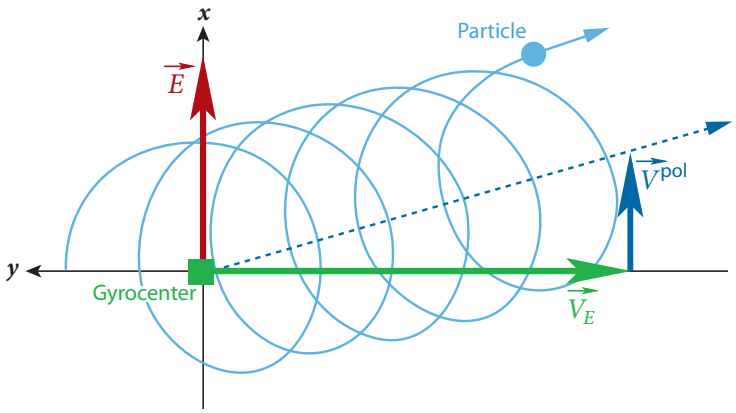


Figure 1.1: The drifting of an electrically charged particle gyrocentre with $\mathrm{E}\times\mathrm{B}$ and effective polarisation velocities, $\boldsymbol{V}_{\mathrm{E}}$ and $\boldsymbol{V}^{\mathrm{pol}}$, respectively, due to an electric field $\boldsymbol{E}$ in the plane $(x, y)$ perpendicular to the constant magnetic field: the electric field acceleration changes the radius of the otherwise circular gyromotion; indeed, tokamak conditions are such that the fluctuating electric field can be considered and treated as a perturbation (Krommes, 2012).

## 1.2 Gyrokinetics

We begin by defining the gyrokinetic ordering and, thereby, the gyrokinetic regime.

### 1.2.1 Ordering

The turbulence is characterised by fluctuations in density, temperature and electrostatic potential (Brizard and Hahm, 2007). The fluctuations themselves are characterised in terms of characteristic wavevector components and frequencies.

The gyrokinetic ordering parameter (Dimits et al., 1992) is

$$\epsilon_{\mathrm{gy}} \sim \omega\Omega^{-1} \sim k_{\parallel}\rho_{\mathrm{t}} \sim \rho_{\mathrm{t}}L_{\mathrm{B}}^{-1} \sim uv_{\mathrm{t}}^{-1} \ll 1, \tag{1.1}$$

where $\omega$ is the characteristic fluctuation frequency, $\Omega = |q|Bm^{-1}$ is the gyrofrequency, $q$ is the particle charge, $B$ is the magnetic field strength, $m$ is the

particle mass, $k_\parallel$ is the component of the characteristic fluctuation wavevector in the parallel direction with respect to the magnetic field, $\rho_\mathrm{t} = v_\mathrm{t}\Omega^{-1}$ is the thermal particle gyroradius, $v_\mathrm{t}$ is the thermal particle speed, $L_\mathrm{B}$ is the characteristic magnetic-field nonuniformity length scale and $u$ is the $\mathrm{E} \times \mathrm{B}$ drift speed associated with the fluctuating electrostatic potential. Fundamentally, it is a low-frequency ordering, and length scales and flows that are smaller in the perpendicular than parallel direction are implied by this. Additionally, the ordering is appropriate for tokamak magnetic geometry.

The state-of-the-art gyrokinetic description of particle dynamics is formulated in terms of manifestly conservative, differential-geometric classical mechanics (Brizard, 1990; Brizard and Hahm, 2007; Cary and Brizard, 2009). This is presented in the next subsection in terms of a guiding-centre electrostatic potential $\phi_\mathrm{gc}(\boldsymbol{x}, t) \sim 1$ that satisfies

$$k_\perp \rho_\mathrm{t} \sim \epsilon_\mathrm{gy}, \tag{1.2}$$

where $\boldsymbol{x}$ is the particle position, $t$ is time and $k_\perp$ is the perpendicular wavenumber.

### 1.2.2 Mechanics

The particle Lagrangian $L$ written as a 1-form is

$$\gamma = L\mathrm{d}t = \gamma_a \mathrm{d}z^a, \tag{1.3}$$

where

$$\gamma_a = (\gamma_t, \gamma_i), \tag{1.4}$$

$a \in \{0, \ldots, 6\}$,

$$\gamma_t = -h,$$

$h$ is the Hamiltonian, $\gamma_i$ are the symplectic components, $i \in \{1, \ldots, 6\}$, $z^a$ is a noncanonical seven-dimensional extended phase space coordinate (Cary and Littlejohn, 1983) and we have used Einstein notation. The invariance of the Lagrangian is apparent from this manifest covariance (1.3). Thus, coordinate choice is arbitrary and can be used to reveal symmetries that, by Noether's theorem[1], simplify the physical description.

We choose to express the particle Lagrangian in terms of coordinates $z = (\boldsymbol{x}, \boldsymbol{v})$ (Cary and Brizard, 2009),

$$\gamma = [\epsilon_{\mathrm{gy}}^{-1} \boldsymbol{A}(\boldsymbol{x}) + \boldsymbol{v}] \cdot \mathrm{d}\boldsymbol{x} - \left[\tfrac{1}{2}\boldsymbol{v}^2 + \phi_{\mathrm{gc}}\right] \mathrm{d}t, \tag{1.5}$$

where we indicate the order of each term, we use units, here and in the remainder of the thesis, such that

$$q = m = 1,$$

$\boldsymbol{A} \sim \epsilon_{\mathrm{gy}}^{-1}$ is the magnetic potential, $\boldsymbol{x} \sim \epsilon_{\mathrm{gy}}^{-1}$ and $\boldsymbol{v} \sim 1$ is the particle velocity. We may obtain our complete physical formalism from this Lagrangian (1.5) via the principle of least action and Noether's theorem. Thus, in order to simplify our complete physical formalism, we need only simplify our Lagrangian, as our complete physical formalism is obtained from our Lagrangian.

By general covariance, the Lagrangian is coordinate independent. Thus, let us write this Lagrangian (1.5) in the natural coordinates of gyromotion, the guiding-centre coordinates $Z = (\boldsymbol{X}, v_\parallel, \mu, \zeta)$, where

$$\boldsymbol{X} = \boldsymbol{x} - \boldsymbol{\rho} \sim \epsilon_{\mathrm{gy}}^{-1} \tag{1.6}$$

is the guiding-centre position (Figure 1.2), $\boldsymbol{\rho} = v_\perp \Omega^{-1}(\cos\zeta \hat{e}_1 - \sin\zeta \hat{e}_2) \sim \rho_{\mathrm{t}} \sim 1$ is the gyroradius, $v_\perp \sim v_{\mathrm{t}} \sim 1$ is the perpendicular speed, $\zeta$ is the gyroangle, $\hat{e}_1 = \hat{e}_2 \times \hat{\boldsymbol{b}}$, the hat denotes a unit vector, $\hat{\boldsymbol{b}}$ is the magnetic field unit vector, $v_\parallel \sim 1$ is the parallel velocity and $\mu = \frac{1}{2} v_\perp^2 \Omega^{-1} \sim 1$ is the magnetic moment.

[1] Noether's theorem relates the symmetries of a Lagrangian to its invariants (Krommes, 2010).

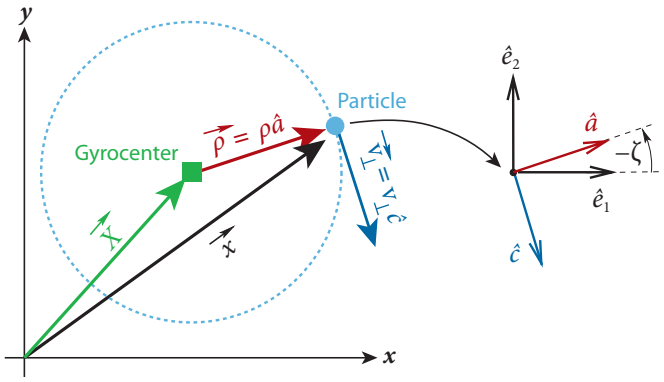


Figure 1.2: The guiding-centre or lowest-order-gyrocentre coordinates, as defined in Subsection 1.2.2, in the plane perpendicular to the magnetic field (Krommes, 2012).

The Lagrangian (1.5) in terms of coordinates $Z$ is

$$\Gamma = [\epsilon_{\rm gy}^{-1}\boldsymbol{A}(\boldsymbol{X}+\boldsymbol{\rho}) + v_\parallel\hat{\boldsymbol{b}} + \boldsymbol{v}_\perp]\cdot \mathrm{d}(\boldsymbol{X}+\boldsymbol{\rho}) - \left[\tfrac{1}{2}(v_\parallel\hat{\boldsymbol{b}}+\boldsymbol{v}_\perp)^2 + \phi_{\rm gc}(\boldsymbol{X}+\boldsymbol{\rho},t)\right]\mathrm{d}t, \tag{1.7}$$

where $\boldsymbol{v}_\perp = \boldsymbol{\rho}\times\boldsymbol{\Omega}$ is the perpendicular velocity and $\boldsymbol{\Omega} = \Omega\hat{\boldsymbol{b}}$.

This Lagrangian (1.7) is almost invariant under $\zeta$ rotation, that is, it has quasi-$\zeta$-symmetry. The potentials depend on $\boldsymbol{x}$, which in turn depends on $\boldsymbol{\rho}$, which itself depends on $\zeta$. However, cancellation and gauge transformation mean that, under the ordering used, the $\zeta$-dependence of the potentials is small as their variation over a distance $\rho_{\rm t}$ is small. Thus, we may write the Lagrangian (1.7) as

$$\Gamma = \Gamma_0 + \epsilon_{\rm gy}\Gamma_1,$$

where $\Gamma_0$ is $\zeta$-independent and $\Gamma_1$ is $\zeta$-dependent. The invariance of the Lagrangian is apparent from its manifest covariance (1.3). Thus, we may perturb the coordinate system in order to obtain a Lagrangian with exact $\zeta$-symmetry. This is achieved via a systematic, near-identity or *Lie* transformation of the Lagrangian. We detail this Lie transform in the next chapter.

The guiding-centre particle Lagrangian obtained up to first order in $\epsilon_{\rm gy}$ (1.1)

is

$$\Gamma = [\epsilon_{\rm gy}^{-1}\boldsymbol{A}(\boldsymbol{X}) + v_\parallel \hat{\boldsymbol{b}}] \cdot \mathrm{d}\boldsymbol{X} + \mu \mathrm{d}\zeta - \left(\tfrac{1}{2}v_\parallel^2 + \mu\Omega + \phi_{\rm gc}(\boldsymbol{X})\right)\mathrm{d}t. \tag{1.8}$$

This Lagrangian (1.8) depends on a five-dimensional phase space coordinate, thus, our complete physical formalism will now depend on a five-dimensional phase space coordinate. Additionally, by Noether's theorem, the $\zeta$-symmetry of the Lagrangian (1.8) corresponds to the adiabatic invariance of $\mu$.

We present the gyrocentre particle Lagrangian obtained within gyrokinetic theory in the next subsection.

### 1.2.3 Lagrangian

The gyrocentre particle Lagrangian is obtained by starting with a gyrokinetic (1.1), as opposed to guiding-centre (1.2), potential in the Lagrangian (1.5). An intermediate Lie transform is performed in the absence of the potential perturbation to obtain an equilibrium guiding-centre particle Lagrangian,

$$\gamma(z) \to \Gamma_{\rm eq}(Z) \to \bar{\Gamma}(\bar{Z}),$$

where the overbar denotes a gyrocentre quantity.

The gyrocentre particle Lagrangian up to second order in $\epsilon_{\rm gy}$ (1.1) (Brizard, 1989) is

$$\begin{aligned}\bar{\Gamma} = &[\epsilon_{\rm gy}^{-1}\boldsymbol{A}(\bar{\boldsymbol{X}}) + \bar{v}_\parallel \hat{\boldsymbol{b}}] \cdot \mathrm{d}\bar{\boldsymbol{X}} + \bar{\mu}\mathrm{d}\bar{\zeta} - \left[\tfrac{1}{2}\bar{v}_\parallel^2 + \bar{\mu}\Omega + \langle\phi_{\rm gy}(\boldsymbol{x},t)\rangle\right.\\ &\left. - \epsilon_{\rm gy}^2 \tfrac{1}{2}\Omega^{-1}(\Omega^{-1}\langle\bar{\boldsymbol{\nabla}}\tilde{\Phi}_{\rm gy} \times \hat{\boldsymbol{b}} \cdot \bar{\boldsymbol{\nabla}}\tilde{\phi}_{\rm gy}\rangle + \langle\tilde{\phi}_{\rm gy}^2\rangle_{,\bar{\mu}})\right]\mathrm{d}t,\end{aligned} \tag{1.9}$$

where

$$\langle\psi\rangle(\bar{\boldsymbol{X}},\bar{\mu},t) = (2\pi)^{-1}\int \mathrm{d}\bar{\zeta}\mathrm{d}^3x\,\delta(\bar{\boldsymbol{X}} + \bar{\boldsymbol{\rho}} - \boldsymbol{x})\psi(\boldsymbol{x},t) \tag{1.10}$$

is the gyroaverage for any function $\psi$, $\phi_{\rm gy}$ is the electrostatic potential that

satisfies the gyrokinetic ordering (1.1),

$$\tilde{\Phi}_{\mathrm{gy}} = \int \mathrm{d}\bar{\zeta}\tilde{\phi}_{\mathrm{gy}} \sim \epsilon_{\mathrm{gy}},$$

$$\tilde{\phi}_{\mathrm{gy}} = \phi_{\mathrm{gy}} - \langle\phi_{\mathrm{gy}}\rangle \sim \epsilon_{\mathrm{gy}}$$

and

$$\Psi_{,a} = \partial_a \Psi$$

for any function $\Psi$. This Lagrangian (1.9) depends on a five-dimensional phase space coordinate, thus, our complete physical formalism will now depend on a five-dimensional phase space coordinate. Additionally, by Noether's theorem, the $\bar{\zeta}$-symmetry of the Lagrangian (1.9) corresponds to the adiabatic invariance of $\bar{\mu}$.

By using a Fourier space representation of $\phi_{\mathrm{gy}}$, performing the integral in the expression for its gyroaverage (1.10) and Taylor expanding the resulting Bessel function, the gyroaveraged potential can be interpreted (Jolliet, 2009) as a finite-Larmor-radius (FLR) corrected gyrocentre potential,

$$\langle\phi_{\mathrm{gy}}\rangle = \bar{\phi}_{\mathrm{gy}} + \tfrac{1}{2}\Omega^{-1}\bar{\mu}\bar{\nabla}_{\perp}^{2}\bar{\phi}_{\mathrm{gy}} + \cdots \sim 1.$$

The gyrokinetic ordering (1.1) includes the weak-flow ordering

$$uv_{\mathrm{t}}^{-1} \sim \epsilon_{\mathrm{gy}}. \tag{1.11}$$

This ordering (1.11) cannot be applied to scrape-off-layer (ITER, 1999a), transport-barrier-containing and strongly rotating tokamak plasmas and many astrophysical plasmas due to the presence of strong flows (Artun and Tang, 1994), for which

$$uv_{\mathrm{t}}^{-1} \sim 1.$$

Strong-flow generalisations of gyrokinetics are described in the next section.

## 1.3 Strong flows

Strong-flow generalisations of gyrokinetics focused, initially, on symplectic (1.4) and, more recently, on Hamiltonian modifications.

### 1.3.1 Symplectic formulation

The work of Brizard (1995), Hahm (1996) and Hahm et al. (2009) reached its most general form with the work of Madsen (2010). Here, a strong-flow potential $\phi_\mathrm{s} \sim \epsilon_\mathrm{gy}^{-1}$ is accommodated by making the splitting,

$$\phi_\mathrm{s} = \phi_0(\boldsymbol{x}, t) + \phi_1(\boldsymbol{x}, t), \tag{1.12}$$

where $\phi_0 \sim \epsilon_\mathrm{gy}^{-1}$ is a long-wavelength electrostatic potential and $\phi_1 \sim \epsilon_\mathrm{gy}$ is a short-wavelength electrostatic potential.

Symplectic strong-flow theories redefine the velocity variable to be relative to a strong flow (Artun and Tang, 1994). The velocity variable $\boldsymbol{v}$ is redefined to be the velocity in a frame moving with a velocity $\boldsymbol{D} \sim 1$, where $\boldsymbol{D}$ is usually chosen to be an E × B drift velocity.

The gyrocentre Lagrangian up to second order (Madsen, 2010) is

$$\begin{aligned}
\bar{\Gamma} &= [\epsilon_\mathrm{gy}^{-1}\boldsymbol{A}(\bar{\boldsymbol{X}}) + \bar{v}_\parallel\hat{\boldsymbol{b}} + \bar{\boldsymbol{D}}(\bar{\boldsymbol{X}}, t)] \cdot \mathrm{d}\bar{\boldsymbol{X}} + \bar{\mu}\mathrm{d}\bar{\zeta} - \left[\tfrac{1}{2}\bar{v}_\parallel^2 + \bar{\mu}\Omega + \tfrac{1}{2}\bar{\boldsymbol{D}}^2 + \epsilon_\mathrm{gy}^{-1}\langle\phi_\mathrm{s}\rangle\right. \\
&\quad \left. -\epsilon_\mathrm{gy}^2\tfrac{1}{2}\Omega^{-1}(\Omega^{-1}\langle\bar{\boldsymbol{\nabla}}\tilde{\Phi}_1 \times \hat{\boldsymbol{b}} \cdot \bar{\boldsymbol{\nabla}}\tilde{\phi}_1\rangle + \langle\tilde{\phi}_1^2\rangle_{,\bar{\mu}})\right]\mathrm{d}t, \qquad (1.13) \\
\bar{\boldsymbol{D}} &= \Omega^{-1}\hat{\boldsymbol{b}} \times \bar{\boldsymbol{\nabla}}\bar{\phi}_0,
\end{aligned}$$

where we also redefine $\mu = \frac{1}{2}v_\perp^2\Omega^{-1} \sim 1$ to be the magnetic moment in the frame moving with a velocity $\boldsymbol{D}$, $\tilde{\Phi}_1 = \int \mathrm{d}\bar{\zeta}\tilde{\phi}_1 \sim \epsilon_\mathrm{gy}$ and $\tilde{\phi}_1 = \phi_1 - \langle\phi_1\rangle \sim \epsilon_\mathrm{gy}$.

A high-frequency symplectic strong-flow theory was formulated by Qin et al. (2007), however, this work has been criticised (Madsen, 2010) for an inconsistent application of a high-frequency ordering. Under a low-frequency ordering, Kawamura and Fukuyama (2008) included a higher-order term in a redefinition

of $\bar{\boldsymbol{D}}$,

$$\bar{\boldsymbol{D}}_{\mathrm{K}} = \bar{\boldsymbol{D}} + \epsilon_{\mathrm{gy}}\Omega^{-1}\hat{\boldsymbol{b}} \times (\bar{\boldsymbol{D}}_{\mathrm{K}} \cdot \bar{\boldsymbol{\nabla}})\bar{\boldsymbol{D}}_{\mathrm{K}} \sim 1. \tag{1.14}$$

The second term in $\bar{\boldsymbol{D}}_{\mathrm{K}}$ (1.14) is the centrifugal drift, which had appeared in the Euler-Lagrange equation of previous symplectic strong-flow theories. Both Qin et al. (2007) and Kawamura and Fukuyama (2008) have been criticised (Madsen, 2010) for being unnecessarily complex and specialised as a result of forgoing an intermediate, guiding-centre step.

The use of the two-component potential (1.12) is a partial, discontinuous treatment of the spectral range of tokamak turbulence,

$$\epsilon_{\mathrm{gy}} \lesssim k_{\perp}\rho_{\mathrm{t}} \lesssim 1. \tag{1.15}$$

Additionally, it introduces ambiguity to the conservative field theory and disallows the natural computation of a complete Vlasov-Poisson system.

A Hamiltonian, as opposed to symplectic, modification has also been considered. This is described in the next subsection.

### 1.3.2 Hamiltonian formulation

Miyato et al. (2009) employ the guiding-centre ordering (1.2). Their modified and simplified strong-flow guiding-centre Lagrangian up to second order is

$$\begin{aligned} \Gamma &= [\epsilon_{\mathrm{gy}}^{-1}\boldsymbol{A}(\boldsymbol{X}) + v_{\parallel}\hat{\boldsymbol{b}}] \cdot \mathrm{d}\boldsymbol{X} + \mu \mathrm{d}\zeta - \big(\tfrac{1}{2}v_{\parallel}^2 + \mu\Omega - \tfrac{1}{2}\boldsymbol{D}^2 \\ &\quad + \epsilon_{\mathrm{gy}}^{-1}\langle\phi_0\rangle\big)\mathrm{d}t, \\ \boldsymbol{D} &= \Omega^{-1}\hat{\boldsymbol{b}} \times \boldsymbol{\nabla}\phi_0(\boldsymbol{X}) \sim 1. \end{aligned} \tag{1.16}$$

The presence of $\boldsymbol{D}$ in the guiding-centre coordinate transformation,

$$\boldsymbol{X} = \boldsymbol{x} - \epsilon_{\mathrm{gy}}\Omega^{-1}\hat{\boldsymbol{b}} \times (\boldsymbol{v}_{\perp} + \boldsymbol{D}) + \mathcal{O}(\epsilon_{\mathrm{gy}}^2), \tag{1.17}$$

results in the absence of $\boldsymbol{D}$ in the symplectic part of the Lagrangian (1.16). The

symplectic part of this Lagrangian (1.16) is then identical in form to that of the weak-flow Lagrangian (1.9), unlike the symplectic strong-flow Lagrangian (1.13) of the previous subsection. This particular choice of guiding-centre coordinate transformation (1.17) also results in the term involving $\boldsymbol{D}$ in the Hamiltonian in this Lagrangian (1.16) appearing with the opposite sign to that in the Hamiltonian in the symplectic strong-flow Lagrangian (1.13) of the previous subsection. This, coupled with the absence of $\boldsymbol{D}$ from the symplectic part of the Lagrangian (1.16), results in this Hamiltonian strong-flow theory having fundamental weak-flow consistency. The potential appearing in this Lagrangian (1.16) only has a single component, unlike the symplectic strong-flow Lagrangian (1.13) of the previous subsection. As $\phi_1$ is not considered, all the terms associated with this potential component in the symplectic Lagrangian (1.13) of the previous subsection are absent in this Lagrangian (1.16).

We summarise pertinent gyrokinetic theories in Table 1.1.

| | Flows | Formulation | $k_\perp \rho_\mathrm{t}$ |
|---|---|---|---|
| Brizard (1989) | Weak | Hamiltonian | Arbitrary |
| Miyato et al. (2009) | Strong | Hamiltonian | $\mathcal{O}(\epsilon_\mathrm{gy})$ |
| Madsen (2010) | Strong | Symplectic | $\mathcal{O}(\epsilon_\mathrm{gy})$, $\mathcal{O}(1)$ |
| Dimits (2010a,b) | Strong | Symplectic | Arbitrary |

Table 1.1: A summary of pertinent gyrokinetic theories.

Experimental observations of tokamak plasma dynamics indicate that self-consistent interaction occurs on all length scales (Holzhauer et al., 1994; Andrew et al., 2008). The unified treatment (Dimits, 2010a,b) of the spectral range of tokamak turbulence (1.15) within strong-flow gyrokinetic theories is the subject of the next chapter.

# Chapter 2

# Gyrokinetic theory

In this chapter, we will present a generalisation of gyrokinetic theory that allows dynamic strong flows and is valid for arbitrary wavelength electrostatic potential perturbations in slab magnetic geometry. This generalisation is achieved by utilising a generalisation of the gyrokinetic ordering (1.1).

## 2.1 Ordering

The gyrokinetic ordering parameter (1.1) was originally (Hahm, 1988)

$$\epsilon_{\mathrm{gy}} \sim \omega\Omega^{-1} \sim k_{\parallel}\rho_{\mathrm{t}} \sim \rho_{\mathrm{t}}L_{\mathrm{B}}^{-1} \sim \phi_{\mathrm{gy}}T^{-1} \ll 1, k_{\perp}\rho_{\mathrm{t}} \sim 1, \tag{2.1}$$

where $T$ is the temperature, we use units, here and in the remainder of the thesis, such that

$$k_{\mathrm{B}} = 1$$

and $k_{\mathrm{B}}$ is the Boltzmann constant. This original ordering (2.1) was generalised (Dimits et al., 1992) by no longer ordering the quantity $\phi_{\mathrm{gy}}T^{-1}$, nor the quantity $k_{\perp}\rho_{\mathrm{t}}$, and instead ordering the size of the E $\times$ B flow associated with $\phi_{\mathrm{gy}}$ to be small compared to the thermal speed (1.1). This is the weak-flow gyrokinetic ordering (1.1). This weak-flow ordering (1.1) includes the treatment of the small-

amplitude gyroscale perturbations of the original ordering (2.1) but additionally allows larger-amplitude perturbations on larger perpendicular length scales.

The weak-flow ordering (1.1) can be further generalised (Dimits, 2010a,b) by no longer ordering the quantity $uv_{\mathrm{t}}^{-1}$ and instead ordering the vorticity. The strong-flow gyrokinetic ordering parameter used in this thesis is

$$\epsilon \sim \omega\Omega^{-1} \sim k_{\parallel}\rho_{\mathrm{t}} \sim \rho_{\mathrm{t}}L_{\mathrm{B}}^{-1} \sim u'\Omega^{-1} \ll 1, \tag{2.2}$$

where $u'$ represents the magnitude of the spatial derivatives of the E $\times$ B drift velocity associated with the fluctuating electrostatic potential. Given that, for a general magnetised plasma, $\omega \sim u'$, allowing $u'\Omega^{-1} > \epsilon$ would break the fundamental gyrosymmetry. This ordering (2.2) includes the treatment of the weak flows of the weak-flow ordering (1.1) but additionally allows larger flows on larger perpendicular length scales. This ordering (2.2) is compatible with the magnetohydrodynamics (MHD) ordering and similar to the Hasegawa-Mima ordering (Horton and Hasegawa, 1994), which additionally uses the cold-ion limit. $u'$ represents both the eddy turnover time and the nonlinear timescale.

For the accurate numerical solution of reduced plasma models, it is essential to have conservation properties (Cary and Brizard, 2009) and, specifically, intrinsic energetic consistency (Scott and Smirnov, 2010). The equation set of Dimits (2010a,b) has been criticised (Madsen, 2011) for not being manifestly conservative as, ultimately, it is not obtained as a whole, directly from the particle gyrocentre Lagrangian (Scott and Smirnov, 2010). Weak-flow gyrokinetics is a well established theoretical tool (Krommes, 2012) and the fluid limit is pertinent to turbulence analysis (Brizard and Hahm, 2007; Miyato et al., 2009). Symplectic strong-flow formulations, such a Dimits (2010a,b), have been criticised (Miyato et al., 2009; Scott and Smirnov, 2010; Scott, 2013) for a lack of weak-flow and fluid consistency. We address these points in this chapter.

We begin by deriving a preliminary, guiding-centre Lagrangian, where the fast gyromotion time scale has been decoupled (Brizard and Hahm, 2007), in

the next section.

## 2.2 Guiding-centre Lagrangian

Our particle Lagrangian in terms of coordinate $z$ (1.5) is

$$\gamma = [\boldsymbol{A}(\boldsymbol{x}) + \boldsymbol{v}] \cdot \mathrm{d}\boldsymbol{x} - \left[\tfrac{1}{2}\boldsymbol{v}^2 + \phi(\boldsymbol{x}, t)\right] \mathrm{d}t, \tag{2.3}$$

where $\phi$ is the electrostatic potential that satisfies our strong-flow ordering (2.2). As in Subsection 1.3.1, we redefine the particle velocity $\boldsymbol{v}$ as the velocity in a frame moving with a velocity $\boldsymbol{u}(\boldsymbol{x}, \boldsymbol{v}, t) \sim 1$ such that this Lagrangian (2.3) becomes

$$[\boldsymbol{A}(\boldsymbol{x}) + \boldsymbol{v} + \boldsymbol{u}] \cdot \mathrm{d}\boldsymbol{x} - \left[\tfrac{1}{2}(\boldsymbol{v} + \boldsymbol{u})^2 + \phi\right] \mathrm{d}t,$$

where we have redefined $\boldsymbol{v}$.

Given our simple, slab magnetic geometry, it is sufficient to perform a change of variables from our original coordinates $z$ to guiding-centre coordinates $Z$, as defined in the previous chapter, rather than use a Lie transform. This yields

$$\begin{aligned}\Gamma =&[\boldsymbol{A}(\boldsymbol{X} + \boldsymbol{\rho}) + v_\parallel \hat{\boldsymbol{b}} + \boldsymbol{v}_\perp + \boldsymbol{u}] \cdot (\mathrm{d}\boldsymbol{X} + \mathrm{d}\boldsymbol{\rho}) - (\tfrac{1}{2}v_\parallel^2 + \mu\Omega + \tfrac{1}{2}\boldsymbol{u}^2 + \langle\phi\rangle \\ &+ \delta_1\tilde{\phi})\mathrm{d}t,\end{aligned} \tag{2.4}$$

where we have used

$$\hat{\boldsymbol{b}} \cdot \boldsymbol{u} = 0$$

and

$$\delta_1\tilde{\phi} = \tilde{\phi} + \boldsymbol{v}_\perp \cdot \boldsymbol{u} = \tilde{\phi} + \boldsymbol{\rho} \cdot \boldsymbol{\Omega} \times \boldsymbol{u} \tag{2.5}$$

has a more general form than that of Dimits (2010a,b). We can expand the first term in square brackets in this Lagrangian (2.4) as $\boldsymbol{A}(\boldsymbol{X} + \boldsymbol{\rho}) = \boldsymbol{A}(\boldsymbol{X}) + (\boldsymbol{\rho} \cdot$

$\boldsymbol{\nabla})\boldsymbol{A}(\boldsymbol{X})$ and make use of a total derivative[1]

$$\mathrm{d}S = -\mathrm{d}\big\{\boldsymbol{\rho}\cdot\big[\big(1+\tfrac{1}{2}\boldsymbol{\rho}\cdot\boldsymbol{\nabla}\big)\boldsymbol{A}(\boldsymbol{X})+\boldsymbol{u}\big]\big\},$$

which is modified from that of Hahm (1988) and Dimits (2010a,b) by the presence of $\boldsymbol{u}$. This yields (Hahm, 1988)

$$\begin{aligned}\Gamma =&[\boldsymbol{A}(\boldsymbol{X})+v_\parallel\hat{\boldsymbol{b}}+\boldsymbol{u}]\cdot\mathrm{d}\boldsymbol{X}-\mathrm{d}\boldsymbol{X}\cdot\{\boldsymbol{\nabla}[\boldsymbol{A}(\boldsymbol{X})\cdot\boldsymbol{\rho}]-(\boldsymbol{\rho}\cdot\boldsymbol{\nabla})\boldsymbol{A}(\boldsymbol{X})\\&-\boldsymbol{\rho}\times[\boldsymbol{\nabla}\times\boldsymbol{A}(\boldsymbol{X})]\}-\boldsymbol{\rho}\cdot\mathrm{d}\boldsymbol{u}+\mu\mathrm{d}\zeta-(\tfrac{1}{2}v_\parallel^2+\mu\Omega+\tfrac{1}{2}\boldsymbol{u}^2+\langle\phi\rangle+\delta_1\tilde{\phi})\mathrm{d}t,\end{aligned}\tag{2.6}$$

where we have used $\boldsymbol{v}_\perp\cdot\mathrm{d}\boldsymbol{X}=\boldsymbol{\rho}\times[\boldsymbol{\nabla}\times\boldsymbol{A}(\boldsymbol{X})]\cdot\mathrm{d}\boldsymbol{X}$. By identifying the terms in curly brackets in this Lagrangian (2.6) as $[\boldsymbol{A}(\boldsymbol{X})\cdot\boldsymbol{\nabla}]\boldsymbol{\rho}+\boldsymbol{A}(\boldsymbol{X})\times(\boldsymbol{\nabla}\times\boldsymbol{\rho})=0$, we obtain our guiding-centre Lagrangian

$$\Gamma =[\boldsymbol{A}(\boldsymbol{X})+v_\parallel\hat{\boldsymbol{b}}+\boldsymbol{u}]\cdot\mathrm{d}\boldsymbol{X}-\boldsymbol{\rho}\cdot\mathrm{d}\boldsymbol{u}+\mu\mathrm{d}\zeta-(\tfrac{1}{2}v_\parallel^2+\mu\Omega+\tfrac{1}{2}\boldsymbol{u}^2+\langle\phi\rangle+\delta_1\tilde{\phi})\mathrm{d}t.\tag{2.7}$$

This Lagrangian (2.7) is modified from that of Hahm (1988) by the presence of $\boldsymbol{u}$.

We are now in a position to transform to gyrocentre coordinates. This is covered in the next section.

## 2.3 Gyrocentre Lagrangian

Using the strong-flow ordering (2.2), we can write the guiding-centre Lagrangian (2.7) as

$$\Gamma=\Gamma_0+\Gamma_1,$$

where

$$\Gamma_0=[\boldsymbol{A}(\boldsymbol{X})+v_\parallel\hat{\boldsymbol{b}}+\boldsymbol{u}]\cdot\mathrm{d}\boldsymbol{X}+\mu\mathrm{d}\zeta-(\tfrac{1}{2}v_\parallel^2+\mu\Omega+\tfrac{1}{2}\boldsymbol{u}^2+\langle\phi\rangle)\mathrm{d}t=\mathcal{O}(\epsilon^{-1})\tag{2.8}$$

[1]The addition of an arbitrary total derivative of a *gauge* to a Lagrangian does not change the Euler-Lagrange equation (Littlejohn, 1982).

is $\zeta$-independent and

$$\Gamma_1 = -\boldsymbol{\rho}\cdot \mathrm{d}\boldsymbol{u} - \delta_1\tilde{\phi}\mathrm{d}t = -\boldsymbol{\rho}\cdot(\mathrm{d}t\partial_t + \mathrm{d}\boldsymbol{X}\cdot\boldsymbol{\nabla} + \mathrm{d}\mu\partial_\mu)\boldsymbol{u} - \delta_1\tilde{\phi}\mathrm{d}t = \mathcal{O}(\epsilon) \quad (2.9)$$

is $\zeta$-dependent. Both $\Gamma_0$ (2.8) and $\Gamma_1$ (2.9) are modified from that of Hahm (1988) by the presence of $\boldsymbol{u}$ and $\langle\phi\rangle$.

The requirement

$$\delta_1\tilde{\phi} = \mathcal{O}(\epsilon)$$

is equivalent to restrictions on the possible choices for the $\zeta$-independent potential appearing in our guiding-centre Lagrangian (2.7) and $\boldsymbol{u}$ given by

$$\phi_{\mathrm{g}} - \phi(\boldsymbol{X}, t) \leq \mathcal{O}(\epsilon) \quad (2.10)$$

and

$$\boldsymbol{u} - \Omega^{-1}\hat{\boldsymbol{b}}\times\boldsymbol{\nabla}\phi(\boldsymbol{X}, t) \leq \mathcal{O}(\epsilon), \quad (2.11)$$

respectively, where $\phi_{\mathrm{g}}$ is a general $\zeta$-independent potential. Some possible choices for $\phi_{\mathrm{g}}$ and $\boldsymbol{u}$ that satisfy the restrictions (2.10) and (2.11) are $\phi_{\mathrm{g}} = \phi(\boldsymbol{X}, t)$,

$$\phi_{\mathrm{g}} = \langle\phi\rangle,$$

$\boldsymbol{u} = \Omega^{-1}\hat{\boldsymbol{b}}\times\boldsymbol{\nabla}\phi(\boldsymbol{X}, t)$ and

$$\boldsymbol{u} = \Omega^{-1}\hat{\boldsymbol{b}}\times\boldsymbol{\nabla}\langle\phi\rangle. \quad (2.12)$$

We will choose $\boldsymbol{u}$ to take this latter form (2.12). In addition, $\boldsymbol{u}$ must satisfy the condition

$$\partial_\tau\boldsymbol{u} = (\partial_t + \boldsymbol{u}\cdot\boldsymbol{\nabla})\boldsymbol{u} \sim \epsilon^2,$$

where $\tau$ corresponds to the time variable in the frame moving with a velocity $\boldsymbol{u}$ (Artun and Tang, 1994).

We compute our gyrocentre Lagrangian systematically via Lagrangian Lie

perturbation theory (Littlejohn, 1982, 1983; Cary and Littlejohn, 1983). The Lie transform used proceeds order by order in $\epsilon$ (2.2) and is given by the operator

$$\mathsf{T}^{\pm 1} = \exp\left(\pm \sum_{n=1}^{\infty} \epsilon^n \mathcal{L}_n\right), \tag{2.13}$$

where $\mathcal{L}_n$ are the Lie derivative operators,

$$\mathcal{L}_n \Gamma = g_n^a \omega_{ab} \mathrm{d}z^b,$$

$$\Gamma = \sum_{n=0}^{\infty} \epsilon^n \Gamma_n,$$

$g_n^a$ are the arbitrary *generators*,

$$\omega_{ab} = 2\Gamma_{[b,a]} \tag{2.14}$$

is the Lagrange matrix and $\Gamma_{[b,a]} = \frac{1}{2}(\Gamma_{b,a} - \Gamma_{a,b})$. By convention (Littlejohn, 1982), $\mathsf{T}^{-1}$ is applied to $\Gamma$,

$$\bar{\Gamma} = \mathsf{T}^{-1}\Gamma. \tag{2.15}$$

For the special case of the perturbation being solely resident within the Hamiltonian, Hamiltonian Lie perturbation theory (Cary, 1981) is sufficient. Pertinent examples of the use of Hamiltonian and Lagrangian Lie perturbation theory that admit comparison are Hahm et al. (1988) and Hahm (1988), respectively.

We start by computing the lowest-nontrivial-order part of the gyrocentre Lagrangian in the next subsection.

### 2.3.1 First order

The first-order part of the gyrocentre Lagrangian in terms of the Lie transform (2.15) is

$$\bar{\Gamma}_1 = \Gamma_1 - \mathcal{L}_1\Gamma_0 + \mathrm{d}S_1 \tag{2.16}$$

$$=\Gamma_1 - g_1^a \omega_{0ab} \mathrm{d}Z^b + \mathrm{d}S_1,$$

where

$$\mathrm{d}S_1 = \mathrm{d}Z^a \partial_a S_1$$

and $S_1$ is the first-order part of a gauge. We can compute the non-zero Lagrange matrix (2.14) components of $\Gamma_0$ (2.8) as

$$\begin{aligned}
&\omega_{0X_{i'}X_{j'}} = \Gamma_{0X_{j'},X_{i'}} - \Gamma_{0X_{i'},X_{j'}} = (A+u)_{j',X_{i'}} - (A+u)_{i',X_{j'}} = \epsilon_{i'j'k'}\Omega^*_{k'},\\
&\omega_{0\boldsymbol{X}\mu} = -\boldsymbol{u}_{,\mu},\\
&\omega_{0\boldsymbol{X}t} = -\boldsymbol{\nabla}\langle\phi\rangle - \boldsymbol{u}\times(\boldsymbol{\nabla}\times\boldsymbol{u}) - (\boldsymbol{u}\cdot\boldsymbol{\nabla}+\partial_t)\boldsymbol{u},\\
&\omega_{0\mu t} = -\langle\phi\rangle_{,\mu} - \boldsymbol{u}\cdot\boldsymbol{u}_{,\mu} - \Omega,\\
&\omega_{0\boldsymbol{X}v_\parallel} = -\hat{\boldsymbol{b}},\\
&\omega_{0v_\parallel t} = -v_\parallel,\\
&\omega_{0\mu\zeta} = 1,
\end{aligned} \tag{2.17}$$

where $i', j', k' \in \{1,2,3\}$, $\epsilon_{i'j'k'}$ is the three-dimensional Levi-Civita pseudotensor,

$$\boldsymbol{\Omega}^* = \boldsymbol{\Omega} + \boldsymbol{\nabla}\times\boldsymbol{u}, \tag{2.18}$$

and we have used $\frac{1}{2}\boldsymbol{\nabla}\boldsymbol{u}^2 = \boldsymbol{u}\times(\boldsymbol{\nabla}\times\boldsymbol{u}) + (\boldsymbol{u}\cdot\boldsymbol{\nabla})\boldsymbol{u}$. We can then write

$$\Gamma_1 = (-\boldsymbol{\rho}\cdot\boldsymbol{\nabla}\boldsymbol{u})\cdot\mathrm{d}\boldsymbol{X} - \boldsymbol{\rho}\cdot\boldsymbol{u}_{,\mu}\mathrm{d}\mu - (\boldsymbol{\rho}\cdot\boldsymbol{u}_{,t} + \delta_1\tilde{\phi})\mathrm{d}t,$$

$$\begin{aligned}
-g_1^a\omega_{0ab}\mathrm{d}Z^b =& (g_1^{\boldsymbol{X}}\times\boldsymbol{\Omega}^* - g_1^\mu\boldsymbol{u}_{,\mu})\cdot\mathrm{d}\boldsymbol{X} + (g_1^{\boldsymbol{X}}\boldsymbol{u}_{,\mu} + g_1^\zeta)\mathrm{d}\mu - g_1^\mu\mathrm{d}\zeta\\
&+ \{g_1^{\boldsymbol{X}}\cdot[\boldsymbol{\nabla}\langle\phi\rangle + \boldsymbol{u}\times(\boldsymbol{\nabla}\times\boldsymbol{u})] + g_1^\mu(\langle\phi\rangle_{,\mu} + \boldsymbol{u}\cdot\boldsymbol{u}_{,\mu} + \Omega)\}\mathrm{d}t\\
&+ \mathcal{O}(\epsilon^3)
\end{aligned}$$

and

$$\mathrm{d}S_1 = \boldsymbol{\nabla}S_1\cdot\mathrm{d}\boldsymbol{X} + S_{1,v_\parallel}\mathrm{d}v_\parallel + S_{1,\mu}\mathrm{d}\mu + S_{1,\zeta}\mathrm{d}\zeta + S_{1,t}\mathrm{d}t,$$

where we have chosen

$$g_1^{v_\parallel} = g_1^t = 0,$$

as in Hahm (1988).

We may solve for the first-order generator in terms of the first-order gauge such that the gyrocentre Lagrangian is composed solely of a time component at first order. This yields the non-zero first-order generators

$$\begin{aligned} g_1^{\boldsymbol{X}} &= \Omega^{-1}[\boldsymbol{\rho}\cdot(\hat{\boldsymbol{b}}\times\boldsymbol{\nabla})\boldsymbol{u} + \boldsymbol{\nabla}S_1\times\hat{\boldsymbol{b}}], \\ g_1^{\mu} &= S_{1,\zeta}, \\ g_1^{\zeta} &= \boldsymbol{\rho}\cdot\boldsymbol{u}_{,\mu} - S_{1,\mu}, \end{aligned}$$

where, as for the case for weak flows, $\hat{\boldsymbol{b}}\cdot g_1^{\boldsymbol{X}} = 0$. The first-order part of the gyrocentre Lagrangian is then

$$\bar{\Gamma}_1 = (-\delta_1\tilde{\phi} + \Omega S_{1,\zeta})\mathrm{d}t + \Gamma_2,$$

where

$$\begin{aligned} \Gamma_2 &= [g_1^{\boldsymbol{X}}\times(\boldsymbol{\nabla}\times\boldsymbol{u}) - g_1^{\mu}\boldsymbol{u}_{,\mu}]\cdot\mathrm{d}\boldsymbol{X} + g_1^{\boldsymbol{X}}\boldsymbol{u}_{,\mu}\mathrm{d}\mu + \{g_1^{\boldsymbol{X}}\cdot\boldsymbol{u}\times(\boldsymbol{\nabla}\times\boldsymbol{u}) + g_1^{\mu}(\langle\phi\rangle_{,\mu} \\ &\quad + \boldsymbol{u}\cdot\boldsymbol{u}_{,\mu}) + (\partial_t + \boldsymbol{u}\cdot\boldsymbol{\nabla})(S_1 - \boldsymbol{\rho}\cdot\boldsymbol{u})\}\mathrm{d}t \\ &= \mathcal{O}(\epsilon^2) \end{aligned}$$

and, as in Dimits (2010a,b), we have used

$$(\partial_t + \boldsymbol{u}\cdot\boldsymbol{\nabla})S_1 \sim \epsilon^2,$$

which is validated upon choosing the first-order part of the gauge.

We choose the first-order part of the gauge such that the gyrocentre Lagrangian is gyroangle independent at first order or, equivalently, such that it cancels with the first-order gyroangle-dependent terms in the time component

of the Lagrangian. This yields

$$S_1 = \Omega^{-1}\delta_1\tilde{\Phi}, \tag{2.19}$$

where $\delta_1\tilde{\Phi} = \int \mathrm{d}\zeta\delta_1\tilde{\phi}$, and we have that the first-order part of our gyrocentre Lagrangian is

$$\bar{\Gamma}_1 = \Gamma_2.$$

By substituting for the first-order gauge (2.19), we may now write our non-zero first-order generators as

$$\begin{aligned} g_1^{\boldsymbol{X}} &= \Omega^{-2}\boldsymbol{\nabla}\tilde{\Phi}\times\hat{\boldsymbol{b}}, \\ g_1^{\mu} &= \Omega^{-1}\delta_1\tilde{\phi}, \\ g_1^{\zeta} &= \boldsymbol{\rho}\cdot\boldsymbol{u}_{,\mu} - \Omega^{-1}\delta_1\tilde{\Phi}_{,\mu} = -\Omega^{-1}\tilde{\Phi}_{,\mu} - \boldsymbol{u}\cdot\boldsymbol{\rho}_{,\mu}. \end{aligned} \tag{2.20}$$

Our first-order spatial generator is the same as that for weak flows. For $k_\perp\rho_\mathrm{t} \sim \epsilon$, our $g_1^\mu$ and $g_1^\zeta$ (2.20) are small compared to those for weak flows. This represents an enhancement of the Lagrangian Lie perturbation theory.

In order to obtain the crucial polarisation physics (Lee, 1983), the Lagrangian Lie perturbation theory must proceed to second order. We will do so in the next subsection.

### 2.3.2 Second order

The second-order part of the gyrocentre Lagrangian in terms of the Lie transform (2.15) is

$$\bar{\Gamma}_2 = \Gamma_2 - \mathcal{L}_1\Gamma_1 + \left(\tfrac{1}{2}\mathcal{L}_1^2 - \mathcal{L}_2\right)\Gamma_0 + \mathrm{d}S_2, \tag{2.21}$$

where

$$\mathrm{d}S_2 = \mathrm{d}Z^a\partial_a S_2$$

and $S_2$ is the second-order part of the gauge. We can use the expression for the first-order part of the gyrocentre Lagrangian written in terms of the Lie

transform (2.16) to write this expression (2.21) as

$$\bar{\Gamma}_2 = \Gamma_2 - \tfrac{1}{2}\mathcal{L}_1\Gamma_1 - \mathcal{L}_2\Gamma_0 + \mathrm{d}S_2 + O(\epsilon^3) = \Gamma_2 - \tfrac{1}{2}g_1^a\omega_{1ab}\mathrm{d}Z^b - g_2^a\omega_{0ab}\mathrm{d}Z^b + \mathrm{d}S_2, \tag{2.22}$$

where we have used $\mathcal{L}_1\mathrm{d}S_1 = 0$.

We may compute the Lagrange matrix (2.14) components of $\Gamma_1$ as

$$\begin{aligned}
\omega_{1\boldsymbol{X}\mu} &= \boldsymbol{\nabla u}\cdot\boldsymbol{\rho}_{,\mu},\\
\omega_{1\boldsymbol{X}\zeta} &= \boldsymbol{\rho}_{,\zeta}\cdot\boldsymbol{\nabla u},\\
\omega_{1\boldsymbol{X}t} &= -\boldsymbol{\nabla}\delta_1\tilde{\phi},\\
\omega_{1\mu\zeta} &= \boldsymbol{\rho}_{,\zeta}\cdot\boldsymbol{u}_{,\mu},\\
\omega_{1\mu t} &= -\boldsymbol{u}_{,t}\cdot\boldsymbol{\rho}_{,\mu} - \delta_1\tilde{\phi}_{,\mu},\\
\omega_{1\zeta t} &= -(\boldsymbol{\rho}\cdot\boldsymbol{u}_{,t} + \delta_1\tilde{\phi})_{,\zeta}.
\end{aligned}$$

We may then write the terms in the expression for the second order part of the gyrocentre Lagrangian (2.22) as

$$\begin{aligned}
-\tfrac{1}{2}g_1^a\omega_{1ab}\mathrm{d}Z^b =& \tfrac{1}{2}\{g_1^a\boldsymbol{\rho}_{,a}\cdot\boldsymbol{\nabla u}\cdot\mathrm{d}\boldsymbol{X} + (g_1^\zeta\boldsymbol{\rho}_{,\zeta}\cdot\boldsymbol{u}_{,\mu} - g_1^{\boldsymbol{X}}\cdot\boldsymbol{\nabla u}\cdot\boldsymbol{\rho}_{,\mu})\mathrm{d}\mu - g_1^a\boldsymbol{\rho}_{,\zeta}\cdot\boldsymbol{u}_{,a}\mathrm{d}\zeta\\
&+ [g_1^{\boldsymbol{X}}\cdot\boldsymbol{\nabla}\delta_1\tilde{\phi} + g_1^\mu(\boldsymbol{u}_{,t}\cdot\boldsymbol{\rho}_{,\mu} + \delta_1\tilde{\phi}_{,\mu}) + g_1^\zeta(\boldsymbol{\rho}\cdot\boldsymbol{u}_{,t} + \delta_1\tilde{\phi})_{,\zeta}]\mathrm{d}t\},
\end{aligned}$$

$$-g_2^a\omega_{0ab}\mathrm{d}Z^b = g_2^{\boldsymbol{X}}\times\boldsymbol{\Omega}\cdot\mathrm{d}\boldsymbol{X} + g_2^\zeta\mathrm{d}\mu - g_2^\mu\mathrm{d}\zeta + (g_2^{\boldsymbol{X}}\cdot\boldsymbol{\nabla}\langle\phi\rangle + g_2^\mu\Omega)\mathrm{d}t + \mathcal{O}(\epsilon^3)$$

and

$$\mathrm{d}S_2 = \boldsymbol{\nabla}S_2\cdot\mathrm{d}\boldsymbol{X} + S_{2,v_\parallel}\mathrm{d}v_\parallel + S_{2,\mu}\mathrm{d}\mu + S_{2,\zeta}\mathrm{d}\zeta + S_{2,t}\mathrm{d}t,$$

where we have chosen

$$g_2^{v_\parallel} = g_2^t = 0.$$

We may solve for the second-order generator in terms of the second-order gauge such that the gyrocentre Lagrangian is composed solely of a time compo-

nent at second order. This yields the non-zero second-order generators

$$
\begin{aligned}
g_2^{\boldsymbol{X}} &= \Omega^{-1}\big[g_1^{\boldsymbol{X}} \times (\boldsymbol{\nabla}\times\boldsymbol{u}) - g_1^{\mu}\boldsymbol{u}_{,\mu} + \tfrac{1}{2}g_1^{a}\boldsymbol{\rho}_{,a}\cdot\boldsymbol{\nabla}\boldsymbol{u} + \boldsymbol{\nabla}S_2\big]\times\hat{\boldsymbol{b}},\\
g_2^{\mu} &= S_{2,\zeta} - \tfrac{1}{2}g_1^{a}\boldsymbol{\rho}_{,\zeta}\cdot\boldsymbol{u}_{,a},\\
g_2^{\zeta} &= -[g_1^{\boldsymbol{X}}\boldsymbol{u}_{,\mu} + \tfrac{1}{2}(g_1^{\zeta}\boldsymbol{\rho}_{,\zeta}\cdot\boldsymbol{u}_{,\mu} + g_1^{\boldsymbol{X}}\cdot\boldsymbol{\nabla}\boldsymbol{u}\cdot\boldsymbol{\rho}_{,\mu}) + S_{2,\mu}].
\end{aligned}
$$

At this point, several cancellations are facilitated as a result of having chosen $\boldsymbol{u}$ to be the E×B drift velocity associated with the $\zeta$-independent potential that appears in our guiding-centre Lagrangian (2.7). For the particular choice of our second order generator, the second-order part of the gyrocentre Lagrangian is

$$
\begin{aligned}
\bar{\Gamma}_2 =& \big[g_1^{\mu}\langle\phi\rangle_{,\mu} + (\partial_t + \boldsymbol{u}\cdot\boldsymbol{\nabla})(S_1 - \boldsymbol{\rho}\cdot\boldsymbol{u}) + \tfrac{1}{2}g_1^{a}(\delta_1\tilde{\phi}_{,a} - \Omega\boldsymbol{\rho}_{,\zeta}\cdot\boldsymbol{u}_{,a}) + \Omega S_{2,\zeta}\big]\mathrm{d}t\\
&+ \mathcal{O}(\epsilon^3),
\end{aligned}
$$

where we have used

$$
\tfrac{1}{2}g_1^{a}\boldsymbol{\rho}_{,a}\cdot(\partial_t + \boldsymbol{u}\cdot\boldsymbol{\nabla})\boldsymbol{u} \sim (\partial_t + \boldsymbol{u}\cdot\boldsymbol{\nabla})S_2 \sim \epsilon^3.
$$

We now choose the second-order gauge such that the second-order part of the gyrocentre Lagrangian is gyroangle independent. This yields

$$
\begin{aligned}
\bar{\Gamma}_2 =& \tfrac{1}{2}\langle g_1^{a}(\delta_1\tilde{\phi}_{,a} - \Omega\boldsymbol{\rho}_{,\zeta}\cdot\boldsymbol{u}_{,a})\rangle\mathrm{d}t\\
=& \big(\tfrac{1}{2}\langle g_1^{\boldsymbol{X}}\cdot\boldsymbol{\nabla}\tilde{\phi}\rangle + \tfrac{1}{2}\Omega^{-1}\langle\delta_1\tilde{\phi}^2\rangle_{,\mu} + \hat{\boldsymbol{b}}\times\langle\delta_1\tilde{\phi}\boldsymbol{\rho}\rangle\cdot\boldsymbol{u}_{,\mu}\big)\mathrm{d}t,
\end{aligned}
\tag{2.23}
$$

where we have used the first-order generators (2.20) and expanded one of the factors of $\delta_1\tilde{\phi}$ (2.5). We can also expand the remaining factors of $\delta_1\tilde{\phi}$ (2.5) in this Lagrangian (2.23) to yield

$$
\begin{aligned}
\bar{\Gamma}_2 =& \big(\tfrac{1}{2}\langle g_1^{\boldsymbol{X}}\cdot\boldsymbol{\nabla}\tilde{\phi}\rangle + \tfrac{1}{2}\Omega^{-1}\langle\tilde{\phi}^2\rangle_{,\mu} - \boldsymbol{u}\cdot\hat{\boldsymbol{b}}\times\langle\tilde{\phi}\boldsymbol{\rho}\rangle_{,\mu} + \tfrac{1}{2}\boldsymbol{u}^2\big)\mathrm{d}t\\
=& \big(\tfrac{1}{2}\langle g_1^{\boldsymbol{X}}\cdot\boldsymbol{\nabla}\tilde{\phi}\rangle + \tfrac{1}{2}\Omega^{-1}\langle\tilde{\phi}^2\rangle_{,\mu} - \tfrac{1}{2}\boldsymbol{u}^2\big)\mathrm{d}t,
\end{aligned}
\tag{2.24}
$$

where we have used

$$\boldsymbol{u} = \hat{\boldsymbol{b}} \times \langle \tilde{\phi} \boldsymbol{\rho} \rangle_{,\mu}$$

and the only difference between this form of the second-order part of the gyrocentre Lagrangian and that for weak flows is the presence of $\boldsymbol{u}$.

Our gyrocentre Lagrangian up to second order is then

$$\begin{aligned} \bar{\Gamma} =& [\boldsymbol{A}(\bar{\boldsymbol{X}}) + \bar{v}_{\parallel} \hat{\boldsymbol{b}}] \cdot \mathrm{d}\bar{\boldsymbol{X}} + \bar{\mu} \mathrm{d}\bar{\zeta} - \big( \tfrac{1}{2} \bar{v}_{\parallel}^2 + \bar{\mu} \Omega + \langle \phi \rangle - \tfrac{1}{2} \langle g_1^{\bar{\boldsymbol{X}}} \cdot \bar{\boldsymbol{\nabla}} \tilde{\phi} \rangle \\ & - \tfrac{1}{2} \Omega^{-1} \langle \tilde{\phi}^2 \rangle_{,\bar{\mu}} \big) \mathrm{d}t + \bar{\boldsymbol{u}} \cdot (\mathrm{d}\bar{\boldsymbol{X}} - \bar{\boldsymbol{u}} \mathrm{d}t). \end{aligned} \tag{2.25}$$

This Lagrangian (2.25) is identical to the weak-flow gyrocentre Lagrangian up to second order (1.9) except for the last term. Our gyrocentre Lagrangian up to second order (2.25) is also substantially simpler than that of Dimits (2010a,b). In particular, our second-order terms appear only in the Hamiltonian.

The principle of least action leads to an equation for describing the behaviour of the system under consideration: the Euler-Lagrange equation. We will derive the explicit form of our Euler-Lagrange equation in the next section.

## 2.4 Euler-Lagrange equation

Using the Lagrange matrix (2.14) components computed from the gyrocentre Lagrangian (2.25) up to first-order, or equivalently those computed from the guiding-centre Lagrangian up to zeroth-order (2.17), in the gyrocentre Euler-Lagrange equation (Littlejohn, 1983),

$$\bar{\omega}_{ij} \dot{\bar{Z}}_j = \bar{\omega}_{ti},$$

where $j \in \{1, \ldots, 6\}$, with $i = \{\bar{\boldsymbol{X}}, \bar{v}_{\parallel}, \bar{\mu}, \bar{\zeta}\}$ yields

$$\dot{\bar{\boldsymbol{X}}} \times \bar{\boldsymbol{\Omega}}^* - \dot{\bar{v}}_{\parallel} \hat{\boldsymbol{b}} = \bar{\omega}_{t\bar{\boldsymbol{X}}} \tag{2.26}$$

$$\hat{\boldsymbol{b}} \cdot \dot{\bar{\boldsymbol{X}}} = \bar{v}_{\parallel}, \tag{2.27}$$

$$\dot{\bar{\zeta}} = \Omega + \langle\phi\rangle_{,\bar{\mu}} + \bar{\boldsymbol{u}} \cdot \bar{\boldsymbol{u}}_{,\mu} - \bar{\boldsymbol{u}}_{,\bar{\mu}} \cdot \dot{\bar{\boldsymbol{X}}}, \tag{2.28}$$

$$\dot{\bar{\mu}} = 0, \tag{2.29}$$

respectively. By Noether's theorem, the $\bar{\zeta}$-symmetry of our Lagrangian (2.25) corresponds to the adiabatic invariance of $\bar{\mu}$ (2.29).

Taking the cross product of $\hat{\boldsymbol{b}}$ and Equation 2.26, expanding the resultant triple product and using Equation 2.27 yields

$$\dot{\bar{\boldsymbol{X}}} = \bar{\Omega}_{\parallel}^{*-1}\{\Omega\bar{\boldsymbol{u}} + \hat{\boldsymbol{b}} \times [\bar{\boldsymbol{u}} \times (\bar{\boldsymbol{\nabla}} \times \bar{\boldsymbol{u}}) + (\bar{\boldsymbol{u}} \cdot \bar{\boldsymbol{\nabla}} + \partial_t)\bar{\boldsymbol{u}}] + \bar{v}_{\parallel}\bar{\boldsymbol{\Omega}}^*\}, \tag{2.30}$$

where

$$\bar{\Omega}_{\parallel}^* = \hat{\boldsymbol{b}} \cdot \bar{\boldsymbol{\Omega}}^*. \tag{2.31}$$

By expanding the triple product and using the vector identity

$$\bar{\boldsymbol{\Omega}}^* = \bar{\Omega}_{\parallel}^*\hat{\boldsymbol{b}} + \hat{\boldsymbol{b}} \times \bar{\boldsymbol{u}}_{,\parallel}, \tag{2.32}$$

which is analogous to that in Hahm (1988),

$$\dot{\bar{\boldsymbol{X}}} = \bar{\boldsymbol{u}} + \bar{\Omega}_{\parallel}^{*-1}\hat{\boldsymbol{b}} \times (\partial_t + \bar{\boldsymbol{u}} \cdot \bar{\boldsymbol{\nabla}} + \bar{v}_{\parallel}\bar{\nabla}_{\parallel})\bar{\boldsymbol{u}} + \bar{v}_{\parallel}\hat{\boldsymbol{b}}. \tag{2.33}$$

The second term in $\dot{\bar{\boldsymbol{X}}}$ (2.33) is the strong-flow term. It is a polarisation drift that originates from the change of frame and contains centrifugal and Coriolis drift terms, which are the second and third terms in the parentheses, respectively.

Projecting Equation 2.26 onto $\bar{\boldsymbol{\Omega}}^*$ yields

$$\dot{\bar{v}}_{\parallel} = -\bar{\Omega}_{\parallel}^{*-1}\bar{\boldsymbol{\Omega}}^* \cdot [\bar{\boldsymbol{\nabla}}\langle\phi\rangle + \bar{\boldsymbol{u}} \times (\bar{\boldsymbol{\nabla}} \times \bar{\boldsymbol{u}}) + (\bar{\boldsymbol{u}} \cdot \bar{\boldsymbol{\nabla}} + \partial_t)\bar{\boldsymbol{u}}].$$

By using Equation 2.32 with the first and last terms and Equation 2.18 with

the second term, and expanding the cross product,

$$\dot{\bar{v}}_{\parallel} = -\langle\phi\rangle_{,\parallel} + \bar{\Omega}_{\parallel}^{*-1}\bar{\boldsymbol{u}}_{,\parallel}\cdot\hat{\boldsymbol{b}}\times(\partial_t + \bar{\boldsymbol{u}}\cdot\bar{\boldsymbol{\nabla}})\bar{\boldsymbol{u}}. \tag{2.34}$$

The second term in $\dot{\bar{v}}_{\parallel}$ (2.34) is the strong-flow term. It is absent from that of Dimits (2010a,b), although a similar term is present in the second-order part of $\dot{\bar{v}}_{\parallel}$ of Dimits (2010a,b).

Inserting $\dot{\bar{\boldsymbol{X}}}$ (2.33) into $\dot{\bar{\zeta}}$ (2.28) yields

$$\dot{\bar{\zeta}} = \Omega + \langle\phi\rangle_{,\bar{\mu}} - \bar{\Omega}_{\parallel}^{*-1}\bar{\boldsymbol{u}}_{,\bar{\mu}}\cdot\hat{\boldsymbol{b}}\times(\partial_t + \bar{\boldsymbol{u}}\cdot\bar{\boldsymbol{\nabla}} + \bar{v}_{\parallel}\bar{\nabla}_{\parallel})\bar{\boldsymbol{u}}.$$

The contributions to the Euler-Lagrange equations from the second-order part of the gyrocentre Lagrangian are

$$\begin{aligned}
\dot{\bar{\boldsymbol{X}}}_2 &= \bar{\Omega}_{\parallel}^{*-1}\hat{\boldsymbol{b}}\times\bar{\boldsymbol{\nabla}}\bar{H}_2,\\
\dot{\bar{v}}_{\parallel 2} &= -\bar{H}_{2,\parallel} + \bar{\Omega}_{\parallel}^{*-1}\bar{\boldsymbol{u}}_{,\parallel}\cdot\hat{\boldsymbol{b}}\times\bar{\boldsymbol{\nabla}}\bar{H}_2,\\
\dot{\bar{\zeta}}_2 &= \bar{H}_{2,\bar{\mu}},\\
\bar{H}_2 &= \tfrac{1}{2}\langle g_1^{\boldsymbol{X}}\cdot\boldsymbol{\nabla}\tilde{\phi}\rangle + \tfrac{1}{2}\Omega^{-1}\langle\delta_1\tilde{\phi}^2\rangle_{,\mu} + \hat{\boldsymbol{b}}\times\langle\delta_1\tilde{\phi}\boldsymbol{\rho}\rangle\cdot\boldsymbol{u}_{,\mu}.
\end{aligned}$$

where $\bar{H}_2$ is the second-order part of the gyrocentre Hamiltonian (2.23). As is the case for weak flows, the Euler-Lagrange equations that include the contributions from the second-order part of the gyrocentre Lagrangian can be simplified by renormalising the potential.

Now we are in a position to use Liouville's theorem to obtain a Vlasov equation. In order to complete the description of a collisionless particle-field system, state-of-the-art gyrokinetic theory employs non-relativistic classical field theory. However, symplectic strong flows necessitate a generalisation of conventional gyrokinetic field theory. This is described in the next section.

## 2.5 Field theory

The particle-field system Lagrangian is

$$L_{\mathrm{s}} = \sum_n L_n + L_{\mathrm{f}}, \tag{2.35}$$

where $L_n$ is the $n$th particle Lagrangian and $L_{\mathrm{f}}$ is the field part of the system Lagrangian. Within tokamaks, the large E × B particle-drift kinetic energy compared to field energy or *quasineutrality* implies that

$$L_{\mathrm{f}} = 0.$$

It is useful to write our system Lagrangian (2.35) in terms of the species distribution function $f(z,t)$, where the species subscript has been suppressed. This is analogous to writing the particle number $N(t)$ in terms of the species distribution function,

$$N = \sum_n 1 = \int \mathrm{d}^6 z f,$$

where the species sum has been suppressed. Our discrete system Lagrangian (2.35) then becomes

$$L_{\mathrm{s}} = \int \mathrm{d}^6 z f L. \tag{2.36}$$

We wish to write our system Lagrangian in terms of our gyrocentre coordinate. Going from our discrete (2.35) to our smooth (2.36) form of system Lagrangian is coordinate system independent, so we may simply write down our gyrocentre system Lagrangian as

$$L_{\mathrm{s}} = \int \mathrm{d}^6 \bar{Z} \bar{F}(\bar{Z},t) L, \tag{2.37}$$

where $\bar{F}$ is the gyrocentre species distribution function.

We may equivalently obtain our gyrocentre system Lagrangian (2.37) by transforming our original system Lagrangian (2.36) from coordinate $z$ to $\bar{Z}$.

The integration element $\mathrm{d}^6 z$ transforms as

$$\mathrm{d}^6 z = J_{\bar{Z}\to z}\mathrm{d}^6 \bar{Z}, \tag{2.38}$$

where

$$J_{\bar{Z}\to z} = |\bar{\partial}_i \mathcal{T}_{\bar{Z}\to z}\bar{Z}_j|$$

is the Jacobian determinant and $\mathcal{T}_{\bar{Z}\to z}$ is a mapping from coordinate system $\bar{Z}$ to $z$. The distribution function $f$ must transform as a scalar density,

$$f = (J_{\bar{Z}\to z})^{-1}\bar{F}. \tag{2.39}$$

Performing these two transformations results in all the factors of the Jacobian cancelling and yields the same gyrocentre system Lagrangian (2.37) as before.

The invariance of the original (2.36) and gyrocentre (2.37) system Lagrangians is apparent from their manifest covariance.

Conventional gyrokinetic field theory (Sugama, 2000; Brizard and Tronko, 2011) simply transforms $f$ as a scalar, as opposed to a scalar density (2.39), and so arrives at a form of gyrocentre system Lagrangian that is not manifestly covariant.

The Poisson equation is obtained from the stationary variation of the system Lagrangian with respect to the potential. In order to comply with the demand for general covariance, the variation must be performed on forms (2.35, 2.36, 2.37) of the system Lagrangian whose manifest covariance imply invariance.

Conventional gyrokinetic field theory varies a system Lagrangian that is not manifestly covariant, so the variation is not guaranteed to be invariant.

Whilst we are able to write our Vlasov-Poisson equations in terms of our gyrocentre coordinate, we are, ultimately, interested in equations that are written in terms of the conventional gyrocentre species distribution function (Dubin

et al., 1983; Brizard and Hahm, 2007)

$$\bar{F}'(\bar{Z}) = f(\mathcal{T}_{\bar{Z}\to z}\bar{Z}), \tag{2.40}$$

where $\bar{F}'$ is $\zeta$-independent,

$$\bar{F}'_{,\zeta} = 0. \tag{2.41}$$

It is, therefore, necessary to use the expression relating our original and gyrocentre distributions functions (2.39) in our gyrocentre system Lagrangian (2.37).

The Jacobian in this expression (2.39) can be written in terms of the gyrocentre Lagrange matrix (2.14),

$$J_{\bar{Z}\to z} = |\bar{\omega}_{ij}|^{\frac{1}{2}}. \tag{2.42}$$

This Lagrange matrix is a function of the symplectic part of the gyrocentre Lagrangian (2.25), which, in turn, depends on the potential. In order to comply with the demand for general covariance, the expression (2.39) should only be used after the variation with respect to the potential has been performed.

Conventional gyrokinetic field theory uses a gyrocentre system Lagrangian that is written directly in terms the conventional gyrocentre distribution function (2.40). In the absence of symplectic strong flows, the symplectic part of the gyrocentre Lagrangian (1.9), the gyrocentre Lagrange matrix $\bar{\omega}_{ij}$ and the gyrocentre Jacobian are all independent of the potential. Thus, care is only needed for the case of a symplectic strong-flow theory.

The Vlasov equation is obtained from Liouville's theorem,

$$\dot{\bar{F}}' = 0.$$

Our gyrocentre Vlasov equation is

$$\bar{F}'_{,t} + \dot{\bar{Z}}_{\bar{i}}\bar{F}'_{,\bar{i}} = 0. \tag{2.43}$$

Conventional gyrokinetic field theory (Brizard, 2000) obtains the Vlasov equation from the system Lagrangian by prescribing the variation.

We will use the field theory described in this section to derive our Poisson equation in the next section.

Unlike Dimits (2010a,b), our Vlasov-Poisson system is manifestly conservative as, ultimately, we obtain it as a whole, directly from our gyrocentre particle Lagrangian (2.25) (Scott and Smirnov, 2010).

## 2.6 Poisson equation

We will derive our Poisson equation using both the manifestly conservative, variational method described in the previous section and the original, direct method (Dubin et al., 1983).

### 2.6.1 Variational method

The variation of our gyrocentre system Lagrangian (2.37) with respect to the potential is

$$(\delta L_{\mathrm{s}})_{\phi} = \int \mathrm{d}^6 \bar{Z} \bar{F} (\delta L)_{\phi}, \tag{2.44}$$

where $(\delta L)_{\phi}$ is the variation of the particle Lagrangian with respect to the potential.

By using a variational method, it is possible to obtain a Poisson equation from our gyrocentre Lagrangian up to zeroth order.

#### Zeroth order

Our gyrocentre Lagrangian up to zeroth-order is

$$\bar{\Gamma}_{-1,0} = \bar{\Gamma}_{-1} + \bar{\Gamma}_0 = [\boldsymbol{A}(\bar{\boldsymbol{X}}) + \bar{v}_{\parallel} \hat{\boldsymbol{b}}] \cdot \mathrm{d}\bar{\boldsymbol{X}} + \bar{\mu} \mathrm{d}\bar{\zeta} - \left( \tfrac{1}{2} \bar{v}_{\parallel}^2 + \bar{\mu} \Omega + \langle \phi \rangle \right) \mathrm{d}t + \bar{\boldsymbol{u}} \cdot \left( \mathrm{d}\bar{\boldsymbol{X}} - \tfrac{1}{2} \bar{\boldsymbol{u}} \mathrm{d}t \right). \tag{2.45}$$

The potential-dependent part of this Lagrangian (2.45) is

$$\bar{\Gamma}_{-1,0\phi} = -\langle\phi\rangle \mathrm{d}t + \bar{\boldsymbol{u}} \cdot (\mathrm{d}\bar{\boldsymbol{X}} - \tfrac{1}{2}\bar{\boldsymbol{u}}\mathrm{d}t). \tag{2.46}$$

We can use the expression relating our particle Lagrangian written as a 1- or 0-form (1.3) and express $\bar{\boldsymbol{u}}$ in terms of the potential (2.12) in order to vary the potential-dependent part (2.46) of the Lagrangian (2.45) with respect to the potential in the variation (2.44). This yields

$$\begin{aligned}(\delta L_{\mathrm{s}-1,0})_\phi &= -\int \mathrm{d}^6\bar{Z}\bar{F}\{[\langle\phi+\delta\phi\rangle - \Omega^{-1}\bar{\boldsymbol{\nabla}}\langle\phi+\delta\phi\rangle \cdot (\dot{\bar{\boldsymbol{X}}} \times \hat{\boldsymbol{b}} - \tfrac{1}{2}\Omega^{-1}\bar{\boldsymbol{\nabla}}_\perp\langle\phi \\ &\quad +\delta\phi\rangle)] - [\langle\phi\rangle - \Omega^{-1}\bar{\boldsymbol{\nabla}}\langle\phi\rangle \cdot (\dot{\bar{\boldsymbol{X}}} \times \hat{\boldsymbol{b}} - \tfrac{1}{2}\Omega^{-1}\bar{\boldsymbol{\nabla}}_\perp\langle\phi\rangle)]\} \\ &= -\int \mathrm{d}^6\bar{Z}\bar{F}[\langle\delta\phi\rangle - \Omega^{-1}\bar{\boldsymbol{\nabla}}\langle\delta\phi\rangle \cdot (\dot{\bar{\boldsymbol{X}}} \times \hat{\boldsymbol{b}} - \Omega^{-1}\bar{\boldsymbol{\nabla}}_\perp\langle\phi\rangle)],\end{aligned} \tag{2.47}$$

where $\delta\phi$ is the variation of the potential and the pertinent variation is linear (Morrison, 2005). By performing an integration by parts so as to move the gyrocentre gradient acting on $\langle\delta\phi\rangle$, the variation (2.47) can be written as

$$(\delta L_{\mathrm{s}-1,0})_\phi = -\int \mathrm{d}^6\bar{Z}\langle\delta\phi\rangle[\bar{F} + \Omega^{-1}\hat{\boldsymbol{b}} \cdot \bar{\boldsymbol{\nabla}} \times \bar{F}(\dot{\bar{\boldsymbol{X}}} - \bar{\boldsymbol{u}})], \tag{2.48}$$

where the surface term was evaluated to give zero. Expanding the integration element as

$$\mathrm{d}^6\bar{Z} = \mathrm{d}\bar{\boldsymbol{X}}\mathrm{d}\bar{v}_\parallel\mathrm{d}\bar{\mu}\mathrm{d}\bar{\zeta}, \tag{2.49}$$

integrating over $\bar{\zeta}$ and expanding the gyroaverage (1.10) in the variation (2.48) yields

$$(\delta L_{\mathrm{s}-1,0})_\phi = -\int \mathrm{d}^3x\delta\phi \int \mathrm{d}^6\bar{Z}\delta(\bar{\boldsymbol{X}} + \bar{\boldsymbol{\rho}} - \boldsymbol{x})[\bar{F} + \Omega^{-1}\hat{\boldsymbol{b}} \cdot \bar{\boldsymbol{\nabla}} \times \bar{F}(\dot{\bar{\boldsymbol{X}}} - \bar{\boldsymbol{u}})]. \tag{2.50}$$

Upon requiring stationary variation,

$$(\delta L_{\mathrm{s}-1,0})_\phi = 0,$$

we can obtain the Poisson equation from our gyrocentre Lagrangian up to zeroth order as

$$0 = \int \mathrm{d}^6 \bar{Z} \delta(\bar{\boldsymbol{X}} + \bar{\boldsymbol{\rho}} - \boldsymbol{x})[\bar{F} + \Omega^{-1} \hat{\boldsymbol{b}} \cdot \bar{\boldsymbol{\nabla}} \times \bar{F}(\dot{\bar{\boldsymbol{X}}} - \bar{\boldsymbol{u}})]. \tag{2.51}$$

For uniform $\bar{F}'$, this Poisson equation (2.51) up to first order is

$$0 = \int \mathrm{d}^6 \bar{Z} \delta(\bar{\boldsymbol{X}} + \bar{\boldsymbol{\rho}} - \boldsymbol{x})(1 + \Omega^{-1} \hat{\boldsymbol{b}} \cdot \bar{\boldsymbol{\nabla}} \times \bar{\boldsymbol{u}}) \bar{F}'. \tag{2.52}$$

In the weak-flow limit, this Poisson equation (2.52) is identical to the weak-flow Poisson equation in the $k_\perp \rho_\mathrm{t} \sim \epsilon$ limit up to first order with uniform $\bar{F}'$.

We will now obtain the Poisson equation from our gyrocentre Lagrangian up to second order (2.25).

### Second order

The potential-dependent part of our gyrocentre Lagrangian up to second order (2.25) is

$$\bar{\Gamma}_\phi = -(\langle \phi \rangle - \tfrac{1}{2} \langle g_1^{\bar{\boldsymbol{X}}} \cdot \bar{\boldsymbol{\nabla}} \tilde{\phi} \rangle - \tfrac{1}{2} \Omega^{-1} \langle \tilde{\phi}^2 \rangle_{,\bar{\mu}}) \mathrm{d}t + \bar{\boldsymbol{u}} \cdot (\mathrm{d}\bar{\boldsymbol{X}} - \bar{\boldsymbol{u}} \mathrm{d}t). \tag{2.53}$$

We can use the expression relating our particle Lagrangian written as a 1- or 0-form (1.3) and express $g_1^{\bar{\boldsymbol{X}}}$ (2.20) and $\bar{\boldsymbol{u}}$ (2.12) in terms of the potential in order to vary the potential-dependent part (2.53) of this Lagrangian (2.25) with respect to the potential in the variation (2.44). This yields

$$\begin{aligned}
(\delta L_\mathrm{s})_\phi = \; & -\int \mathrm{d}^6 \bar{Z} \bar{F} \{ [\langle \phi + \delta\phi \rangle - \tfrac{1}{2} \Omega^{-2} \langle \bar{\boldsymbol{\nabla}} (\tilde{\Phi} + \delta\tilde{\Phi}) \times \hat{\boldsymbol{b}} \cdot \bar{\boldsymbol{\nabla}} (\tilde{\phi} + \delta\tilde{\phi}) \rangle \\
& - \tfrac{1}{2} \Omega^{-1} \langle (\tilde{\phi} + \delta\tilde{\phi})^2 \rangle_{,\bar{\mu}} - \Omega^{-1} \bar{\boldsymbol{\nabla}} \langle \phi + \delta\phi \rangle \cdot (\dot{\bar{\boldsymbol{X}}} \times \hat{\boldsymbol{b}} \\
& - \Omega^{-1} \bar{\boldsymbol{\nabla}}_\perp \langle \phi + \delta\phi \rangle)] - [\langle \phi \rangle - \tfrac{1}{2} \Omega^{-2} \langle \bar{\boldsymbol{\nabla}} \tilde{\Phi} \times \hat{\boldsymbol{b}} \cdot \bar{\boldsymbol{\nabla}} \tilde{\phi} \rangle - \tfrac{1}{2} \Omega^{-1} \langle \tilde{\phi}^2 \rangle_{,\bar{\mu}} \\
& - \Omega^{-1} \bar{\boldsymbol{\nabla}} \langle \phi \rangle \cdot (\dot{\bar{\boldsymbol{X}}} \times \hat{\boldsymbol{b}} - \Omega^{-1} \bar{\boldsymbol{\nabla}}_\perp \langle \phi \rangle)] \} \\
= \; & -\int \mathrm{d}^6 \bar{Z} \bar{F} [\langle \delta\phi \rangle - \Omega^{-2} \langle \bar{\boldsymbol{\nabla}} \tilde{\Phi} \times \hat{\boldsymbol{b}} \cdot \bar{\boldsymbol{\nabla}} \delta\phi \rangle - \Omega^{-1} \langle \tilde{\phi} \delta\phi \rangle_{,\bar{\mu}} \\
& - \Omega^{-1} \bar{\boldsymbol{\nabla}} \langle \delta\phi \rangle \cdot (\dot{\bar{\boldsymbol{X}}} \times \hat{\boldsymbol{b}} - 2\Omega^{-1} \bar{\boldsymbol{\nabla}}_\perp \langle \phi \rangle)].
\end{aligned} \tag{2.54}$$

By performing integrations by parts so as to move the derivatives acting on $\delta\phi$, the variation (2.54) can be written as

$$(\delta L_{\rm s})_\phi = -\int \mathrm{d}^6\bar{Z}\langle\delta\phi[(1+\Omega^{-2}\bar{\boldsymbol{\nabla}}\tilde{\Phi}\times\hat{\boldsymbol{b}}\cdot\bar{\boldsymbol{\nabla}}+\Omega^{-1}\tilde{\phi}\partial_{\bar{\mu}})\bar{F} + \Omega^{-1}\hat{\boldsymbol{b}}\cdot\bar{\boldsymbol{\nabla}}\times\bar{F}(\dot{\bar{\boldsymbol{X}}}-2\bar{\boldsymbol{u}})]\rangle, \tag{2.55}$$

where the surface terms have been evaluated to give zero. Expanding the integration element (2.49), integrating over $\bar{\zeta}$ and expanding the gyroaverage (1.10) in the variation (2.55) yields

$$(\delta L_{\rm s})_\phi = -\int \mathrm{d}^3x\delta\phi\int \mathrm{d}^6\bar{Z}\delta(\bar{\boldsymbol{X}}+\bar{\boldsymbol{\rho}}-\boldsymbol{x})[(1+\Omega^{-2}\bar{\boldsymbol{\nabla}}\tilde{\Phi}\times\hat{\boldsymbol{b}}\cdot\bar{\boldsymbol{\nabla}}+\Omega^{-1}\tilde{\phi}\partial_{\bar{\mu}})\bar{F} + \Omega^{-1}\hat{\boldsymbol{b}}\cdot\bar{\boldsymbol{\nabla}}\times\bar{F}(\dot{\bar{\boldsymbol{X}}}-2\bar{\boldsymbol{u}})]. \tag{2.56}$$

Upon requiring stationary variation, we can obtain our Poisson equation as

$$0 = \int \mathrm{d}^6\bar{Z}\delta(\bar{\boldsymbol{X}}+\bar{\boldsymbol{\rho}}-\boldsymbol{x})[(1+\Omega^{-2}\bar{\boldsymbol{\nabla}}\tilde{\Phi}\times\hat{\boldsymbol{b}}\cdot\bar{\boldsymbol{\nabla}}+\Omega^{-1}\tilde{\phi}\partial_{\bar{\mu}})\bar{F} + \Omega^{-1}\hat{\boldsymbol{b}}\cdot\bar{\boldsymbol{\nabla}}\times\bar{F}(\dot{\bar{\boldsymbol{X}}}-2\bar{\boldsymbol{u}})]. \tag{2.57}$$

We present an alternative, direct method to derive our Poisson equation in the next subsection.

### 2.6.2 Direct method

Here, the Poisson equation is

$$0 = \rho_{\rm c}, \tag{2.58}$$

where $\rho_{\rm c}$ is the charge density. The charge density can be written in terms of the distribution function such that this Poisson equation (2.58) becomes

$$0 = \int \mathrm{d}^3v f. \tag{2.59}$$

This Poisson equation (2.59) can be written in terms of an integral over $z$ as

$$0 = \int \mathrm{d}^6 z \delta(\boldsymbol{x} - \boldsymbol{r}) f, \tag{2.60}$$

where $\boldsymbol{r}$ is the position.

This Poisson equation (2.60) can be equivalently evaluated in terms of either our guiding-centre or gyrocentre coordinate.

### Guiding-centre coordinate

We can perform a change of variables from our original coordinate $z$ to our guiding-centre coordinate $Z$.

The integration element transforms as

$$\mathrm{d}^6 z = J_{Z \to z} \mathrm{d}^6 Z.$$

We can use this, the relation between our original and guiding-centre position (1.6) and the conventional guiding-centre species distribution function

$$F'(Z) = f(\mathcal{T}_{Z \to z} Z)$$

in the Poisson equation (2.60) to yield

$$0 = \int J_{Z \to z} \mathrm{d}^6 Z \delta(\boldsymbol{X} + \boldsymbol{\rho} - \boldsymbol{r}) F'.$$

Once again, we are interested in equations that are written in terms of the conventional gyrocentre distribution function. In order to achieve this, we may use the action of the Lie transform (2.13) on scalars,

$$\mathcal{L}_n f = g_n^a \partial_a f, \tag{2.61}$$

to relate the conventional guiding-centre and gyrocentre distribution functions

as

$$F' = \mathsf{T}\bar{F}'(Z).$$

The Poisson equation is then

$$0 = \int J_{Z\to z} \mathrm{d}^6 Z \delta(\boldsymbol{X} + \boldsymbol{\rho} - \boldsymbol{r}) \mathsf{T}\bar{F}'. \tag{2.62}$$

The guiding-centre Jacobian determinant is

$$J_{Z\to z} = |\bar{\partial}_i \mathcal{T}_{Z\to z} Z_j| = \Omega_\parallel^* + \boldsymbol{\rho}\cdot\boldsymbol{\Omega}\times\boldsymbol{u}_{,\mu} + \Omega^{-1}\epsilon_{i'j'}u_{i',1}u_{j',2} + \rho_{i'}u_{j',\mu}u_{i',j'}, \tag{2.63}$$

where the guiding-centre Jacobian matrix is

$$\partial_{i'}\mathcal{T}_{Z\to z} Z_{j'} = \begin{pmatrix} 1 & 0 & 0 & 0 & -v_2 v_\perp^{-2} & \rho_2 \\ 0 & 1 & 0 & 0 & v_1 v_\perp^{-2} & -\rho_1 \\ 0 & 0 & 1 & 0 & 0 & 0 \\ u_{1,1} & u_{1,2} & u_{1,z} & 0 & u_{1,\mu} + \rho_2\rho^{-2} & v_2 \\ u_{2,1} & u_{2,2} & u_{2,z} & 0 & u_{2,\mu} - \rho_1\rho^{-2} & -v_1 \\ 0 & 0 & 0 & 1 & 0 & 0 \end{pmatrix}$$

and $\epsilon_{i'j'}$ is the two-dimensional Levi-Civita pseudotensor. We obtain the same result by evaluating this Jacobian written in terms of the Lagrange matrix (2.42), where the non-zero Lagrange matrix components are

$$\begin{aligned} \omega_{X_i' X_j'} &= \epsilon_{i'j'k'}\Omega_{k'}^*, \\ \omega_{\boldsymbol{X} v_\parallel} &= -\hat{\boldsymbol{b}}, \\ \omega_{\boldsymbol{X}\mu} &= v_\perp^{-1}\hat{\boldsymbol{\rho}}\cdot\boldsymbol{\nabla}\boldsymbol{u} - \boldsymbol{u}_{,\mu} \\ \omega_{\boldsymbol{X}\zeta} &= \rho\hat{\boldsymbol{v}}_\perp\cdot\boldsymbol{\nabla}\boldsymbol{u} \\ \omega_{\mu\zeta} &= 1 + \rho\hat{\boldsymbol{v}}_\perp\cdot\boldsymbol{u}_{,\mu}. \end{aligned}$$

By using the guiding-centre Jacobian (2.63) up to first order

$$J_{Z\to z0,1} = \Omega_{\parallel}^{*} + \boldsymbol{\rho}\cdot\boldsymbol{\Omega}\times\boldsymbol{u}_{,\mu}$$

and the action of the Lie transform on scalars (2.13, 2.61) up to first order

$$(\mathsf{T}^{\pm 1}\bar{F}')_{0,1} = (1 \pm g_1^i\partial_i)\bar{F}', \tag{2.64}$$

an evaluation of the direct Poisson equation (2.62) up to first order yields the same expression as the variational Poisson equation up to first order (2.67), up to a dummy variable (Dubin et al., 1983).

We may equivalently evaluate the direct Poisson equation (2.60) in terms of our gyrocentre coordinate.

### Gyrocentre coordinate

We transform directly from our original to gyrocentre coordinate.

We may transform the integration element, particle position and original distribution function as before (2.38, 1.6, 2.40). This yields

$$0 = \int J_{\bar{Z}\to z}\mathrm{d}^6\bar{Z}\,\delta(\boldsymbol{X}+\boldsymbol{\rho}-\boldsymbol{r})\bar{F}'.$$

The particle position (1.6) may then be transformed (Brizard and Hahm, 2007) as

$$\boldsymbol{X}+\boldsymbol{\rho} = \mathcal{T}_{\bar{Z}\to Z}(\bar{\boldsymbol{X}}+\bar{\boldsymbol{\rho}}),$$

yielding

$$0 = \int J_{\bar{Z}\to z}\mathrm{d}^6\bar{Z}\,\delta[\mathcal{T}_{\bar{Z}\to Z}(\bar{\boldsymbol{X}}+\bar{\boldsymbol{\rho}})-\boldsymbol{r}]\bar{F}'.$$

We may write this delta function in terms of the Lie transform (2.13) (Brizard and Hahm, 2007) as

$$\delta[\mathcal{T}_{\bar{Z}\to Z}(\bar{\boldsymbol{X}}+\bar{\boldsymbol{\rho}})-\boldsymbol{r}] = \mathsf{T}^{-1}\delta(\bar{\boldsymbol{X}}+\bar{\boldsymbol{\rho}}-\boldsymbol{r}).$$

This yields

$$0 = \int J_{\bar{Z}\to z} \mathrm{d}^6 \bar{Z} [\mathsf{T}^{-1} \delta(\bar{\boldsymbol{X}} + \bar{\boldsymbol{\rho}} - \boldsymbol{r})] \bar{F}'. \tag{2.65}$$

By using the action of the Lie transform on scalars up to first order (2.64) and performing an integration by parts so as to move the derivative within this Lie transform, an evaluation of this gyrocentre direct Poisson equation (2.65) up to first order again yields the same expression as the variational Poisson equation up to first order (2.67), given that the surface terms can be evaluated to give zero and

$$\bar{\partial}_i \bar{g}_1^i = \Omega^{-1} \bar{\boldsymbol{v}}_\perp \cdot \bar{\boldsymbol{u}}_{,\bar{\mu}}.$$

Weak-flow gyrokinetics is a very well established theoretical tool (Krommes, 2012). Symplectic strong-flow gyrokinetic theories have been criticised (Miyato et al., 2009; Scott and Smirnov, 2010; Scott, 2013) for a lack of weak-flow consistency. We consider the weak-flow limit of our Poisson equation (2.57) in the next subsection.

### 2.6.3 Weak-flow limit

In order to take the weak-flow limit consistently, we will consider uniform $\bar{F}'$. We can evaluate our gyrocentre Jacobian written in terms of the gyrocentre Lagrange matrix (2.42) as

$$J_{\bar{Z}\to z} = \bar{\Omega}^*_{\|}, \tag{2.66}$$

where the non-zero gyrocentre Lagrange matrix components are

$$\begin{aligned}
\omega_{\bar{X}_{i'}\bar{X}_{j'}} &= \epsilon_{i'j'k'} \bar{\Omega}^*_{k'}, \\
\omega_{\bar{\boldsymbol{X}}\bar{v}_\|} &= -\hat{\boldsymbol{b}}, \\
\omega_{\bar{\boldsymbol{X}}\bar{\mu}} &= -\bar{\boldsymbol{u}}_{,\bar{\mu}}, \\
\omega_{\bar{\mu}\bar{\zeta}} &= 1.
\end{aligned}$$

This Jacobian (2.66) is not equal to the guiding-centre Jacobian (2.63). This

arises from the symplectic dependence of the Jacobians (2.42) and the symplectic parts of the guiding-centre (2.7) and gyrocentre (2.25) Lagrangians differing by a gyroangle-dependent term. For weak flows, the two Jacobians are identical as the symplectic parts of the two Lagrangians are identical.

By using an alternative form for the second-order part of our gyrocentre Lagrangian (2.24) and our gyrocentre Jacobian (2.66), our Poisson equation up to first order is

$$\begin{aligned} 0 =& \Omega \int \mathrm{d}^6 \bar{Z} \delta(\bar{\boldsymbol{X}} + \bar{\boldsymbol{\rho}} - \boldsymbol{x})[(1 + \Omega^{-1} \tilde{\phi} \partial_{\bar{\mu}}) \bar{F}' + \Omega^{-2} \bar{\nabla}_\perp^2 \langle \phi \rangle \bar{F}' \\ & - \Omega^{-1} \bar{\boldsymbol{\rho}} \cdot (\bar{F}' \bar{\boldsymbol{\nabla}} \langle \phi \rangle)_{,\bar{\mu}}]. \end{aligned} \tag{2.67}$$

By using a Fourier-space representation of the gyrocentre gradient of the gyroaveraged potential,

$$\bar{\boldsymbol{\nabla}} \langle \phi \rangle = \int \mathrm{d}^3 k (\bar{\boldsymbol{\nabla}} \langle \phi \rangle)_{\boldsymbol{k}} e^{i \boldsymbol{k} \cdot \bar{\boldsymbol{X}}},$$

the last two terms in this Poisson equation (2.67) are

$$2\pi i \int \mathrm{d}\bar{v}_\parallel \mathrm{d}\bar{\mu} \mathrm{d}^3 k \{ k_\perp \Omega^{-1} J_0(k_\perp \bar{\rho}) - [\bar{\rho} J_1(k_\perp \bar{\rho})]_{,\bar{\mu}} \} (\bar{\boldsymbol{\nabla}} \langle \phi \rangle)_{\boldsymbol{k}} e^{i \boldsymbol{k} \cdot \boldsymbol{x}} \bar{F}' = 0.$$

Our Poisson equation (2.67) then becomes

$$0 = \Omega \int \mathrm{d}^6 \bar{Z} \delta(\bar{\boldsymbol{X}} + \bar{\boldsymbol{\rho}} - \boldsymbol{x})(1 + \Omega^{-1} \tilde{\phi} \partial_{\bar{\mu}}) \bar{F}'. \tag{2.68}$$

In the weak-flow limit, this Poisson equation (2.68) is identical to the weak-flow Poisson equation up to first order with uniform $\bar{F}'$.

We now have explicit forms for our Vlasov-Poisson equations.

The fluid limit is pertinent to turbulence analysis (Brizard and Hahm, 2007; Miyato et al., 2009). We may now obtain a fluid equation for our system in the next section.

## 2.7 Fluid equation

We will obtain our fluid equation both by taking moments of our Vlasov equation and by deriving a strong-flow reduced fluid equation.

### 2.7.1 Moment equation

Our Vlasov equation (2.43) is

$$\bar{F}'_{,t} + \dot{\bar{X}}_{\bar{i}}\bar{F}'_{,\bar{i}} + \dot{\bar{v}}_{\parallel}\bar{F}'_{,\bar{v}_{\parallel}} = 0, \tag{2.69}$$

where we have used the invariance of the magnetic moment (2.29) and the gyroangle-independence of the distribution function (2.41). We can take a gyrocentre-velocity moment of this Vlasov equation as in Brizard (1990), or equivalently Miyato et al. (2009), to yield

$$n_{\mathrm{gy},t} + \dot{\bar{X}}_{\perp\bar{i}}n_{\mathrm{gy},\bar{i}} = 0, \tag{2.70}$$

where

$$n_{\mathrm{gy}} = \Omega \int \mathrm{d}^6\bar{Z}\delta(\bar{\boldsymbol{X}} + \bar{\boldsymbol{\rho}} - \boldsymbol{x})\bar{F}' \tag{2.71}$$

is our gyrocentre density, we consider a dominance of perpendicular turbulence (Hasegawa and Mima, 1977) and we have used

$$n_{\mathrm{gy},\bar{v}_{\parallel}} = 0.$$

We will now consider a two-species system by redefining $n_{\mathrm{gy}}$ as our ion gyrocentre density and writing our quasineutrality equation as

$$n_{\mathrm{gy}} = n_{\mathrm{e}} - n_{\mathrm{p}}, \tag{2.72}$$

where $n_\mathrm{e}$ is the electron density,

$$n_\mathrm{p} = n_0 \hat{\boldsymbol{b}} \cdot \bar{\boldsymbol{\nabla}} \times \dot{\bar{\boldsymbol{X}}}_\mathrm{l}$$

is the linearised (Scott and Smirnov, 2010) polarisation density in the $k_\perp \rho_\mathrm{t} \sim \epsilon$ limit up to second order,

$$n_0 = \int \mathrm{d}^6 \bar{Z} \delta(\bar{\boldsymbol{X}} + \bar{\boldsymbol{\rho}} - \boldsymbol{x}) \bar{F}_0',$$

$\bar{F}_0'$ is uniform and static, $\dot{\bar{\boldsymbol{X}}}_\mathrm{l}$ is $\dot{\bar{\boldsymbol{X}}}$ (2.33) in the $k_\perp \rho_\mathrm{t} \sim \epsilon$ limit and we use units, here and in the remainder of the thesis, such that

$$\Omega = 1,$$

so as to admit comparison to the derivation of the Hasegawa-Mima equation (Horton and Hasegawa, 1994) and aid numerical analysis. Furthermore, we will take our electron density to be uniform and static,

$$n_\mathrm{e} = n_0. \tag{2.73}$$

We may then write our moment equation (2.70) as

$$\tfrac{\mathrm{d}}{\mathrm{d}t} \hat{\boldsymbol{b}} \cdot \bar{\boldsymbol{\nabla}} \times \dot{\bar{\boldsymbol{X}}}_\mathrm{l} = 0, \tag{2.74}$$

where

$$\tfrac{\mathrm{d}}{\mathrm{d}t} = \partial_t + \dot{\bar{\boldsymbol{X}}}_\mathrm{l} \cdot \bar{\boldsymbol{\nabla}}, \tag{2.75}$$

$$\dot{\bar{\boldsymbol{X}}}_\mathrm{l} = \bar{\boldsymbol{u}}_\mathrm{l} + \hat{\boldsymbol{b}} \times (\partial_t + \bar{\boldsymbol{u}}_\mathrm{l} \cdot \bar{\boldsymbol{\nabla}}) \bar{\boldsymbol{u}}_\mathrm{l} \tag{2.76}$$

and

$$\bar{\boldsymbol{u}}_\mathrm{l} = \hat{\boldsymbol{b}} \times \bar{\boldsymbol{\nabla}} \bar{\phi}.$$

Symplectic strong-flow theories have been criticised (Scott and Smirnov, 2010;

Scott, 2013) for a lack of consistency with reduced fluid equations. In the weak-flow limit, this moment equation is identical to the Hasegawa-Mima equation, which we describe in the next subsection, with $n_\mathrm{e} = n_0$.

Our moment equation (2.74) is a gyrofluid equation (Brizard and Hahm, 2007; Miyato et al., 2009), which includes FLR physics, and, like the Hasegawa-Mima equation, it is a vorticity equation.

We obtain our fluid equation by deriving a strong-flow reduced fluid equation in the next subsection.

### 2.7.2 Reduced fluid equation

The derivation of the Hasegawa-Mima equation (Horton and Hasegawa, 1994) uses an ordering similar to our strong-flow ordering (2.2) and makes use of the Lorentz Force, ion continuity and quasineutrality equations. The procedure is to construct an equation for the parallel vorticity $\Omega_\parallel$ by taking the curl of the Lorentz Force equation and to then combine this with the ion continuity and quasineutrality equations. The equation obtained, the Hasegawa-Mima equation, is

$$\tfrac{\mathrm{d}}{\mathrm{d}t}(\Omega_\parallel - \ln n_\mathrm{e}) = 0, \tag{2.77}$$

where $\frac{\mathrm{d}}{\mathrm{d}t} = \partial_t + \bar{\boldsymbol{u}}_\mathrm{l} \cdot \bar{\boldsymbol{\nabla}}$ is the weak-flow limit of the $\frac{\mathrm{d}}{\mathrm{d}t}$ (2.75) given in the previous subsection, that is to say, with $\dot{\bar{\boldsymbol{X}}}_\mathrm{l}$ (2.76) containing the E × B but not the polarisation drift, $\Omega_\parallel = \hat{\boldsymbol{b}} \cdot \bar{\boldsymbol{\nabla}} \times \bar{\boldsymbol{u}}_\mathrm{l}$ is the weak-flow limit of the parallel vorticity given in the previous subsection, that is to say, again, with $\dot{\bar{\boldsymbol{X}}}_\mathrm{l}$ (2.76) containing the E × B but not the polarisation drift, $n_\mathrm{e} = n_0 e^{\phi}$ is an adiabatic electron density, we use units, here and in the remainder of the thesis, such that

$$T_\mathrm{e} = 1$$

and $T_\mathrm{e}$ is the electron temperature.

We can take the strong-flow limit of this equation (2.77) by including the polarisation drift in $\frac{\mathrm{d}}{\mathrm{d}t}$ and $\Omega_\parallel$. Additionally, we take the electron density to be

uniform and static, as in the previous subsection, which corresponds to taking the large-electron-temperature limit of the adiabatic response. By doing so, we obtain a strong-flow reduced fluid equation that is identical to our moment equation (2.74).

We present a numerical solution of the arbitrary-wavelength, dynamic-strong-flow gyrokinetic theory presented in this chapter in the following chapter.

# Chapter 3

# Discretisation

Symplectic strong-flow theories have been criticised (Miyato et al., 2009; Scott and Smirnov, 2010; Madsen, 2011; Scott, 2013) for equation sets that depend implicitly on the potential and its time derivative (Wang and Hahm, 2010). In this chapter, we demonstrate the tractable nature of our Vlasov-Poisson equations (2.33, 2.34, 2.57, 2.69),

$$
\begin{aligned}
&\bar{F}'_{,t} + \dot{\bar{X}}_{\bar{i}}\bar{F}'_{,\bar{i}} + \dot{\bar{v}}_{\parallel}\bar{F}'_{,\bar{v}_{\parallel}} = 0,\\
&\dot{\bar{\boldsymbol{X}}} = \bar{\boldsymbol{u}} + \bar{\Omega}_{\parallel}^{*-1}\hat{\boldsymbol{b}} \times (\partial_t + \bar{\boldsymbol{u}}\cdot\bar{\boldsymbol{\nabla}} + \bar{v}_{\parallel}\bar{\nabla}_{\parallel})\bar{\boldsymbol{u}} + \bar{v}_{\parallel}\hat{\boldsymbol{b}},\\
&\dot{\bar{v}}_{\parallel} = -\langle\phi\rangle_{,\parallel} + \bar{\Omega}_{\parallel}^{*-1}\bar{\boldsymbol{u}}_{,\parallel}\cdot\hat{\boldsymbol{b}} \times (\partial_t + \bar{\boldsymbol{u}}\cdot\bar{\boldsymbol{\nabla}})\bar{\boldsymbol{u}},\\
&0 = \int \mathrm{d}^6\bar{Z}\delta(\bar{\boldsymbol{X}} + \bar{\boldsymbol{\rho}} - \boldsymbol{x})[(1 + \Omega^{-2}\bar{\boldsymbol{\nabla}}\tilde{\Phi}\times\hat{\boldsymbol{b}}\cdot\bar{\boldsymbol{\nabla}} + \Omega^{-1}\tilde{\phi}\partial_{\bar{\mu}})\bar{F}\\
&\qquad + \Omega^{-1}\hat{\boldsymbol{b}}\cdot\bar{\boldsymbol{\nabla}}\times\bar{F}(\dot{\bar{\boldsymbol{X}}} - 2\bar{\boldsymbol{u}})].
\end{aligned}
$$

We describe our numerical scheme in the next section.

## 3.1 Scheme

From the pertinent numerical scheme options (Garbet et al., 2010), we choose the particle-in-cell method. Here, Monte-Carlo markers are used to represent distribution function quanta that are evolved along trajectories according to

consistent fields. This is shown in Figure 3.1. We use a combination of spectral

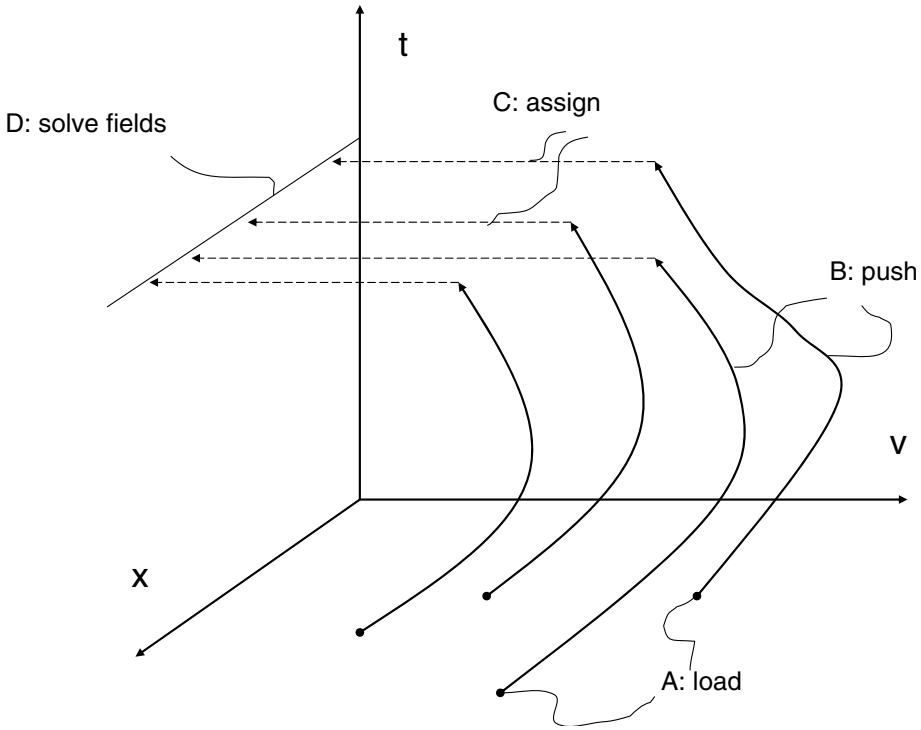


Figure 3.1: In the particle-in-cell method, markers are loaded in phase space (A), evolved or *pushed* along trajectories (B) and their charges are interpolated or *assigned* onto real space (C). Alongside this, fields that are consistent with the charge assignment (C) are solved for in real space (D) (Garbet et al., 2010).

(Frigo and Johnson, 2005) and central finite-difference methods for the fields.

In order to control the Monte-Carlo noise, a $\delta f$ method is usually employed (Garbet et al., 2010). Here, we write

$$\bar{F}' = \bar{F}'_0 + \delta\bar{F}', \tag{3.1}$$

where we choose the analytic part $\bar{F}'_0$ to be Maxwellian,

$$\bar{F}'_0 = (2\pi T)^{-\frac{3}{2}} e^{-\frac{1}{2}\bar{v}^2 T^{-1}},$$

we use units, here and in the remainder of the thesis, such that $n_0 = 1$, $T$ is the ion temperature and the discrete part

$$\delta\bar{F}' \sim \epsilon.$$

We describe this discretisation in the next section.

## 3.2 Distribution function

We can define for marker $n$ a *weight*

$$w_n(t) = \delta\bar{F}'_n V_{\mathrm{p}n}, \tag{3.2}$$

where $\delta\bar{F}'_n$ is the average value of $\delta\bar{F}'$ within our chosen marker phase-space volume

$$V_{\mathrm{p}n} = \mathrm{d}^5 z \mathrm{d}N^{-1}$$

and $\mathrm{d}N$ is the number of markers in the redefined

$$\mathrm{d}^5 z = \bar{\Omega}^*_{\parallel} \mathrm{d}^2\bar{X} \mathrm{d}\bar{v}_{\parallel} \mathrm{d}\bar{\mu} \mathrm{d}\bar{\zeta}.$$

We distribute our markers uniformly (Jolliet, 2009) in the redefined

$$\bar{Z} = (\bar{X}_1, \bar{X}_2, \bar{v}_{\parallel}, \bar{v}_{\perp}), \tag{3.3}$$

where $\bar{X}_1$ and $\bar{X}_2$ are both in the perpendicular plane. This corresponds to (Jolliet, 2009)

$$\mathrm{d}N = N(L_x L_y \pi^2 \bar{v}^2_{\mathrm{max}} T)^{-1} \mathrm{d}^2\bar{X} \mathrm{d}\bar{v}_{\parallel} \mathrm{d}\bar{v}_{\perp} \mathrm{d}\bar{\zeta}$$

and, therefore,

$$V_{\mathrm{p}n} = \bar{\Omega}^*_{\parallel n} \bar{v}_{\perp n} L_x L_y \pi^2 \bar{v}^2_{\mathrm{max}} T N^{-1}, \tag{3.4}$$

where $N$ is the number of markers, $L_x$ and $L_y$ are the lengths of the periodic two-

dimensional spatial simulation domain in the $x$ and $y$ directions, respectively, and we choose the input parameter $\bar{v}_{\max}$ to be given by

$$\bar{v}_{\max} = 5\bar{v}_{\mathrm{t}}.$$

The marker weight (3.2) is initialised by assuming

$$\bar{\Omega}^*_{\|} = \Omega$$

in the marker phase-space volume (3.4).

Markers are initialised in $\bar{Z}$ (3.3) using quasirandom, Hammersley sequences (Rafajłowicz and Schwabe, 2006). The marker phase space coordinate $\bar{Z}_n$ is initialised via

$$\begin{aligned} \bar{Z}_n &= [\bar{X}_{1n}, \bar{X}_{2n}, \arctan(\bar{v}_{\perp n}\bar{v}^{-1}_{\|n}), \bar{v}_n] \\ &= [h^1_n L_x, h^2_n L_y, h^3_n \pi, (nN^{-1}T)^{\frac{1}{2}}\bar{v}_{\max}], \end{aligned} \tag{3.5}$$

where $\arctan(\bar{v}_{\perp}\bar{v}^{-1}_{\|})$ is the pitch angle,

$$h^m_n = \sum_{o\geq 0} c_{mo}(n) p_m^{-(o+1)} \in (0,1)$$

are the Hammersley sequences, $n \in \{1, \ldots, N\}$, $N$ is the number of markers, $c_{mo}(n)$ is the $o$th coefficient in the unique expansion of $n$ in base $p_m$,

$$n = \sum_{o\geq 0} c_{mo}(n) p^o_m, \tag{3.6}$$

and is uniquely defined in terms of this unique expansion (3.6), and $p_m$ is a prime number. From this (3.5), we compute $\bar{Z}_n$ as before (3.3).

We choose the spatial dependence of $\delta f$ in order to specify the desired potential initialisation.

The code has been Message-Passing-Interface parallelised by distributing

markers amongst processors. The field discretisation is unparallelised. The code exhibits excellent strong scaling up to at least 512 processors.

We describe our field discretisation in the next section.

## 3.3 Poisson equation

Our Poisson equation (2.57) depends implicitly on the time derivative of the potential. This is not the case for the weak-flow Poisson equation (Hahm, 1988). Thus, the method of solution of our Poisson equation deviates from that for weak flows.

### 3.3.1 Quasistatic solution

For simplicity of illustration, we may write our Poisson equation (2.57) symbolically as

$$\phi = W + I\phi_{,t}, \tag{3.7}$$

where $W$ represents the part of our Poisson equation (2.57) that is analogous to the weak-flow Poisson equation (Hahm, 1988) and is related to the gyrodensity (2.71) and the reciprocal of spatial polarisation operators and $I$ represents the part of our Poisson equation (2.57) that is related to the implicit dependence on the time derivative of the potential and the reciprocal of spatial polarisation operators. For short timescales, we may write the general solution of this equation (3.7) as

$$\phi = \phi_W + \phi_I e^{tI^{-1}}, \tag{3.8}$$

where $\phi_W$ is the inhomogeneous solution and $\phi_I \sim 1$ is a constant. According to our strong-flow ordering (2.2),

$$I \sim \epsilon.$$

This implies that potential initialisations (3.8) are allowed that violate the fundamental low frequency ordering contained within our strong-flow ordering (2.2).

In general, we have that

$$I \in \mathbb{C}$$

and that, as the strong-flow formalism is an extension of the weak-flow one,

$$\mathrm{Re}(I) \leq 0.$$

We can, therefore, choose to solve our Vlasov-Poisson system in the quasistatic limit by iterating the solution of our Poisson equation (3.7), where the first iteration uses

$$\phi = W.$$

For a spatially uniform $\bar{F}_0'$, our linearised Poisson equation does not contain a term involving the time derivative of the potential and an alternative solution method from that for weak flows is unnecessary.

### 3.3.2 Uniform background

We will use interpolation to pass information between our markers to our grid. Using the simplest possible, nearest-neighbour interpolation, a one-dimensional grid quantity is given by

$$G_n = \sum_{m=1}^{N} M_m i_0(\bar{\boldsymbol{x}}_m \cdot \hat{e}_1 - x_n),$$

where $n \in \{1, \ldots, N_x\}$, $N_x$ is the number of grid points in the $x$ direction, $M$ is the value of a quantity at a marker,

$$i_0(x) = \begin{cases} 0, & x < -\frac{1}{2}\Delta x \\ 1, & -\frac{1}{2}\Delta x \leq x < \frac{1}{2}\Delta x \\ 0, & x \geq \frac{1}{2}\Delta x \end{cases}$$

is the interpolant, $\Delta x = L_x N_x^{-1}$ is the grid spacing in the $x$ direction and $x_n$ is the grid point position in the $x$ direction.

The smoothness of this interpolation can be improved by instead using a linear interpolant given by the convolution of $i_0$ with itself,

$$i_1(x) = \begin{cases} x + 1, & x \leq 0 \\ 1 - x, & x > 0. \end{cases}$$

Simplicity and smoothness may be maximally optimised by using a minimal set of contiguous piecewise polynomials or *B-spline* as an interpolant.

Our fluctuating density,

$$\delta n = \Omega \int \mathrm{d}^6 \bar{Z} \delta(\bar{\boldsymbol{X}} + \bar{\boldsymbol{\rho}} - \boldsymbol{x}) \delta \bar{F}',$$

is then

$$\delta n_{nm} = \sum_{o=1}^{N} w_o N_{\mathrm{g}o}^{-1} \sum_{p=1}^{N_{\mathrm{g}o}} i_3(\bar{\boldsymbol{x}}_o - \boldsymbol{x}_{nm}),$$

where $m \in \{1, \ldots, N_y\}$, $N_y$ is the number of grid points in the $y$ direction,

$$N_{\mathrm{g}} = \max[\mathrm{ceiling}(32 \bar{v}_\perp \bar{v}_{\mathrm{max}}^{-1}), 4]$$

is the $\bar{v}_\perp$-dependent or *adaptive* number of gyroaveraging points (Hatzky et al., 2002), $i_3$ is a cubic B-spline interpolant (Jolliet, 2009) and $\boldsymbol{x}_{nm}$ is the grid point position. The density and potential for a single marker are shown in Figures 3.2

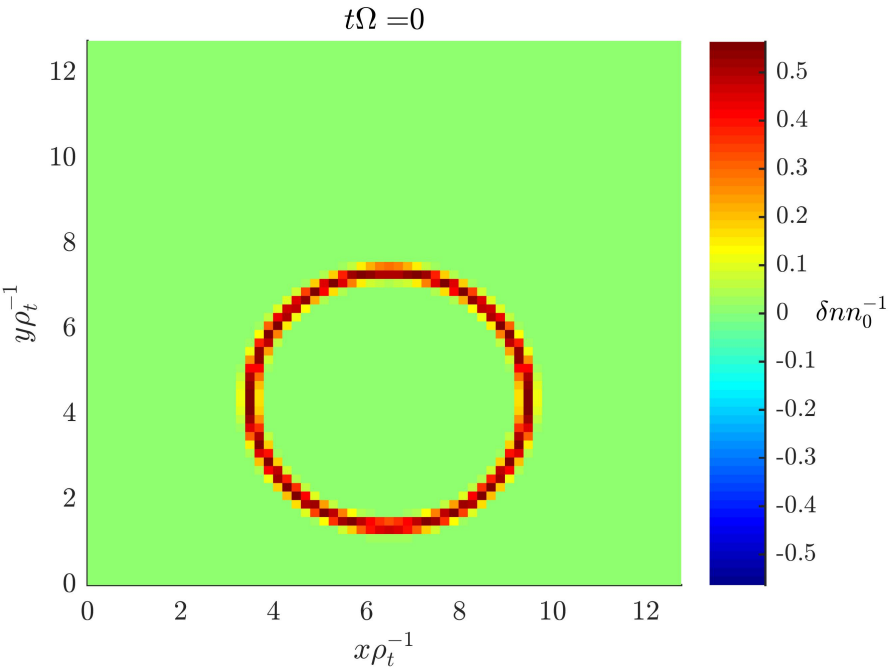


Figure 3.2: The fluctuating density for a single marker on the two-dimensional spatial gyrokinetic simulation domain. We see that markers do not represent pseudo particles but pseudo gyrorings.

and 3.3, respectively. We see that markers do not represent pseudo particles but psuedo gyrorings.

By using our $\delta f$ method (3.1) to linearise (Scott and Smirnov, 2010) our Poisson equation (2.57) up to first order, we obtain a Poisson equation that is identical to the weak-flow Poisson equation (Hahm, 1988) up to first order with uniform $\bar{F}_0'$ (2.68). By using this Poisson equation (2.68) with our quasineutrality equation (2.72), we find our $\boldsymbol{k}_\perp$-space fluctuating density (Dubin et al., 1983) as

$$\delta n_{\boldsymbol{k}_\perp} = T^{-1}[1 - I_0(Tk_\perp^2)e^{-Tk_\perp^2}]\phi_{\boldsymbol{k}_\perp},$$

where

$$\delta n_{\boldsymbol{k}_\perp} = \sum_{\boldsymbol{k}_\perp} \delta n e^{-i\boldsymbol{k}\cdot\boldsymbol{x}},$$

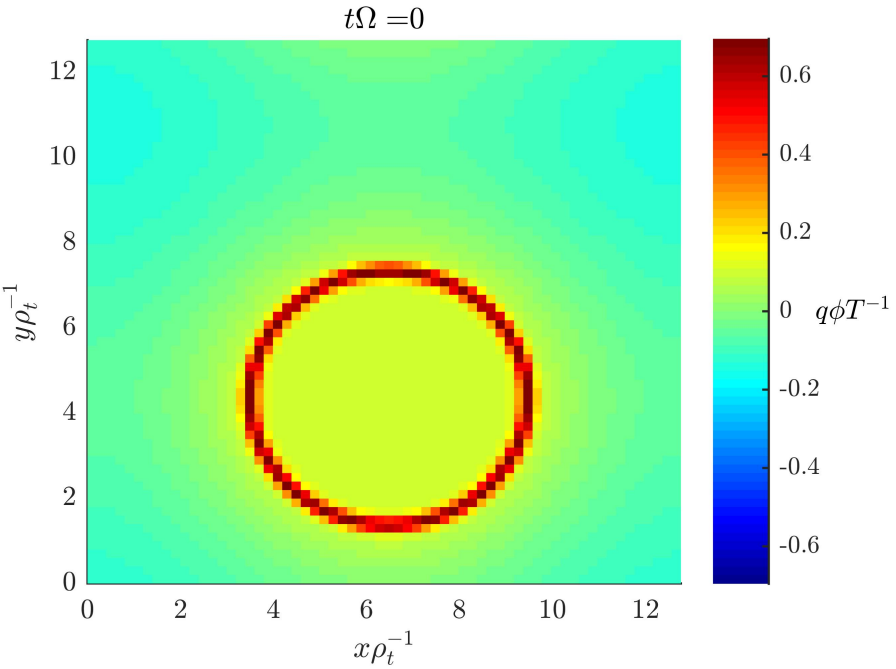


Figure 3.3: The fluctuating electrostatic potential for a single marker on the two-dimensional spatial gyrokinetic simulation domain. We see that markers do not represent pseudo particles but pseudo gyrorings.

$I_n$ is the modified Bessel function of the first kind, $n \in \mathbb{R}$ and

$$\phi_{\boldsymbol{k}_\perp} = \sum_{\boldsymbol{k}_\perp} \phi e^{-i\boldsymbol{k}\cdot\boldsymbol{x}}.$$

In general, spectral methods (Frigo and Johnson, 2005) have an error due to the finite discretised spectral range or *aliasing*.

We are now able to specify our potential initialisation. We now wish to use this to evolve the markers.

## 3.4 Vlasov equation

Our Vlasov equation depends implicitly on the time derivative of the potential. Thus, we evolve our markers by modifying our chosen fourth-order Runge-Kutta

time integrator such that it incorporates iteration.

### 3.4.1 Iterative solver

The fourth-order Runge-Kutta time integrator,

$$\boldsymbol{q}_{\mathrm{m}}(t+\Delta t) = \boldsymbol{q}_{\mathrm{m}}(t) + \tfrac{\Delta t}{6}(\boldsymbol{e}_1 + 2\boldsymbol{e}_2 + 2\boldsymbol{e}_3 + \boldsymbol{e}_4),$$

$$\boldsymbol{e}_1 = \dot{\boldsymbol{q}}_{\mathrm{m}}(\boldsymbol{q}_{\mathrm{m}}(t), t), \tag{3.9}$$

$$\boldsymbol{e}_2 = \dot{\boldsymbol{q}}_{\mathrm{m}}\big(\boldsymbol{q}_{\mathrm{m}}(t) + \tfrac{\Delta t}{2}\boldsymbol{e}_1, t + \tfrac{\Delta t}{2}\big), \tag{3.10}$$

$$\boldsymbol{e}_3 = \dot{\boldsymbol{q}}_{\mathrm{m}}\big(\boldsymbol{q}_{\mathrm{m}}(t) + \tfrac{\Delta t}{2}\boldsymbol{e}_2, t + \tfrac{\Delta t}{2}\big), \tag{3.11}$$

$$\boldsymbol{e}_4 = \dot{\boldsymbol{q}}_{\mathrm{m}}(\boldsymbol{q}_{\mathrm{m}}(t) + \Delta t\boldsymbol{e}_3, t + \Delta t), \tag{3.12}$$

where $\Delta t$ is the time step, uses evaluations of the potential and its derivatives at the beginning (3.9), middle (3.10, 3.11) and end (3.12) of the time-step interval. The evaluation of the potential and its spatial derivatives at these points (3.9, 3.10, 3.11, 3.12) does not pose a problem.

However, in order to evaluate the time derivative of the potential at these points (3.9, 3.10, 3.11, 3.12), it is necessary, and sufficient, to additionally evaluate the potential, and some of its spatial derivatives, at time $t + \frac{\Delta t}{4}$ within the time-step interval,

$$\boldsymbol{e}_0 = \dot{\boldsymbol{q}}_{\mathrm{m}}\big(\boldsymbol{q}_{\mathrm{m}}(t) + \tfrac{\Delta t}{4}\boldsymbol{e}_1, t + \tfrac{\Delta t}{4}\big). \tag{3.13}$$

The evaluation of the time derivative of the potential at the beginning (3.9) and middle (3.10, 3.11) of the time-step interval can be computed from forward,

$$\dot{\phi}(t) = \big(\tfrac{\Delta t}{4}\big)^{-1}\big[\phi\big(t + \tfrac{1}{4}\Delta t\big) - \phi(t)\big], \tag{3.14}$$

and backward,

$$\dot{\phi}\big(t + \tfrac{1}{2}\Delta t\big) = \big(\tfrac{1}{4}\Delta t\big)^{-1}\big[\phi\big(t + \tfrac{1}{2}\Delta t\big) - \phi\big(t + \tfrac{1}{4}\Delta t\big)\big],$$

differences, respectively, that use this additional evaluation point (3.13). The

evaluation of the time derivative of the potential at the end of the time-step interval (3.12) can be computed from a backward difference that uses the evaluations at the middle of the time-step interval (3.10, 3.11),

$$\dot{\phi}(t+\Delta t) = \left(\tfrac{1}{2}\Delta t\right)^{-1}\left[\phi(t+\Delta t) - \phi\left(t+\tfrac{1}{2}\Delta t\right)\right].$$

We can create the additional evaluation point (3.13) by iterating a quarter Euler time step,

$$\boldsymbol{q}_m(t+\tfrac{1}{4}\Delta t) = \boldsymbol{q}_m(t) + \tfrac{\Delta t}{4}\dot{\boldsymbol{q}}_m(\boldsymbol{q}_m(t), t),$$

and a forward-difference evaluation of the time derivative of the potential (3.14), where the first iteration neglects the polarisation drift and each iteration uses the closest known value of the marker phase-space volume (3.4). The spatial derivatives of the potential evaluated at the beginning of the time-step interval are precomputed outside of this iteration loop.

Each of the original integrator evaluations (3.9, 3.10, 3.11, 3.12) are then iterated with each iteration using the closest known value of the marker phase-space volume (3.4).

In general, we expect the accuracy of our modified time integrator to be less than that of the standard one.

For non-uniform $\bar{F}_0'$, we may consider simply using our $\delta f$ method (3.1) to find the time derivative of $\delta\bar{F}'$ as

$$\begin{aligned}\dot{\delta\bar{F}}' &= -\dot{\bar{F}}_0' \\ &= -\dot{\bar{R}}_1 L_{\mathrm{n}}^{-1}\bar{F}_0' - \bar{F}_0'\bar{u}(\partial_t + \bar{\boldsymbol{u}}\cdot\bar{\boldsymbol{\nabla}})\bar{u} \\ &= -\dot{\bar{R}}_1 L_{\mathrm{n}}^{-1}\bar{F}_0' + \mathcal{O}(\epsilon^2),\end{aligned} \tag{3.15}$$

where $L_{\mathrm{n}} \gg L_x$ is the density nonuniformity length scale in the $x$ direction.

We now present convergence studies for our iterative method.

**Convergence**

Our convergence simulations used $2^{23}$ markers. A circularly symmetric solution, as shown in Figures 3.4 and 3.5, is a static solution of our Vlasov-Poisson system.

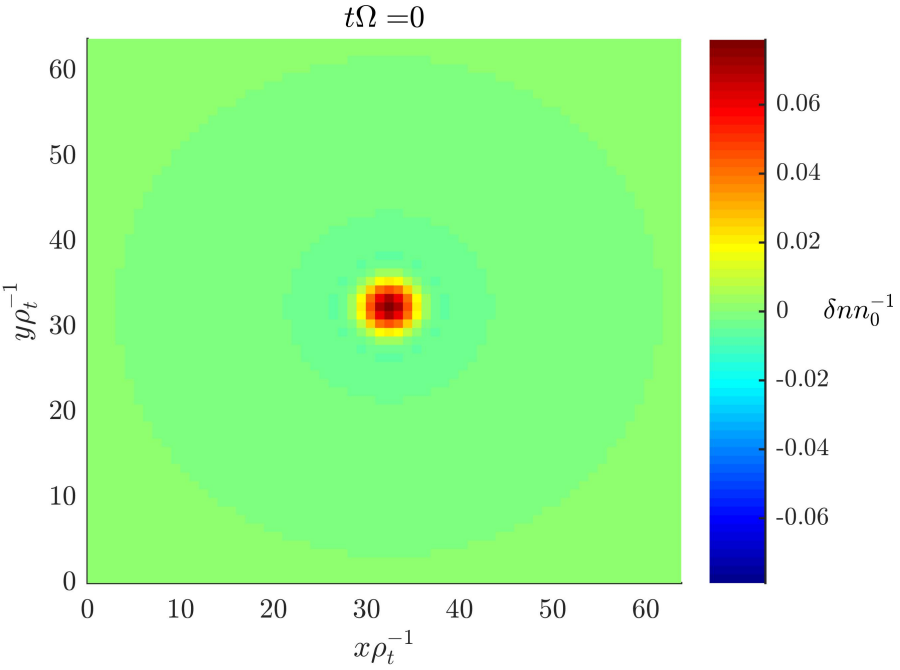


Figure 3.4: The fluctuating density associated with a circularly symmetric solution of the Vlasov-Poisson system on the two-dimensional spatial gyrokinetic simulation domain. The simulation parameters are as in Subsection 3.4.1.

This static potential solution can be modified to give a dynamic solution by adding a constant to the equation for $\dot{\bar{X}}_1$ (2.33) such that we have $\bar{\boldsymbol{u}} \sim 1$.

The relative error per iteration is shown in Figure 3.6. The convergence ratio per iteration is of order $\epsilon$.

We present the verification of our code in the next section.

## 3.5 Verification

We first present weak- and then strong-flow code verification.

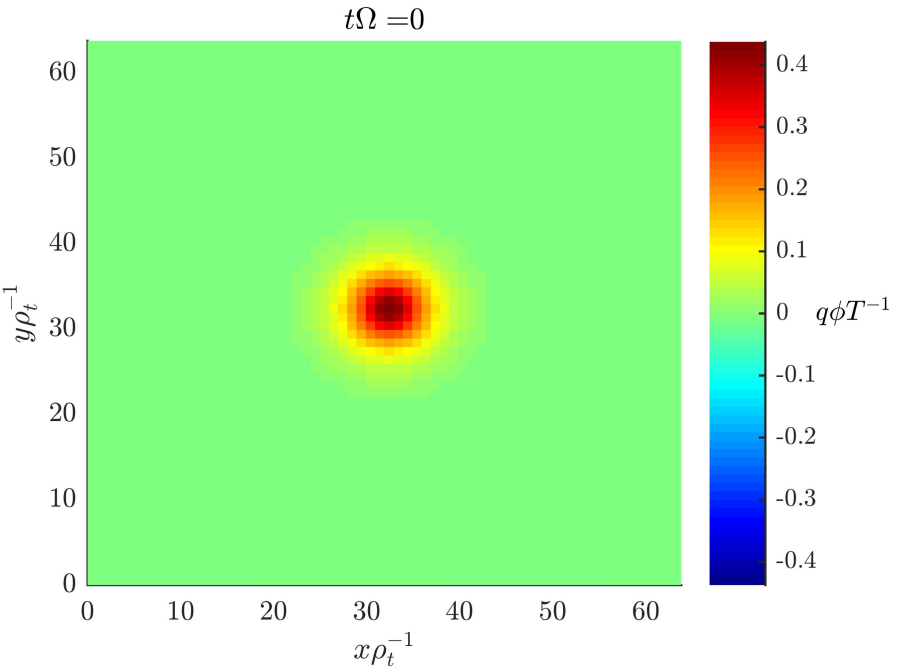


Figure 3.5: The fluctuating electrostatic potential associated with a circularly symmetric solution of the Vlasov-Poisson system on the two-dimensional spatial gyrokinetic simulation domain. The simulation parameters are as in Subsection 3.4.1.

### 3.5.1 Weak flows

As described in Subsection 2.7.1, the Hasegawa-Mima equation is a limiting case of our Vlasov-Poisson system. The Hasegawa-Mima equation exhibits cascade and inverse cascade phenomena (Horton and Hasegawa, 1994). Specifically, the mode coupling coefficient contains the factor $\hat{\boldsymbol{b}} \cdot \boldsymbol{k}_1 \times \boldsymbol{k}_2$, where $\boldsymbol{k}_1$ and $\boldsymbol{k}_2$ are the wavevectors of two modes. Analytic linear growth rates may be computed (Horton and Hasegawa, 1994) by using

$$|\phi_{\boldsymbol{k}_1}| \gg |\phi_{\boldsymbol{k}_2}| \sim |\phi_{\boldsymbol{k}_3}| \gg |\phi_{\boldsymbol{k}_n}|, n \neq 1, 2, 3, \tag{3.16}$$

where $\phi_{\boldsymbol{k}_m}$ is the complex Fourier mode amplitude and $n, m \in \mathbb{Z}^+$.

Weak-flow verification was performed by computing linear simulated and

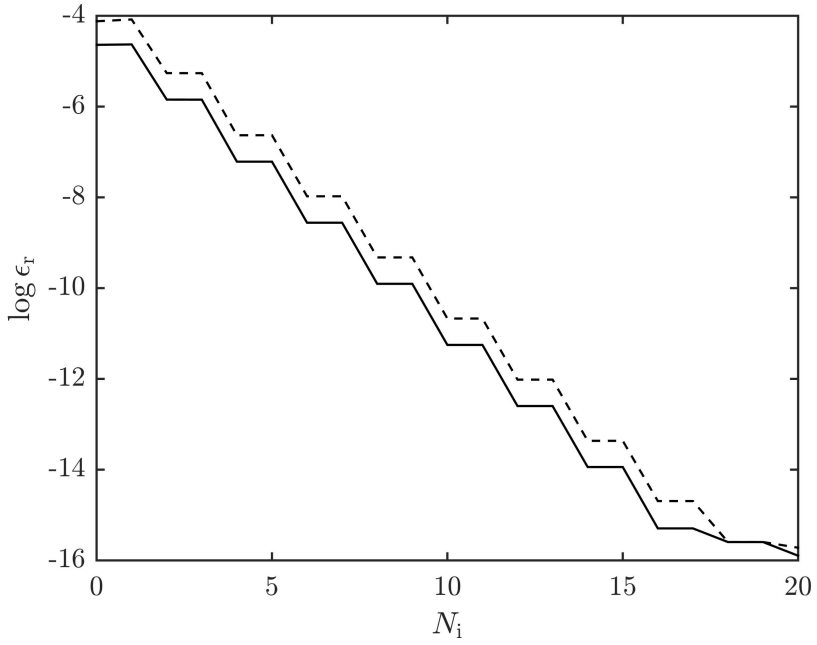


Figure 3.6: The logarithm of the relative error $\epsilon_r$ as a function of the number of iterations $N_i$ in the iterative forth-order Runge-Kutta time integrator for time step $\Delta t = \Omega^{-1}$ (solid), $2\Omega^{-1}$ (dashed). The simulation parameters are as in Subsection 3.4.1.

semi-analytic Kelvin-Helmholtz instability growth-rate spectra. The Kelvin-Helmholtz instability is brought about by the presence of velocity shear and manifests as the exponential growth of the perturbation of a shear layer.

The simulations used $2^{24}$ markers, cold ions, adiabatic electrons, a uniform background ion density, $\Delta t = 1$ and $N_i = 0$. The potential was initialised to contain background and perturbation sinusoidal components in the $y$ and $x$ directions, respectively,

$$\phi = A(\sin k_y y + 10^{-4} \cos k_x x),$$

where $A$ is the background potential amplitude, and $k_x$ and $k_y$ are the wavenumbers in the $x$ and $y$ directions, respectively. An example potential initialisation

is shown in Figures 3.7 and 3.8, where the magnetic field is in the $z$ direction, the flow is in the $x$ direction and there is velocity shear in the $y$ direction.

The evolution is such that the perturbed and coupled modes grow exponentially, as shown in Figures 3.7 and 3.8. We see that we have many growing modes. Thus, we do expect agreement with analytic, three-wave-coupling linear growth rates (3.16). Examples of the late time, saturated state of these simulations is shown in Figures 3.9 and 3.10.

Distinct transient, linear and nonlinear evolutionary periods are visible in the evolution of the growth rate of the perturbation, as shown, for example, in Figures 3.11 and 3.12. Whilst we do not expect agreement with analytic, three-wave-coupling linear growth rates (3.16), we do expect agreement with semi-analytic linear growth rates computed in a similar manner to that of Rogers and Dorland (2005).

During the linear period, our potential is given by

$$\phi_{\mathrm{a}} = A\sin(k_y y) + e^{\gamma t + ik_x x}\sum_{n=-\infty}^{\infty}\phi_n e^{ink_y y}, \tag{3.17}$$

where $\gamma$ is the linear growth rate and $i$ in an exponent is the imaginary unit. By substituting this potential (3.17) into the Hasegawa-Mima equation (2.77), we obtain the eigenvalue equation

$$\sum_{n=-\infty}^{\infty}(\gamma(n^2k_y^2+k_x^2+1)+iAk_xk_y((n^2-1)k_y^2+k_x^2)\cos(k_y y))\phi_n e^{ink_y y} = 0. \tag{3.18}$$

By using

$$\sum_{n=-\infty}^{\infty}\phi_n e^{ink_y y} = \sum_{n=0}^{\infty}a_n\cos nk_y y + \sum_{n=1}^{\infty}b_n\sin nk_y y$$

and the orthogonality of sine and cosine, the eigenvalue equation (3.18) can be written in the form

$$M\boldsymbol{a} = \gamma\boldsymbol{a}, \tag{3.19}$$

where $M \in \mathbb{C}^{n\times n}$ is an infinite square matrix, $n \in \mathbb{Z}^+$, $\boldsymbol{a} = a_m$ and $m \in \mathbb{Z}^*$. The

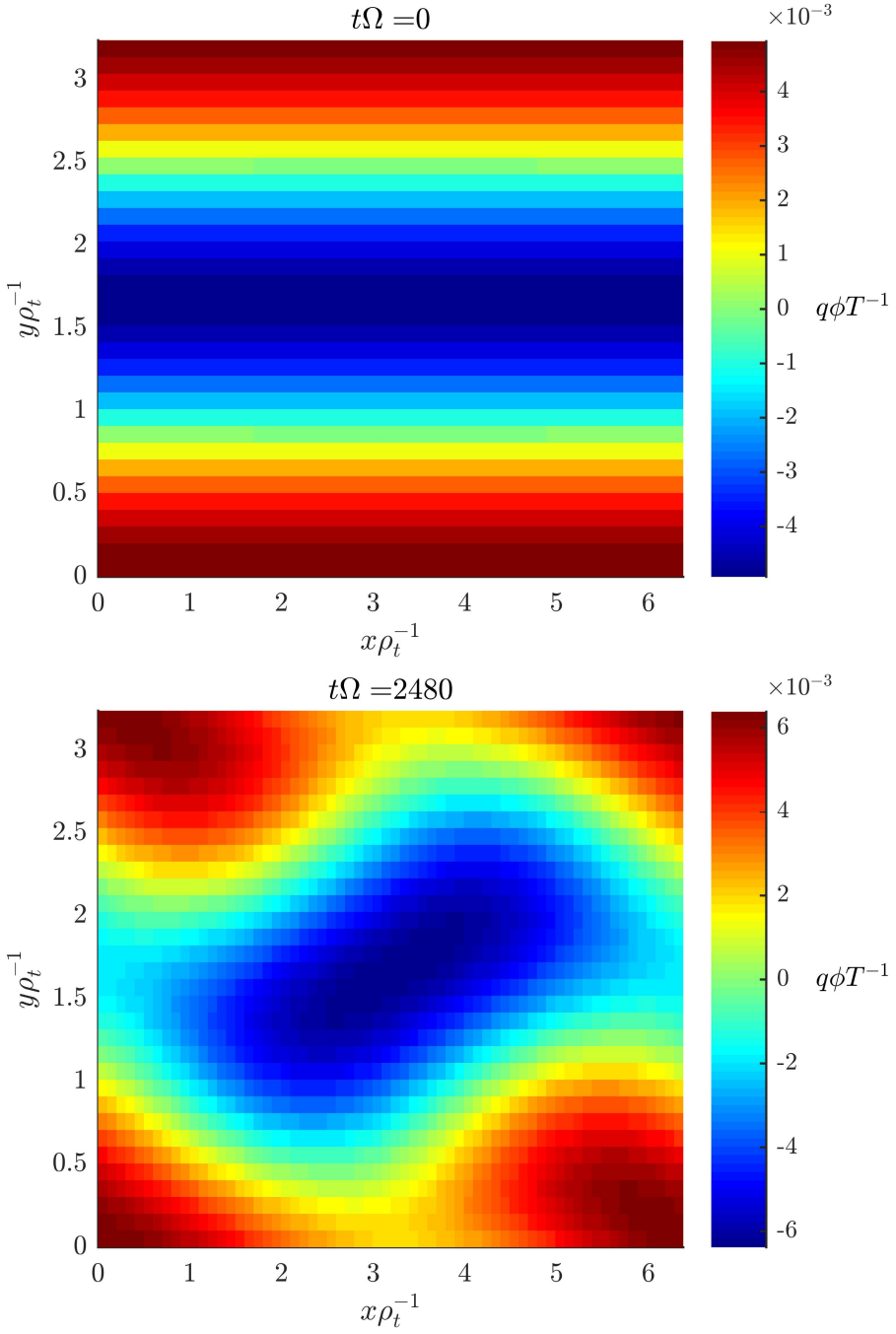


Figure 3.7: The fluctuating electrostatic potential on the two-dimensional spatial domain at the start (top) and transition from the linear to the nonlinear period (bottom) of the gyrokinetic simulation of the Kelvin-Helmholtz instability. The simulation parameters are as in Subsection 3.5.1.

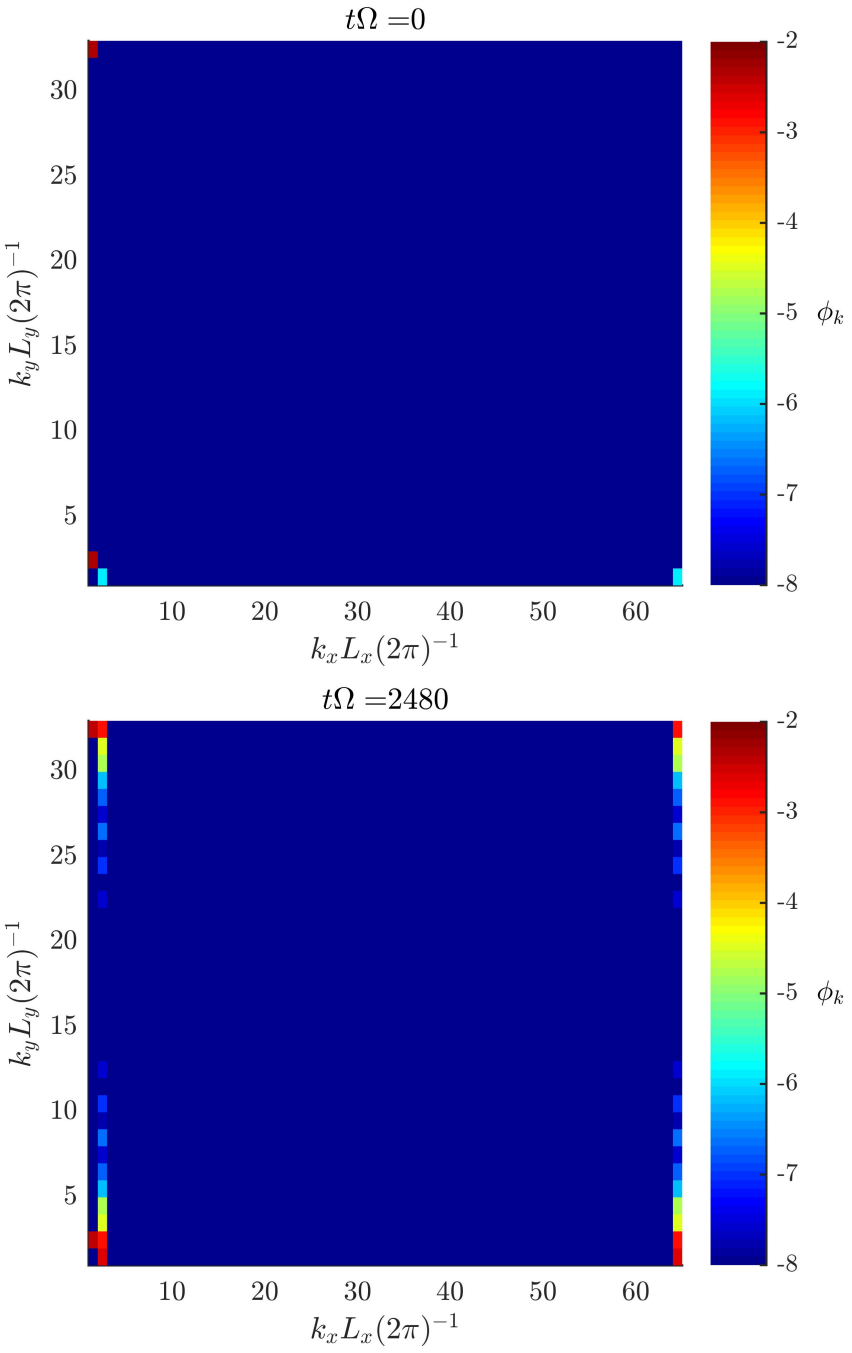


Figure 3.8: The Fourier-space fluctuating electrostatic potential at the start (top) and transition from the linear to the nonlinear period (bottom) of the gyrokinetic simulation of the Kelvin-Helmholtz instability. The simulation parameters are as in Subsection 3.5.1.

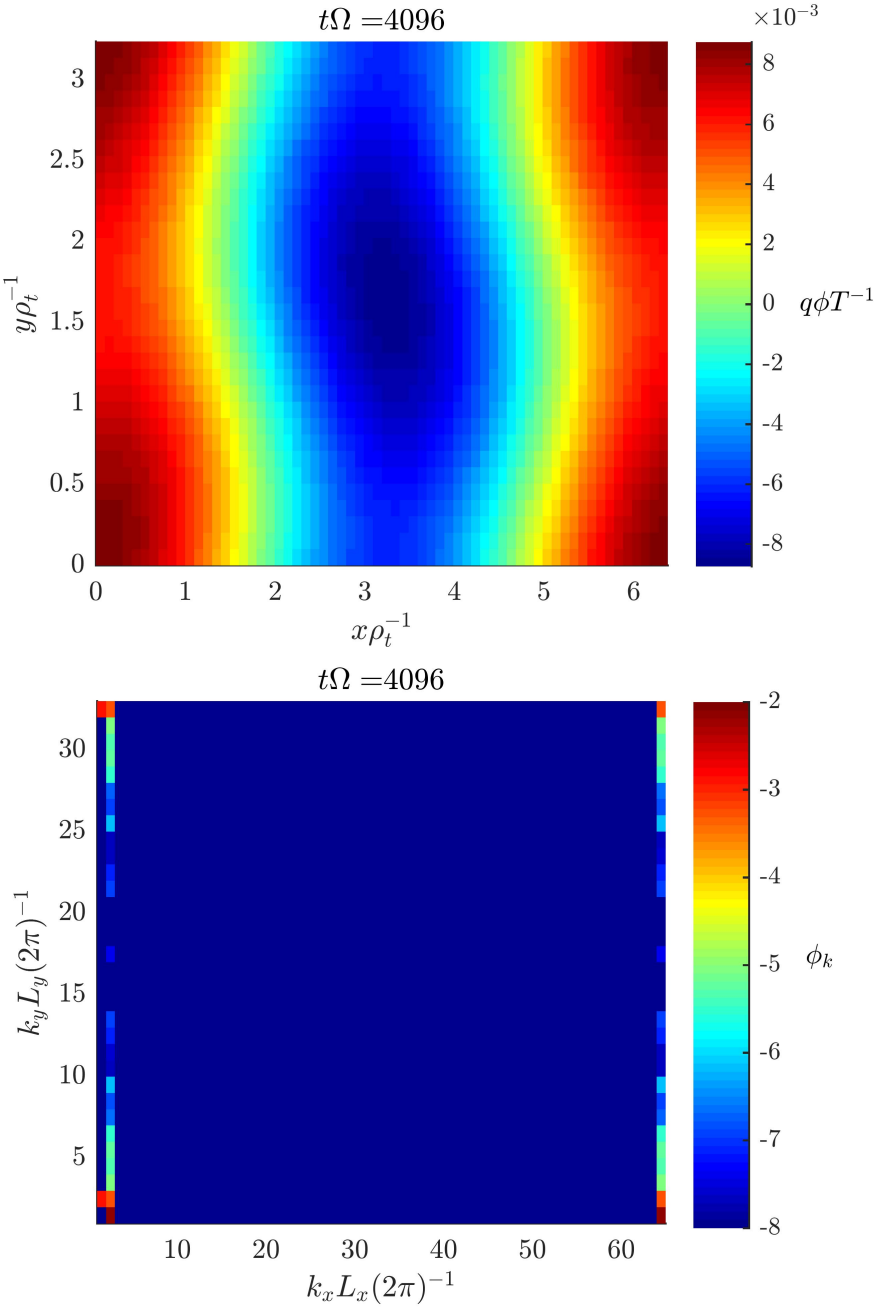


Figure 3.9: The saturated two-dimensional fluctuating electrostatic potential in real (top) and Fourier (bottom) space early in the nonlinear period of a gyrokinetic simulation of the Kelvin-Helmholtz instability. The simulation parameters are as in Subsection 3.5.1.

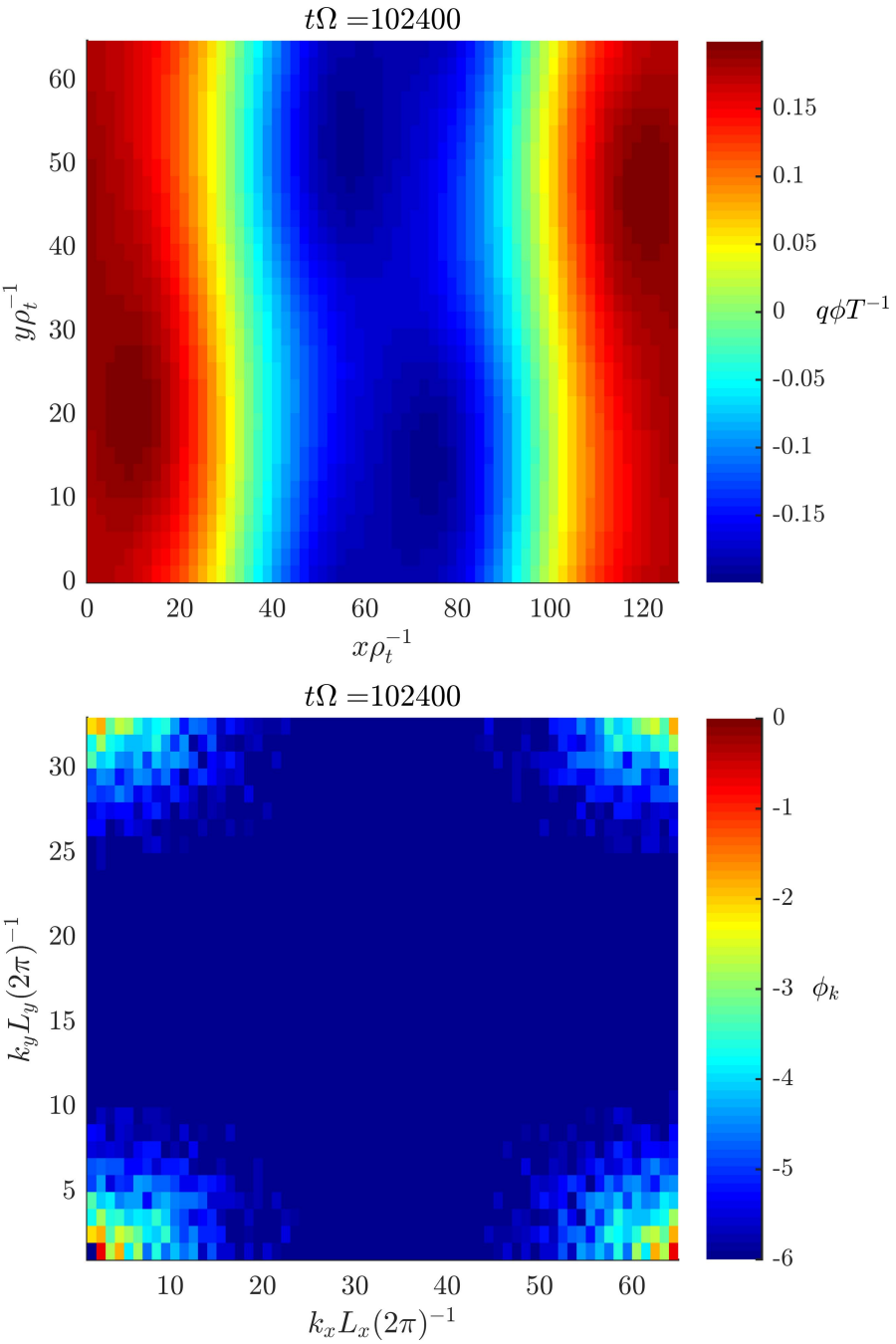


Figure 3.10: The saturated two-dimensional fluctuating electrostatic potential in real (top) and Fourier (bottom) space late in the nonlinear period of a gyrokinetic simulation of the Kelvin-Helmholtz instability. The simulation parameters are as in Subsection 3.5.1.

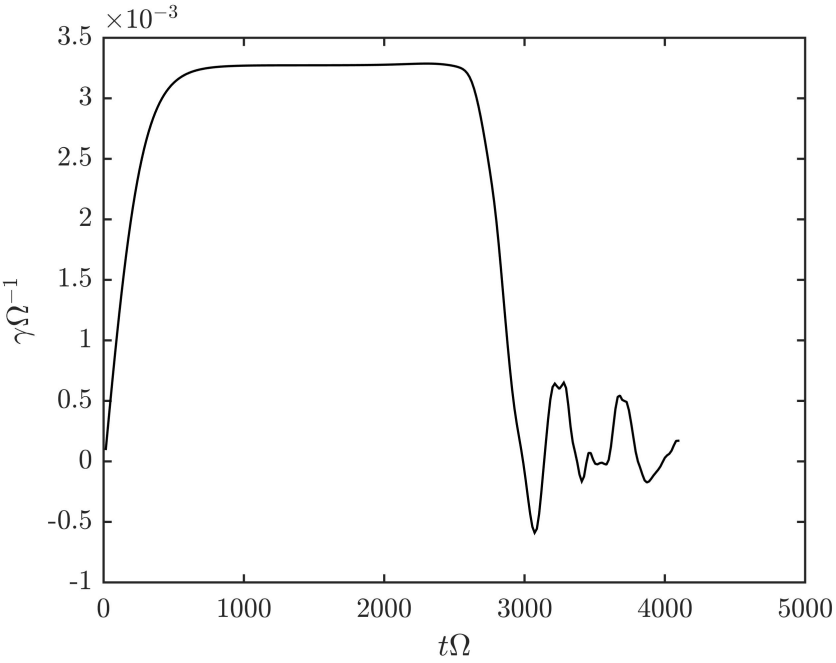


Figure 3.11: The fluctuating electrostatic potential perturbation growth-rate evolution during a Kelvin-Helmholtz instability. The simulation parameters are as in Subsection 3.5.1.

eigenvalue equation in this form (3.19) can be solved numerically by computing the maximum real eigenvalues of a truncation of $M$ that corresponds to our finite dicretised spectral range.

The simulated, semi-analytic (3.19) and analytic (3.16) linear Kelvin-Helmholtz instability growth-rate spectra are shown in Figure 3.13. As expected, we only have good quantitative agreement between the simulated and semi-analytic (3.19) spectra.

Our simple implementation (3.15) of nonuniformity in $\bar{F}_0'$ agrees with the drift-wave velocity (Horton and Hasegawa, 1994) given by the Hasegawa-Mima equation for $k_\perp \rho_\mathrm{t} \sim \epsilon$, with a relative error of $4.72 \times 10^{-2}$.

We present the strong-flow verification of our code in the next subsection.

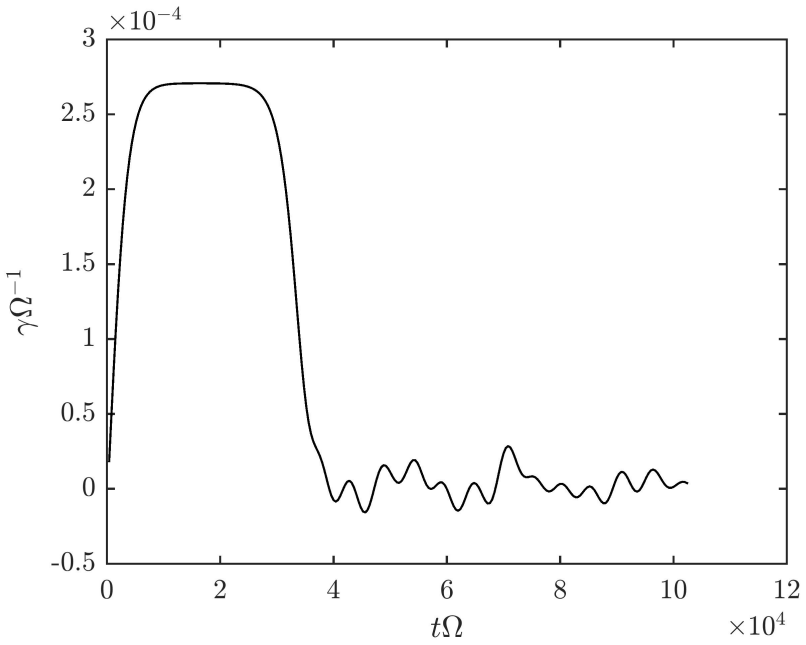


Figure 3.12: The fluctuating electrostatic potential perturbation growth-rate evolution during a Kelvin-Helmholtz instability. The simulation parameters are as in Subsection 3.5.1.

### 3.5.2 Strong flows

Strong-flow verification was performed by comparing the simulated and analytic Kelvin-Helmholtz instability growth-rate spectra of a shear layer.

Strong-flow verification simulations used $2^{23}$ markers, $\Delta t = 1$ and $N_\mathrm{i} = 16$. The potential was initialised to contain a shear layer with $\bar{\boldsymbol{u}} \sim 1$ dominated by a single sign of the parallel vorticity and a sinusoidal perturbation in the $y$ and $x$ directions, respectively. An example initialisation is shown in Figures 3.14 and 3.15.

The evolution is such that the perturbation grows exponentially, as shown in Figure 3.14. Distinct evolutionary periods are visible in the evolution of the growth rate of the perturbation, as shown in Figure 3.16. We can compare the linear-period Kelvin-Helmholtz growth rate to that of an FLR MHD analysis of a thin, incompressible shear layer (Nagano, 1978).

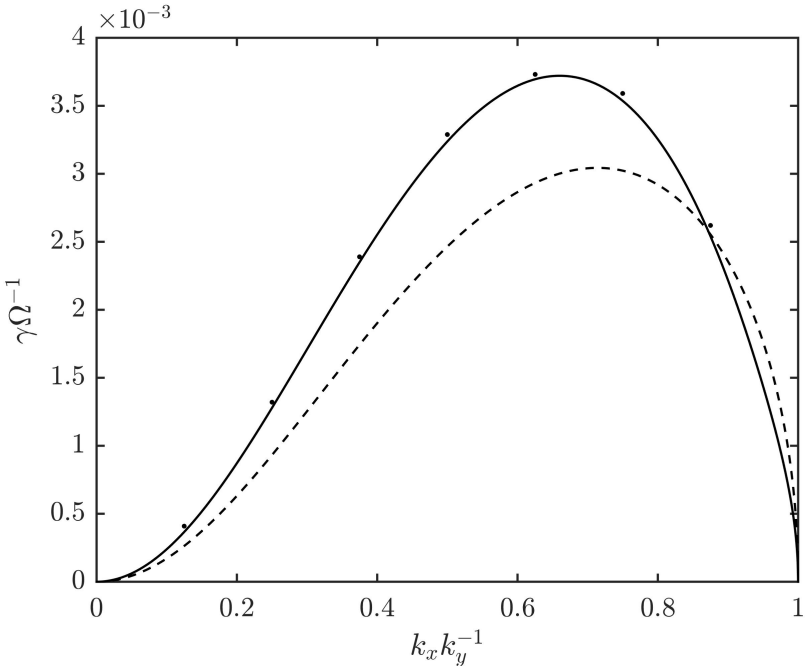


Figure 3.13: The simulated (points), semi-analytic (3.19) (solid) and analytic (3.16) (dashed) linear Kelvin-Helmholtz instability growth-rate spectra. The simulation parameters are as in Subsection 3.5.1.

From Nagano (1978), the positive and negative parallel vorticity growth rates are given by

$$\gamma_{\pm} = \left(\bar{u}^2 k_x^2 \mp \tfrac{1}{2}\rho_{\mathrm{t}}^2 \Omega \bar{u} |k_x^3|\right)^{\frac{1}{2}}, \tag{3.20}$$

respectively. The dependence on the sign of the parallel vorticity is due to the chirality of gyromotion (Nagano, 1978; Gingell et al., 2012). That is to say, the net flow depends on whether the shear flow and gyromotion are correspondent. The asymmetry is manifest in our Vlasov equation (2.33, 2.34, 2.69) through $\bar{\Omega}_{\parallel}^{*}$ (2.31). The effect has also been observed with hybrid models (Gingell et al., 2012). It can be thought of as FLR or strong-flow symmetry breaking.

The simulated and analytic growth-rate spectra are shown in Figure 3.17. We have good qualitative agreement between these spectra, with the changes in the growth rate with the sign of the parallel vorticity having a relative error of

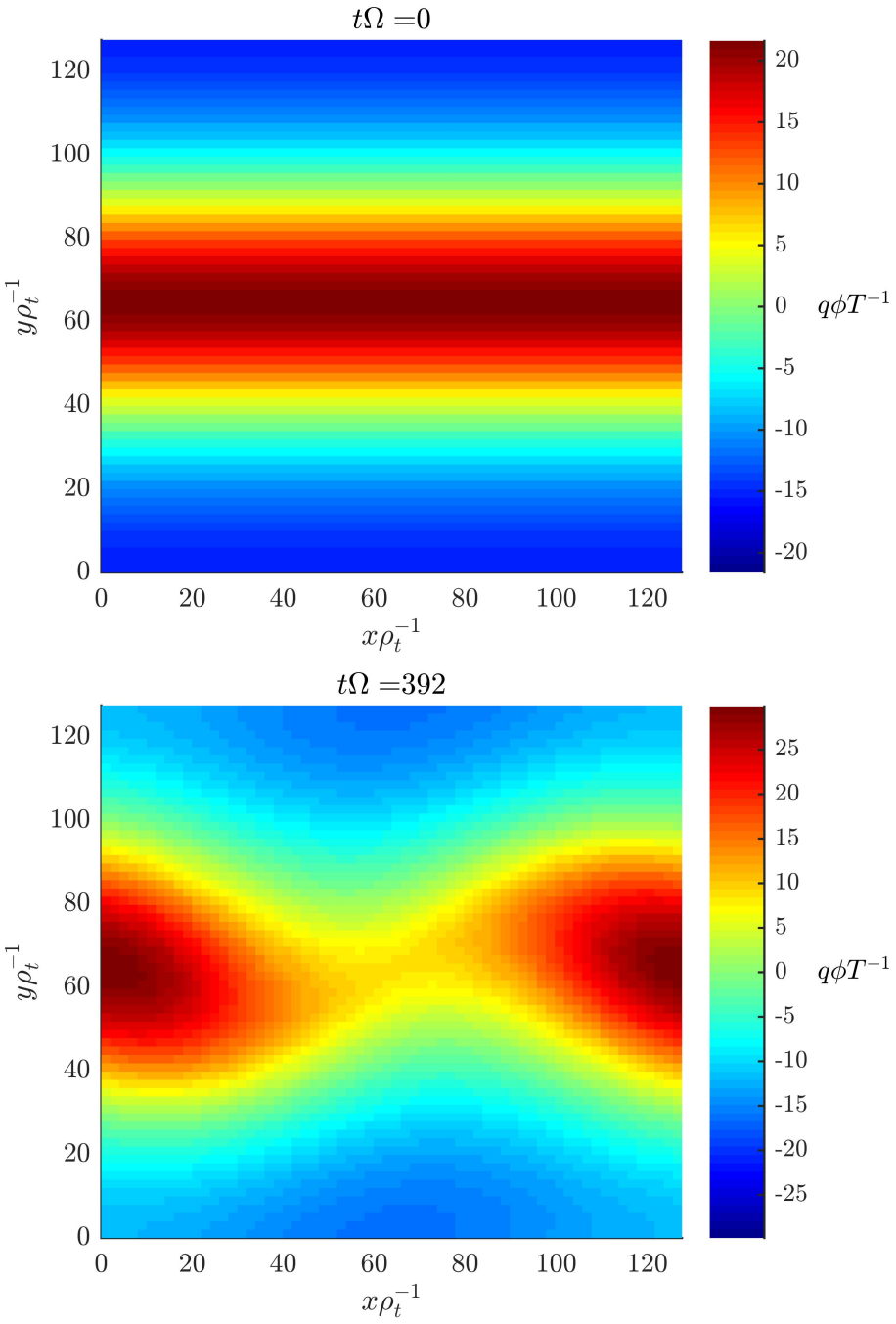


Figure 3.14: The fluctuating electrostatic potential on the two-dimensional spatial domain at the start (top) and transition from the linear to the nonlinear period (bottom) of the gyrokinetic simulation of a Kelvin-Helmholtz unstable shear layer. The simulation parameters are as in Subsection 3.5.2.

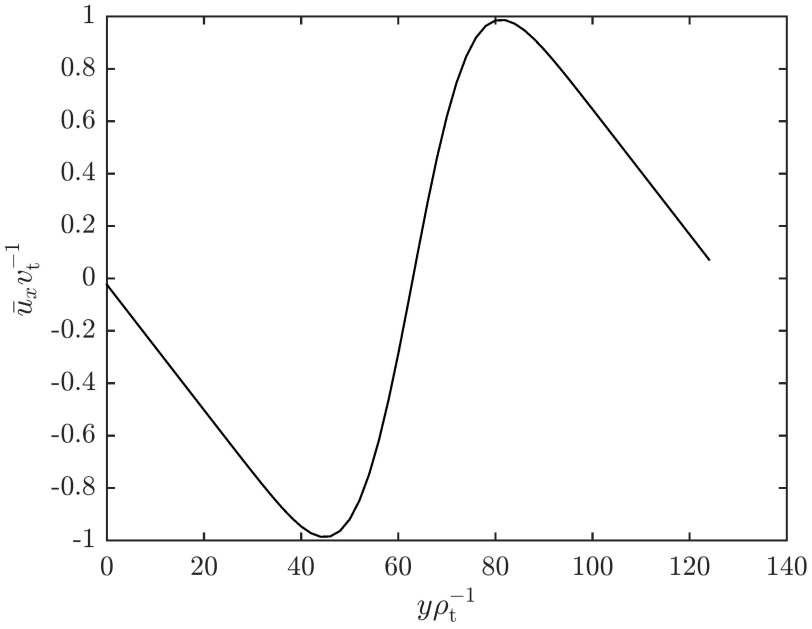


Figure 3.15: The gyroaveraged E × B velocity initialisation in the $y$ direction of the gyrokinetic simulation of a Kelvin-Helmholtz unstable shear layer. Simulation parameters are as in Subsection 3.5.2.

0.488.

We present the applications of our code to more general scenarios in the next chapter.

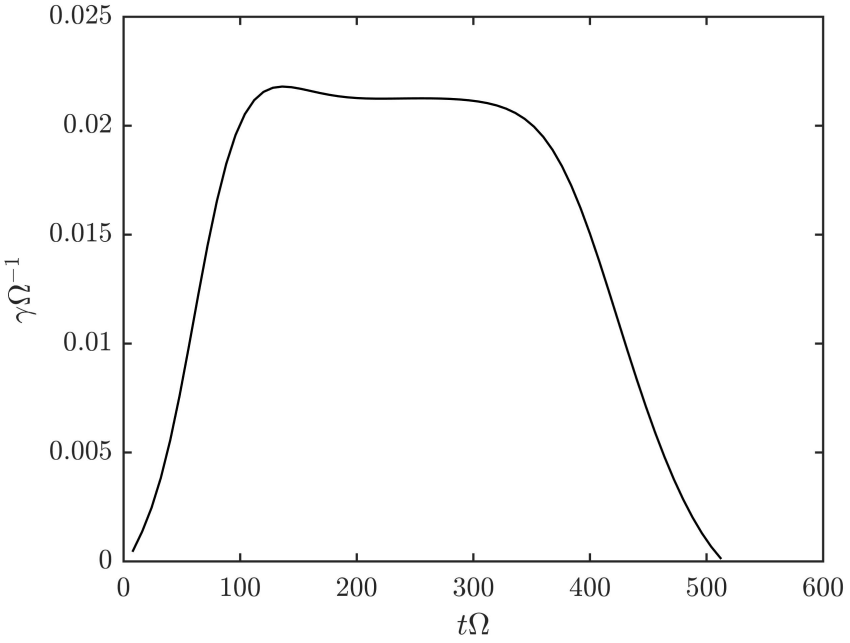


Figure 3.16: The fluctuating electrostatic potential perturbation growth-rate evolution during a Kelvin-Helmholtz instability of a shear layer. The simulation parameters are as in Subsection 3.5.2.

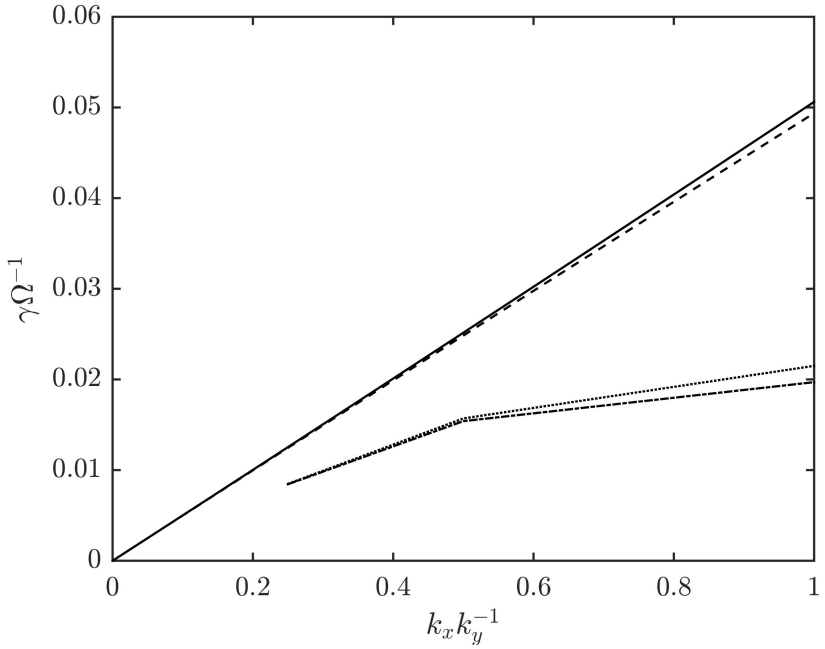


Figure 3.17: The negative and positive parallel vorticity analytic (3.20) (solid and dashed, respectively) and simulated (dotted and dot-dashed, respectively) Kelvin-Helmholtz instability growth-rate spectra of a shear layer. The simulation parameters are as in Subsection 3.5.2.

# Chapter 4

# Applications

We have applied our code to more general shear layers as well as plasma filaments or *blobs*, as shown in Figures 4.1 and 4.2, respectively. The edge of tokamak

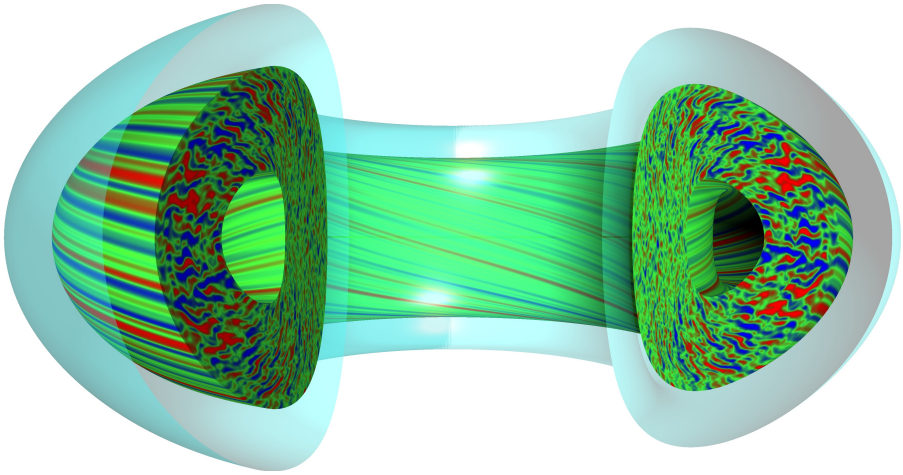

Figure 4.1: A classic, GYRO tokamak simulation showing multiple shear layers (Candy, 2008).

plasmas is associated with the formation and propagation of these blobs, as shown in Figures 4.3 and 4.4. The propagation is due to $\nabla B$ polarisation and is in the major radial direction of a tokamak torus, as shown in Figures 4.5 and 4.6. The damage to tokamaks caused by blobs motivates the understanding of, for example, blob transport.

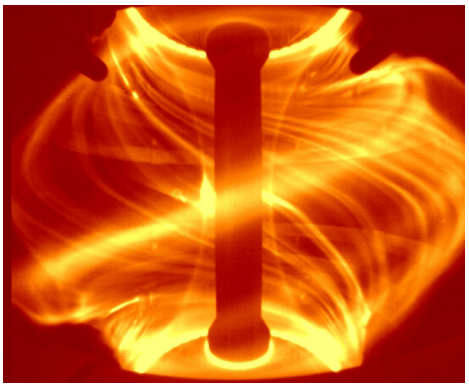

Figure 4.2: A Mega Ampère Spherical Tokamak shot showing plasma filaments or *blobs* during an edge localised mode (Kirk, 2012).

We may investigate the effects of strong-flows on blob transport by assuming that blob formation and $\boldsymbol{\nabla} B$ polarisation has already transpired. Thus, we model a blob simply as a dipole potential, as in Figures 4.4 and 4.5.

We first consider more general shear layer scenarios in the next section.

## 4.1 Shear layer

In order to aid analytic comparison, the shear layer simulations presented in Subsection 3.5.2 were initialised to be dominated by a single sign of parallel vorticity. In this section, we will present more general simulations of the Kelvin-Helmholtz instability of a shear layer.

The simulations used $2^{23}$ markers, $N_\mathrm{i} = 16$ and $\Delta t = 1$. The potential was initialised to contain a shear layer and a sinusoidal perturbation in the $y$ and $x$ directions, respectively. Example potential initialisations are shown in Figures 4.7 and 4.8.

The evolution is analogous to that of our simpler shear layers in the previous chapter, as shown in Figures 4.7 and 4.8. Additionally, by visual inspection, we observe that the weak-flow evolution accords with the symmetry

$$\phi(x, y) = -\phi(-x, -y), \tag{4.1}$$

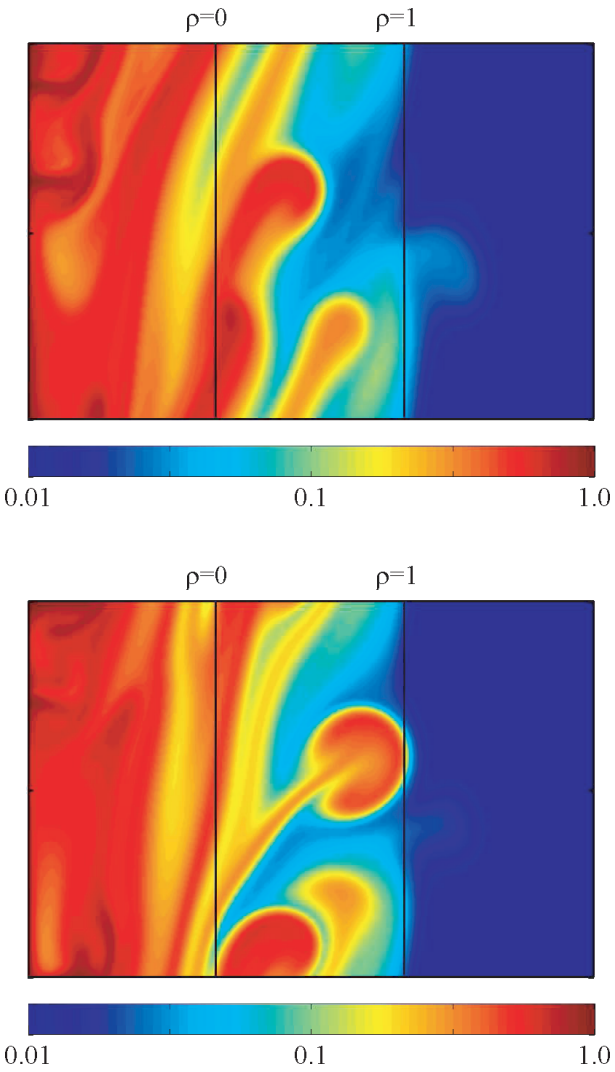


Figure 4.3: A simulation showing plasma filament or *blob* formation in terms of density on a $150\rho_t \times 100\rho_t$ spatial domain, where the bottom panel is at a time $30\Omega^{-1}$ after that of the top panel and, here, $\rho = 0$ denotes the last closed flux surface and $\rho = 1$ denotes the wall radius (Garcia, 2009).

as shown in Figure 4.7. However, for strong flows, we do not observe this symmetry (4.1) and instead have strong-flow or, equivalently, FLR symmetry breaking with

$$\phi(x, y) \neq -\phi(-x, -y), \tag{4.2}$$

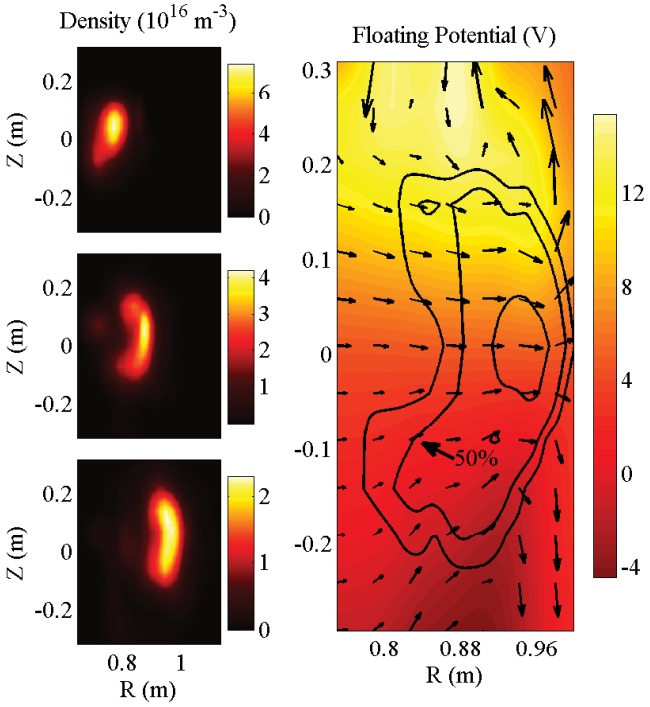


Figure 4.4: An experimental observation of the cross section of a plasma filament or *blob* in terms of density at three different times each separated by 100$\mu$s (left) and floating potential with density and velocity overlaid (right) (Katz et al., 2008).

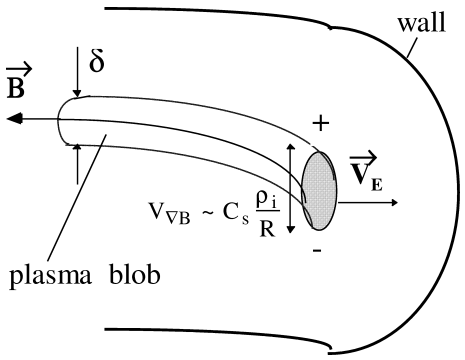


Figure 4.5: $\nabla B$ polarisation and propagation of a blob (Krasheninnikov, 2001).

as shown in Figure 4.8.

Given our constant electron density (2.73), the fluctuating density may be used as a proxy for the parallel vorticity. Thus, we may examine the mono-

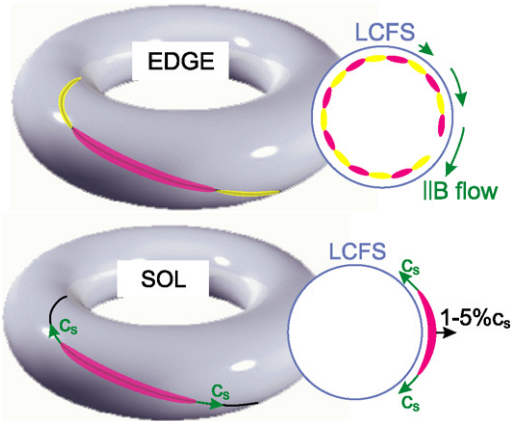


Figure 4.6: Blob propagation through the edge, last closed flux surface (LCFS) and scrape-off layer (SOL), where $c_s$ is the sound speed (Naulin, 2007).

tonically increasing weak- and strong-flow parallel vorticity at the end-state of the simulation. This is shown in Figures 4.9 and 4.10. For weak flows, the distribution of parallel vorticity is symmetric. For strong flows, the magnitudes of the positive values of the parallel vorticity peak more than those of the negative values, however, there is a greater spread in the negative than the positive values of the parallel vorticity.

We consider a circularly symmetric shear layer in the next subsection.

### 4.1.1 Circular symmetry

We may examine the Kelvin-Helmholtz instability of a shear layer with circular symmetry.

The simulations used $2^{23}$ markers, $N_i = 16$ and $\Delta t = 1$. The potential was initialised to contain a circularly symmetric shear layer. An example initialisation is shown in Figures 4.11 and 4.12.

The circularly symmetric shear layer is Kelvin-Helmholtz unstable, as shown in Figures 4.11 and 4.12. Once again, we have the symmetric, weak-flow evolution (4.1), as shown in Figures 4.13, 4.14, 4.15 and 4.16, and the asymmetric, strong-flow evolution (4.2), as shown in Figures 4.17, 4.18, 4.19 and 4.20.

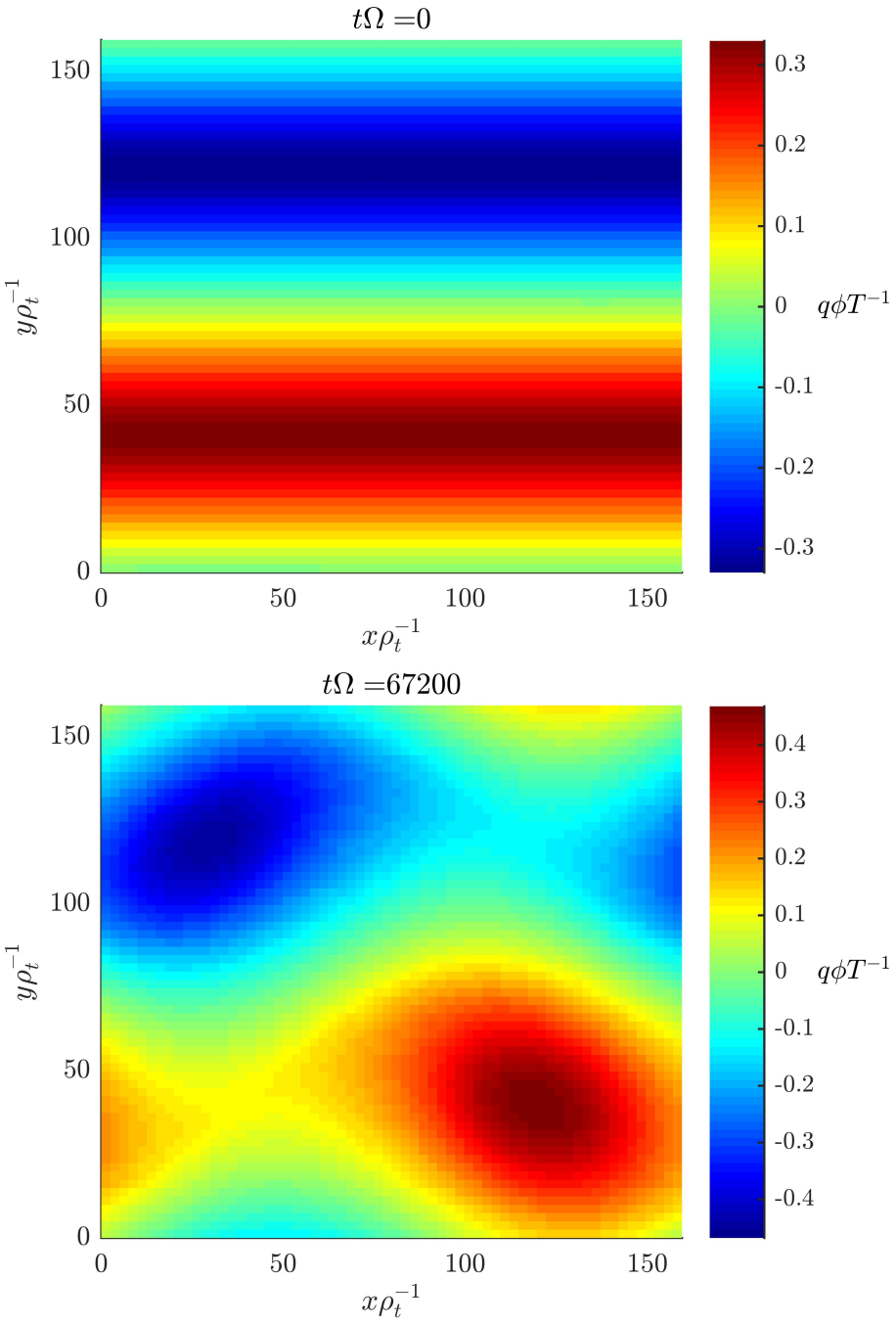


Figure 4.7: The weak-flow fluctuating electrostatic potential initialisation (top) and symmetric evolution (bottom) of a Kelvin-Helmholtz unstable shear layer on the two-dimensional spatial gyrokinetic simulation domain. The simulation parameters are as in Section 4.1.

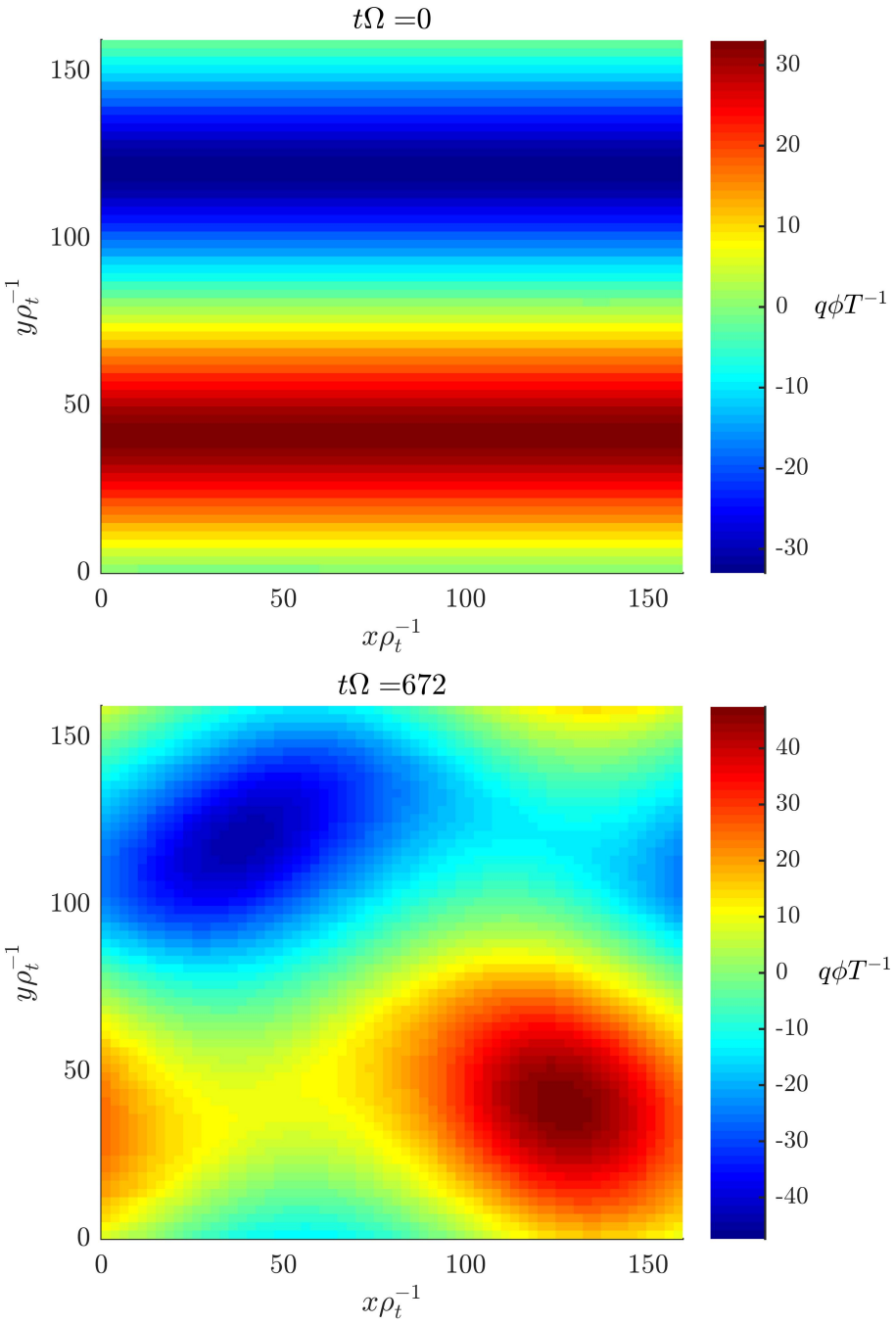


Figure 4.8: The strong-flow fluctuating electrostatic potential initialisation (top) and asymmetric evolution (bottom) of a Kelvin-Helmholtz unstable shear layer on the two-dimensional spatial gyrokinetic simulation domain. The simulation parameters are as in Section 4.1.

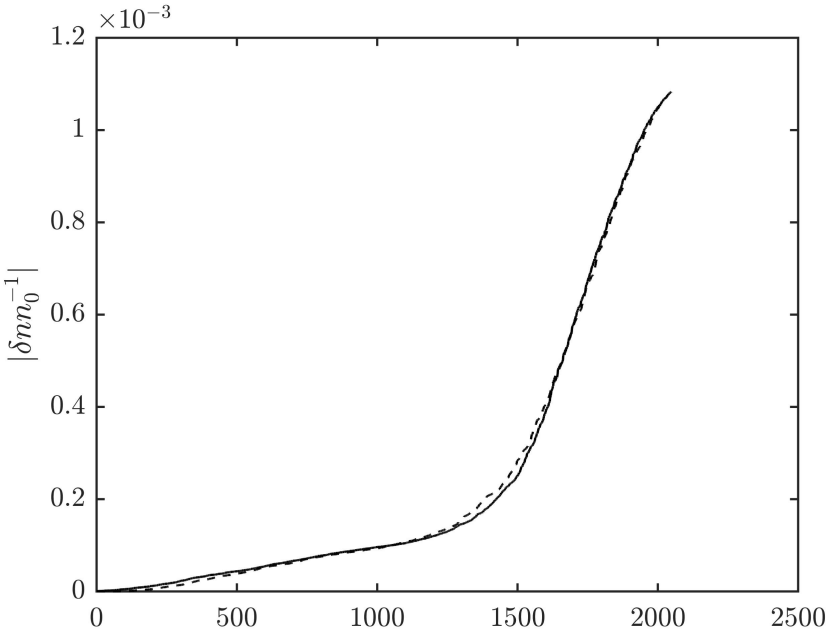


Figure 4.9: The magnitude of the monotonically increasing weak-flow fluctuating density with the predominantly negative (solid) and predominantly positive (dashed) values overlaid. The simulation parameters are as in Section 4.1.

We present the application of our code to the simulation of strong-flow blob transport in the next section.

## 4.2 Blobs

The simulations used $2^{26}$ markers, $N_\mathrm{i} = 16$ and $\Delta t = 1$. The potential was initialised as a dipole. Example potential initialisations are shown in Figures 4.21 and 4.22. We may consider the dipole to be a pair of interacting point vortices with equal but opposite parallel vorticities,

$$\Omega_{\parallel 1} = -\Omega_{\parallel 2}. \tag{4.3}$$

We observe propagation of this dipole, as shown in Figures 4.21 and 4.22.

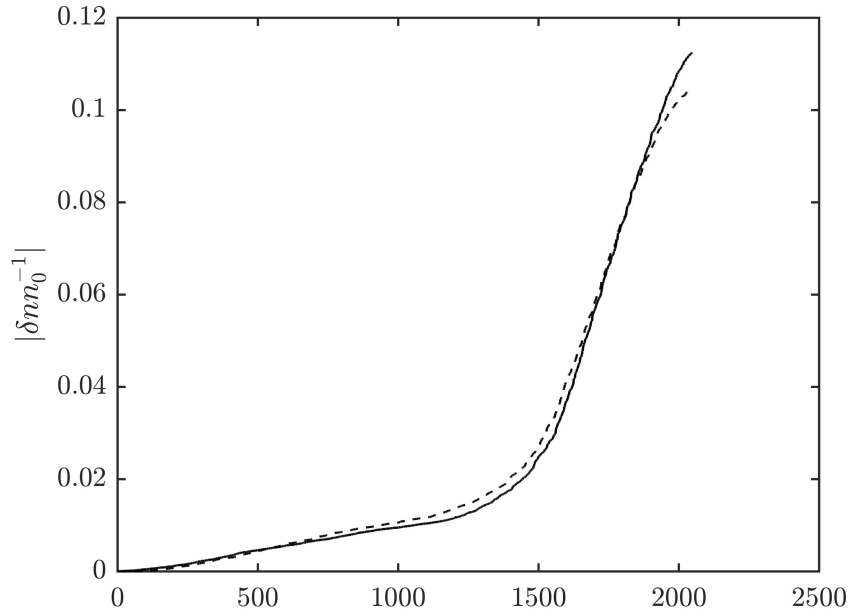


Figure 4.10: The magnitude of the monotonically increasing strong-flow fluctuating density with the predominantly negative (solid) and predominantly positive (dashed) values overlaid. The simulation parameters are as in Section 4.1.

We may write the parallel vorticities (4.3) as the parallel components of curls of velocity fields,

$$\hat{\boldsymbol{b}} \cdot \boldsymbol{\nabla} \times \boldsymbol{v}_1 = -\hat{\boldsymbol{b}} \cdot \boldsymbol{\nabla} \times \boldsymbol{v}_2.$$

We then have that the equal but opposite circulations are given by

$$\int_{\boldsymbol{S}_1} \boldsymbol{\nabla} \times \boldsymbol{v}_1 \cdot \mathrm{d}\boldsymbol{S}_1 = -\int_{\boldsymbol{S}_2} \boldsymbol{\nabla} \times \boldsymbol{v}_2 \cdot \mathrm{d}\boldsymbol{S}_2,$$

where $\boldsymbol{S}_1$ and $\boldsymbol{S}_2$ are surfaces in the $x$-$y$ plane and are enclosed by circles centred around the each respective pole of the dipole. By Stokes' theorem, the circulations may also be given by

$$\oint_{\partial \boldsymbol{S}_1} \boldsymbol{v}_1 \cdot \mathrm{d}\boldsymbol{l}_1 = -\oint_{\partial \boldsymbol{S}_2} \boldsymbol{v}_2 \cdot \mathrm{d}\boldsymbol{l}_2.$$

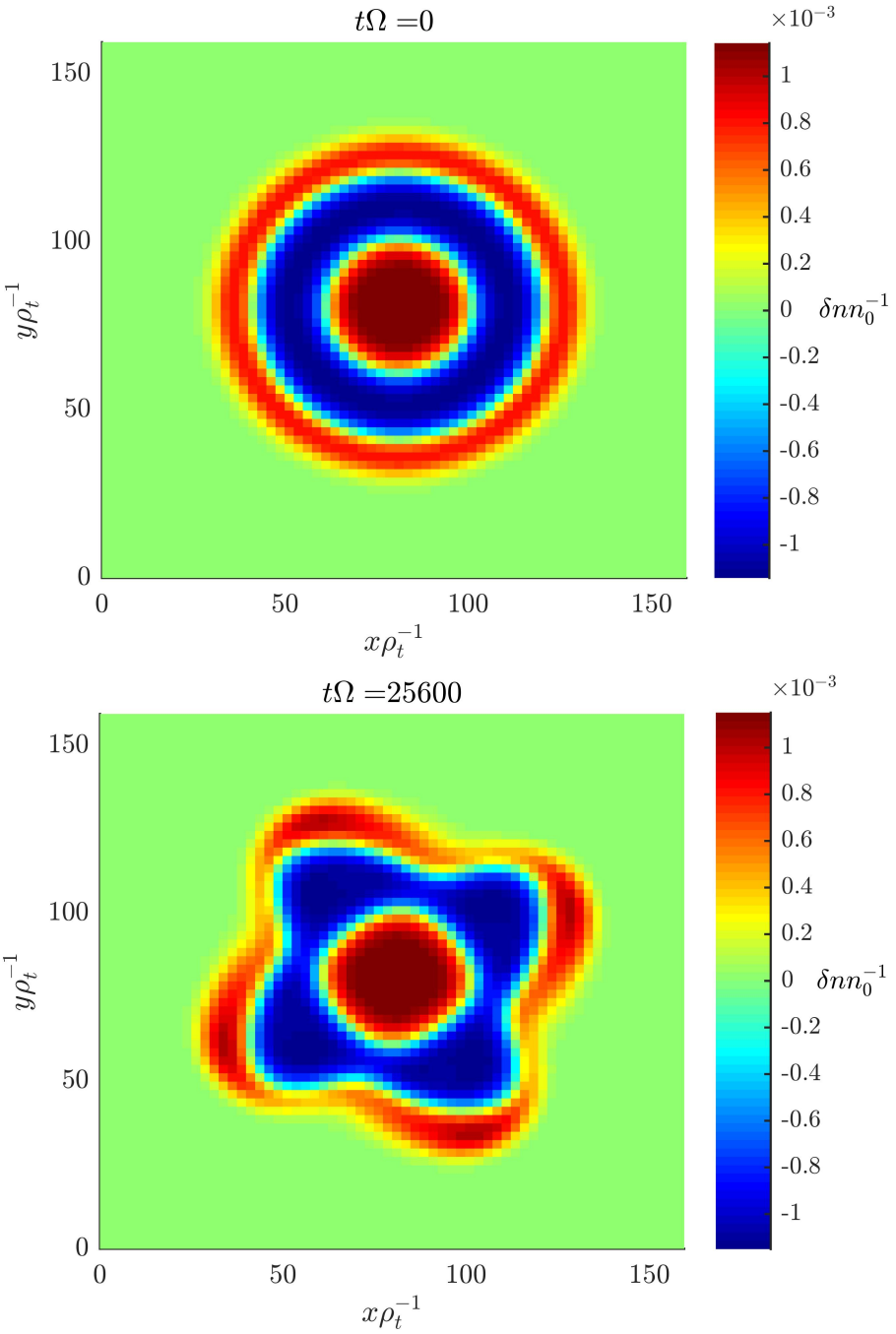


Figure 4.11: The weak-flow, circularly symmetric, Kelvin-Helmholtz unstable shear layer fluctuating density initialisation (top) and evolution (bottom) dominated by positive parallel vorticity on the two-dimensional spatial gyrokinetic simulation domain. The simulation parameters are as in Subsection 4.1.1.

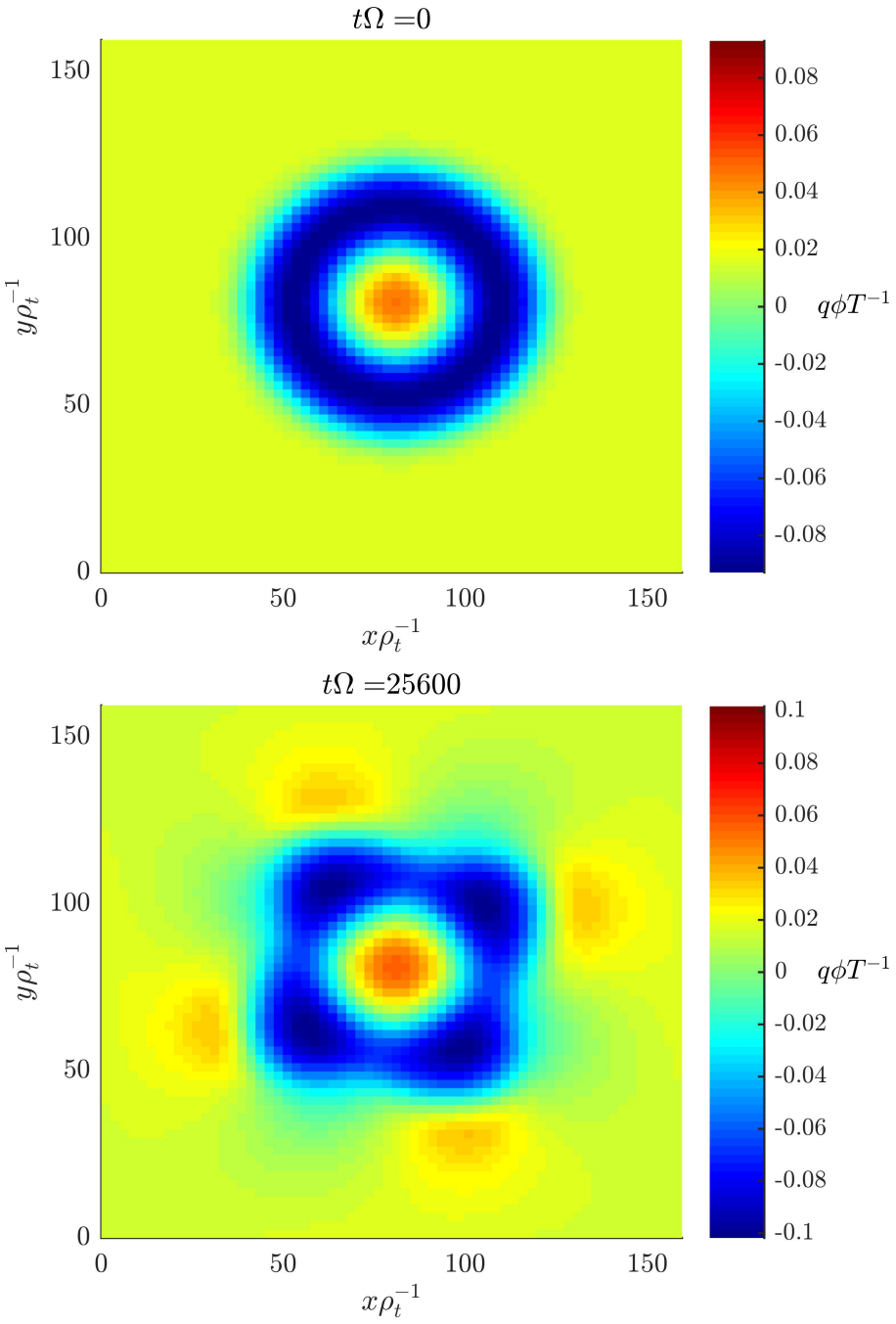


Figure 4.12: The weak-flow, circularly symmetric, Kelvin-Helmholtz unstable shear layer electrostatic potential initialisation (top) and evolution (bottom) dominated by positive parallel vorticity on the two-dimensional spatial gyrokinetic simulation domain. The simulation parameters are as in Subsection 4.1.1.

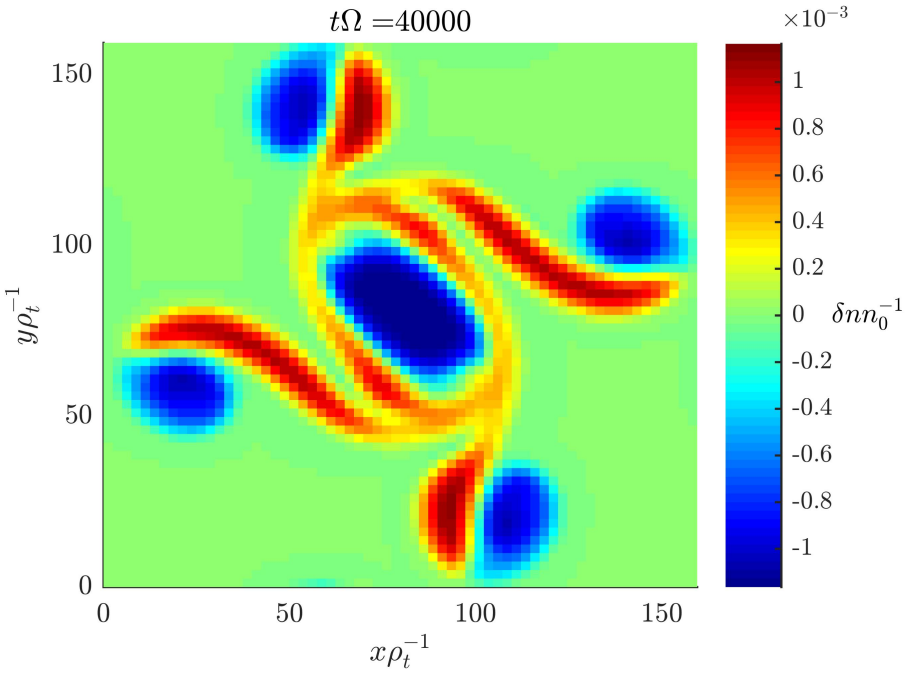


Figure 4.13: The weak-flow fluctuating density on the two-dimensional spatial domain in the nonlinear period of the gyrokinetic simulation of a circularly symmetric, Kelvin-Helmholtz unstable shear layer dominated by positive parallel vorticity. The simulation parameters are as in Subsection 4.1.1.

In terms of azimuthal velocities, with the origin centred on each the vortex,

$$2\pi l_1 v_{1\theta} = -2\pi l_2 v_{2\theta}.$$

We may write these azimuthal velocities in terms of their respective circulations as

$$v_{1\theta} = (2\pi l_1)^{-1} \int_{\boldsymbol{S}_1} \boldsymbol{\nabla} \times \boldsymbol{v}_1 \cdot \mathrm{d}\boldsymbol{S}_1 = -v_{2\theta} = -(2\pi l_2)^{-1} \int_{\boldsymbol{S}_2} \boldsymbol{\nabla} \times \boldsymbol{v}_2 \cdot \mathrm{d}\boldsymbol{S}_2.$$

The corresponding radial velocities are

$$v_{1r} = v_{2r} = 0.$$

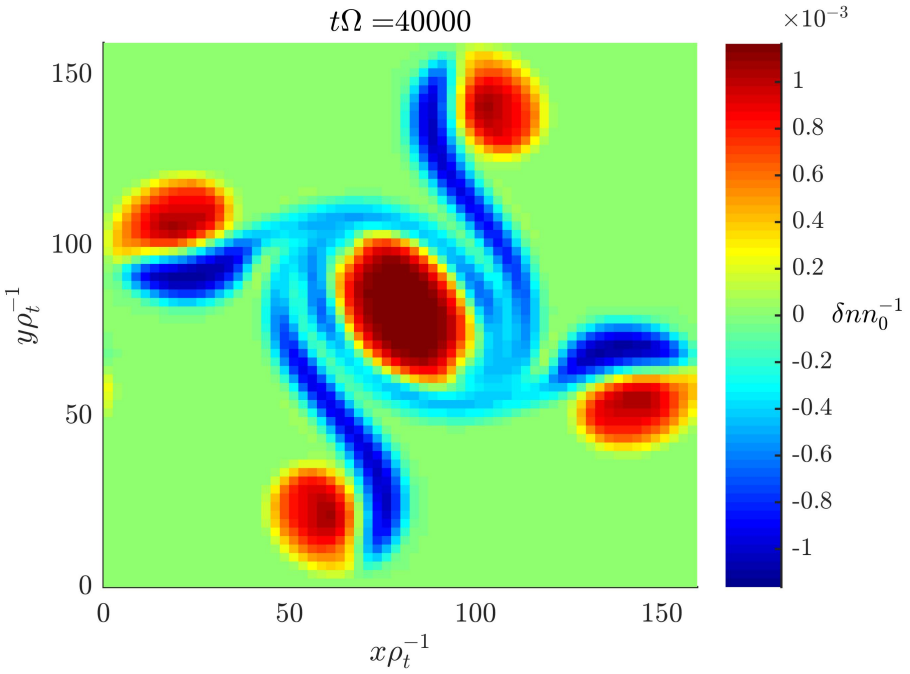


Figure 4.14: The weak-flow fluctuating density on the two-dimensional spatial domain in the nonlinear period of the gyrokinetic simulation of a circularly symmetric, Kelvin-Helmholtz unstable shear layer dominated by negative parallel vorticity. The simulation parameters are as in Subsection 4.1.1.

In other words, we have that each point vortex pulls the other around its centre with equal but opposite azimuthal velocities, resulting in propagation.

For weak flows, the blob travels in a straight line, as shown in Figure 4.23. For the corresponding Cartesian velocities of the point vortices, we have that

$$v_{1x} = v_{2x}$$

and

$$v_{1y} = v_{2y} = 0.$$

For the corresponding blob velocity $\boldsymbol{v}_\mathrm{b}$, we have that

$$\dot{\boldsymbol{v}}_\mathrm{b} = 0,$$

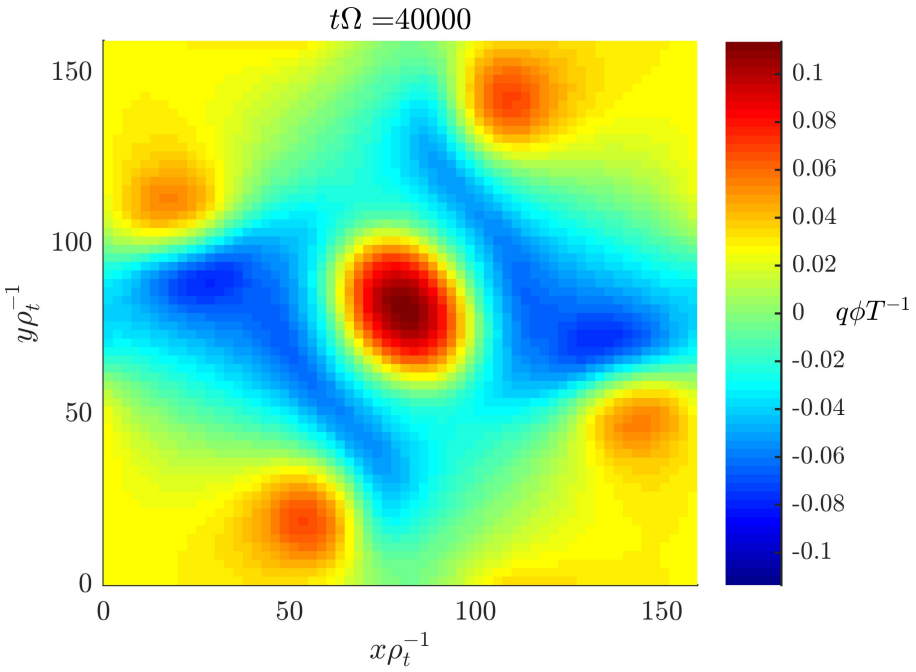


Figure 4.15: The weak-flow fluctuating electrostatic potential on the two-dimensional spatial domain in the nonlinear period of the gyrokinetic simulation of a circularly symmetric, Kelvin-Helmholtz unstable shear layer dominated by positive parallel vorticity. The simulation parameters are as in Subsection 4.1.1.

that is, the blob centre moves with a constant velocity and the each of the vortices do not move relative to the blob centre or each other.

For strong flows, the blob does not travel in a straight line and instead performs circular motion, as shown in Figures 4.22, 4.24 and 4.25. The effects of strong flows manifest as velocity perturbations and shifts in the rotation frequency of each of the point vortices that depend on the sign of the parallel vorticity. This results in azimuthal point vortex velocities that are no longer equal in magnitude. The motion consists of the point centred between the point vortices performing circular motion and the point vortices performing circular motion about this point, with all circular motions having equal angular frequencies.

The simulated radius of curvature of the circular motion of the strong-flow

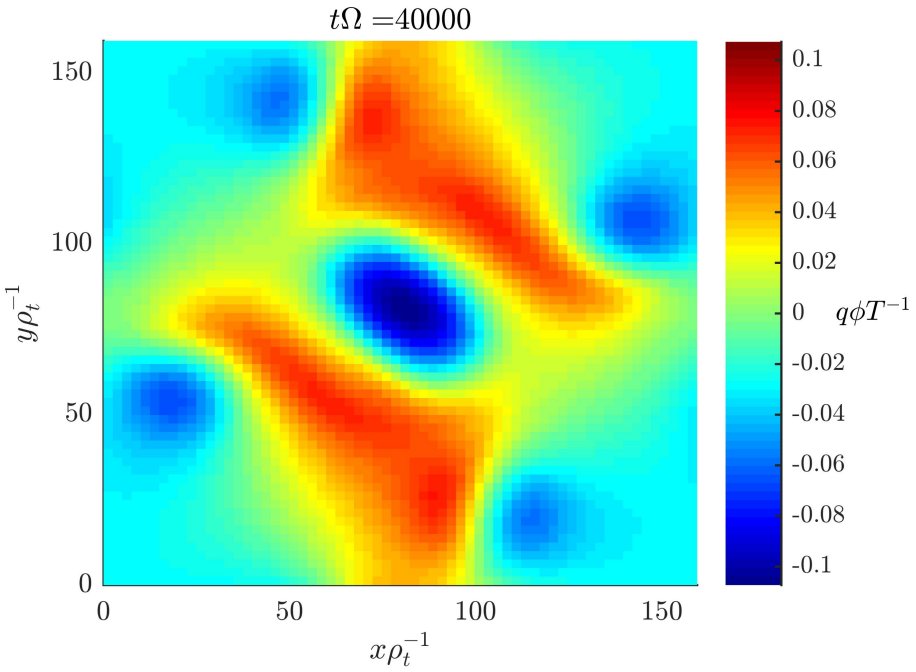


Figure 4.16: The weak-flow fluctuating electrostatic potential on the two-dimensional spatial domain in the nonlinear period of the gyrokinetic simulation of a circularly symmetric, Kelvin-Helmholtz unstable shear layer dominated by negative parallel vorticity. The simulation parameters are as in Subsection 4.1.1.

blob is $2.36 \times 10^3$. By using similar triangles, we may estimate the analytic radius of curvature of the circular motion of our interacting point vortex pair model based on the initialisation of our strong-flow blob simulation (Figure 4.22) as $2.48 \times 10^3$.

We present the conclusion and future scope of this thesis in the next chapter.

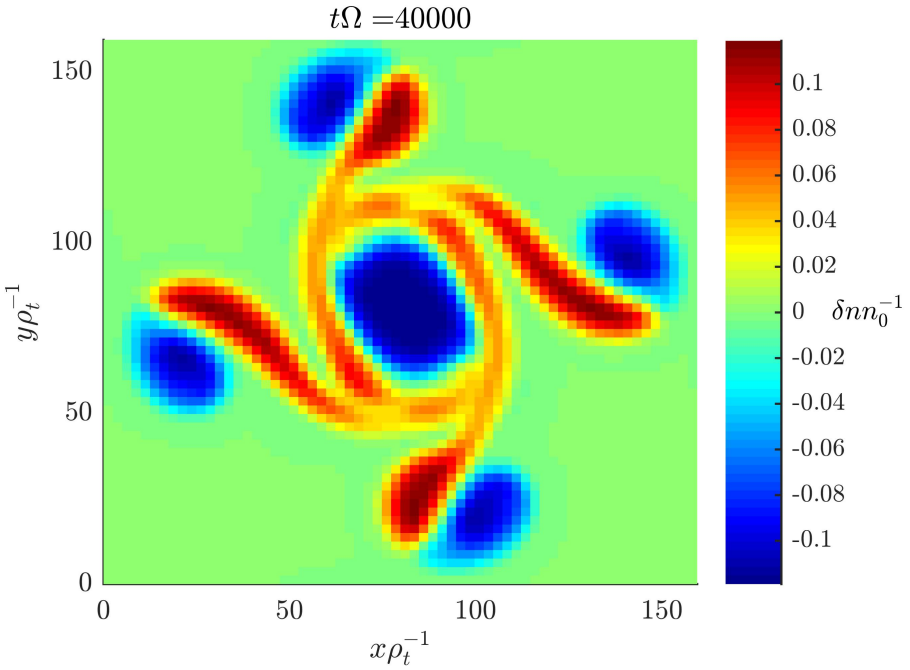


Figure 4.17: The strong-flow fluctuating density on the two-dimensional spatial domain in the nonlinear period of the gyrokinetic simulation of a circularly symmetric, Kelvin-Helmholtz unstable shear layer dominated by positive parallel vorticity. The simulation parameters are as in Subsection 4.1.1.

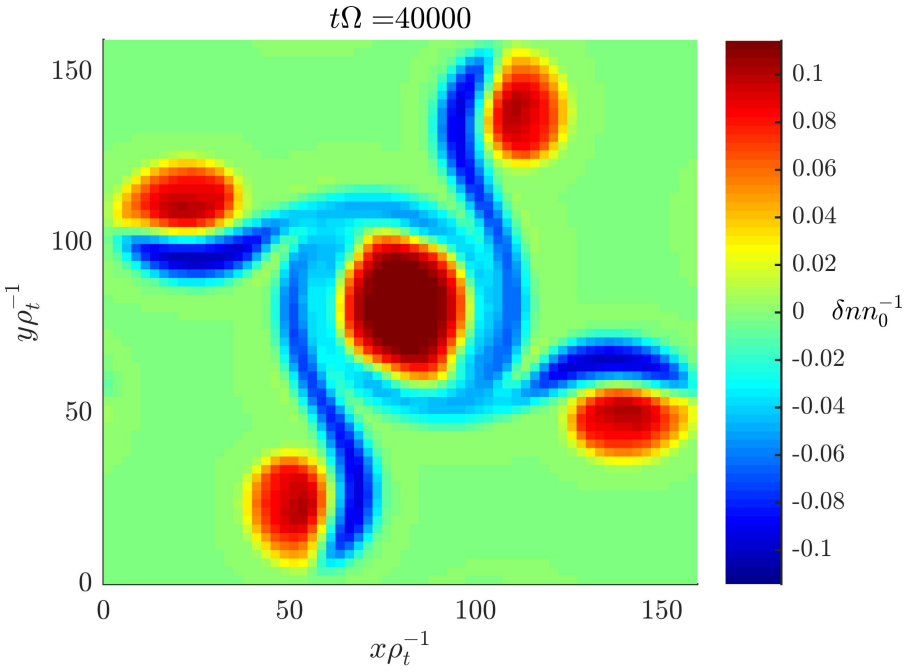


Figure 4.18: The strong-flow fluctuating density on the two-dimensional spatial domain in the nonlinear period of the gyrokinetic simulation of a circularly symmetric, Kelvin-Helmholtz unstable shear layer dominated by negative parallel vorticity. The simulation parameters are as in Subsection 4.1.1.

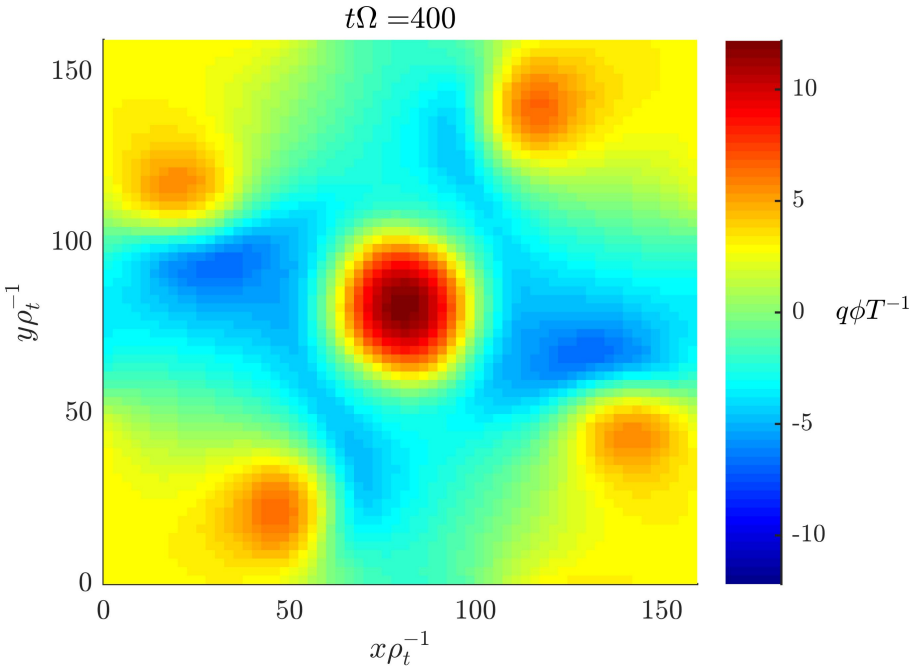


Figure 4.19: The strong-flow fluctuating electrostatic potential on the two-dimensional spatial domain in the nonlinear period of the gyrokinetic simulation of a circularly symmetric, Kelvin-Helmholtz unstable shear layer dominated by positive parallel vorticity. The simulation parameters are as in Subsection 4.1.1.

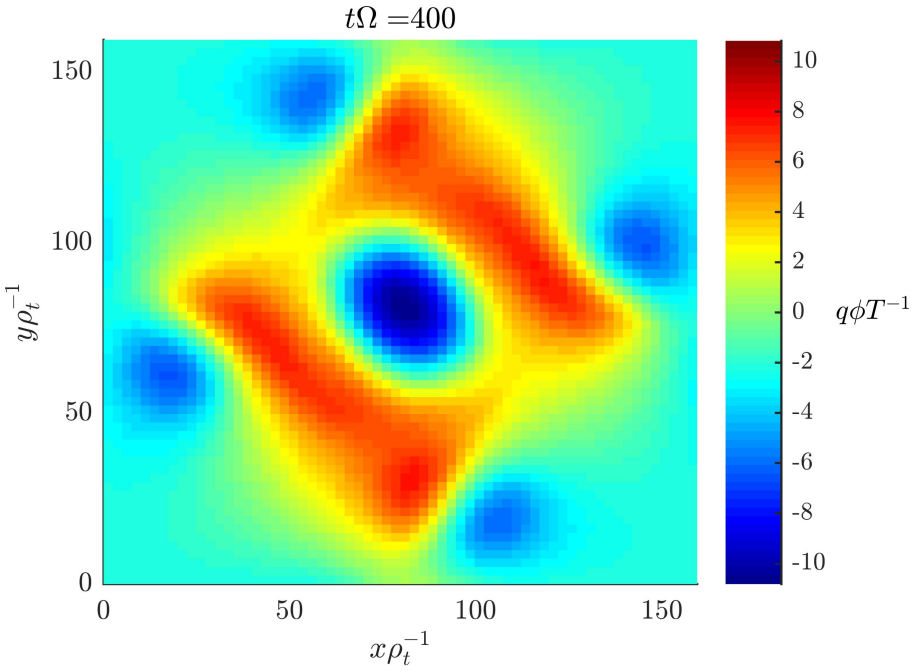


Figure 4.20: The strong-flow fluctuating electrostatic potential on the two-dimensional spatial domain in the nonlinear period of the gyrokinetic simulation of a circularly symmetric, Kelvin-Helmholtz unstable shear layer dominated by negative parallel vorticity. The simulation parameters are as in Subsection 4.1.1.

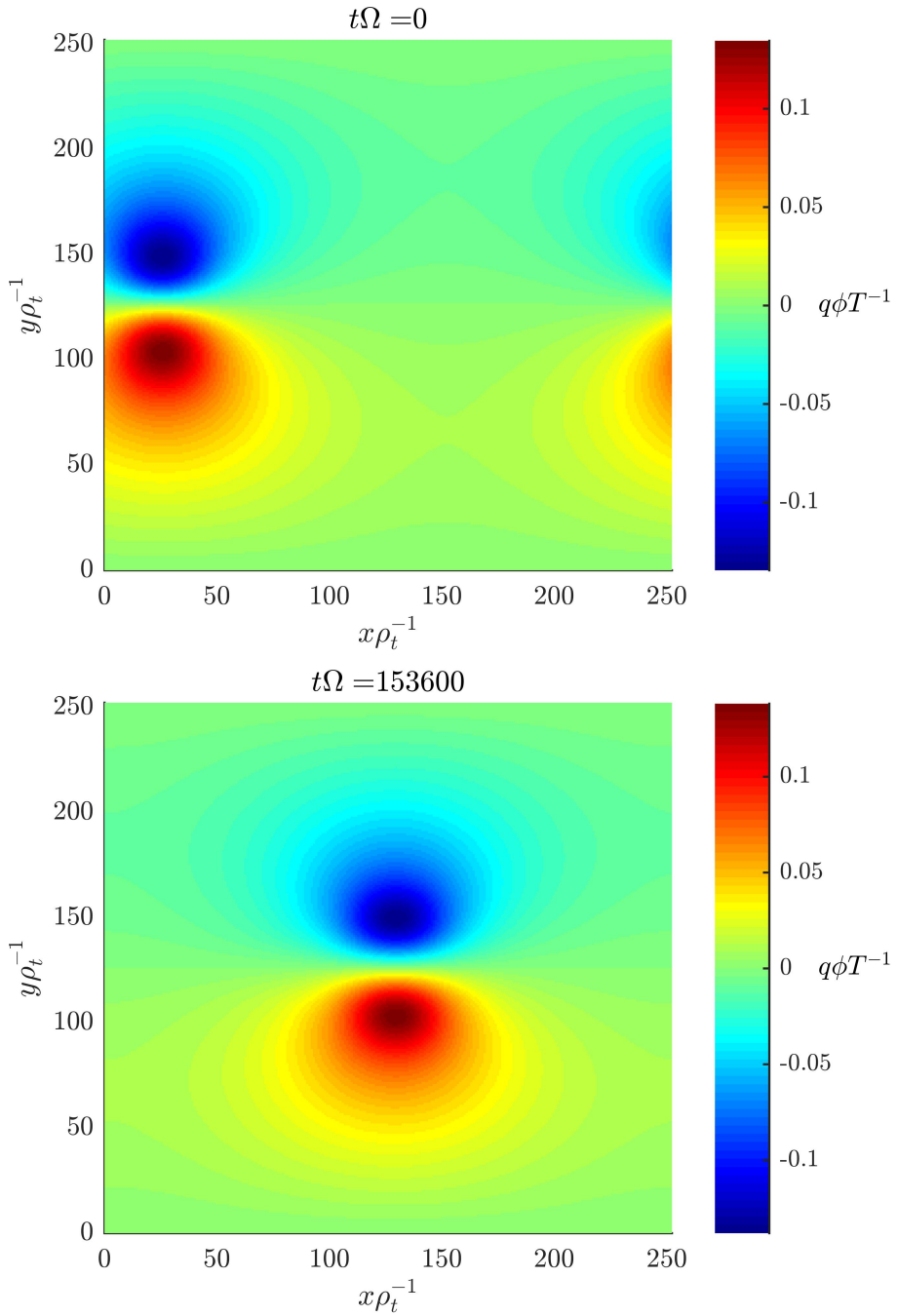


Figure 4.21: The weak-flow dipole fluctuating electrostatic potential blob model initialisation (top) and evolution (bottom) on the two-dimensional spatial gyrokinetic simulation domain. The simulation parameters are as in Subsection 4.2.

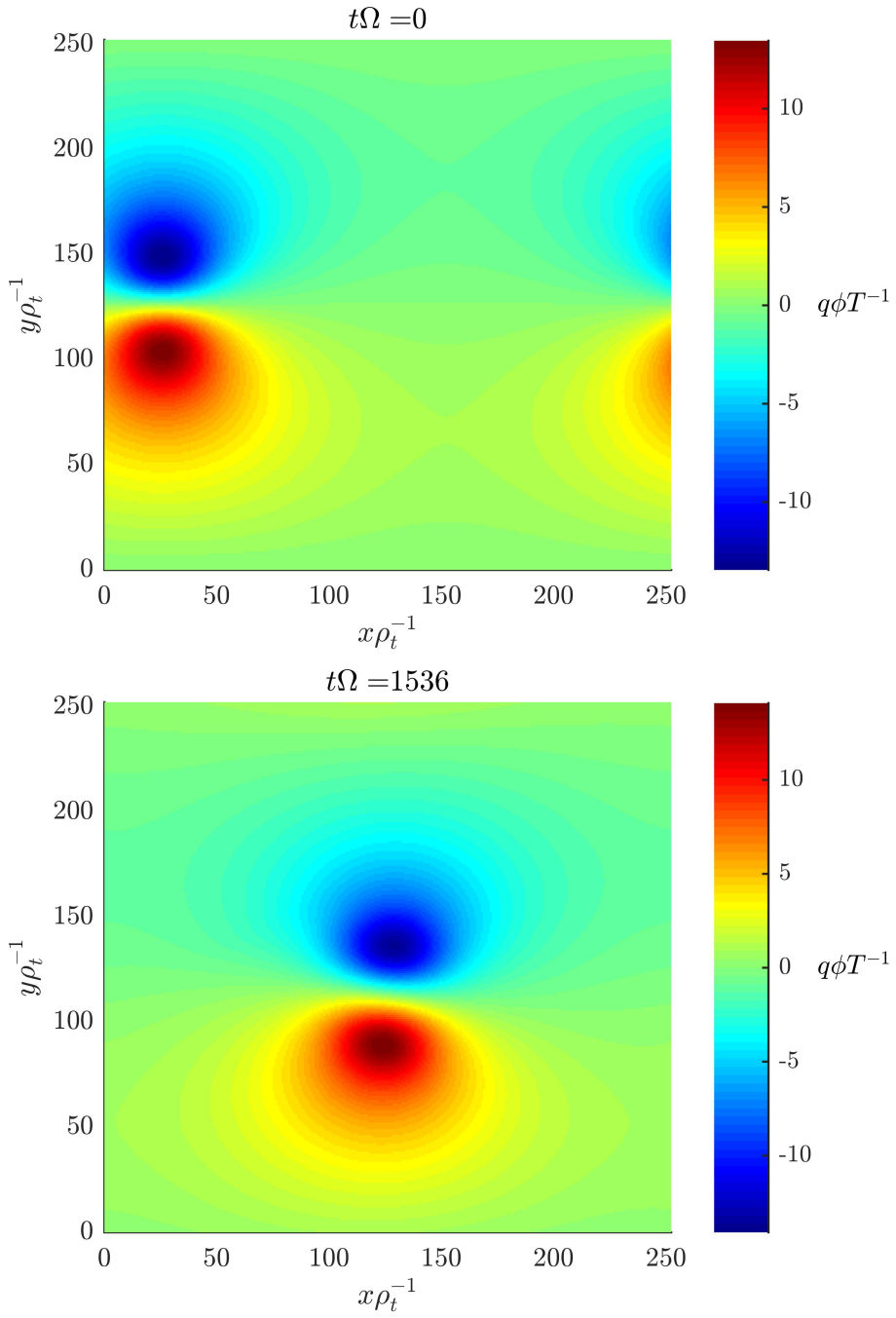


Figure 4.22: The strong-flow dipole fluctuating electrostatic potential blob model initialisation (top) and evolution (bottom) on the two-dimensional spatial gyrokinetic simulation domain. The simulation parameters are as in Subsection 4.2.

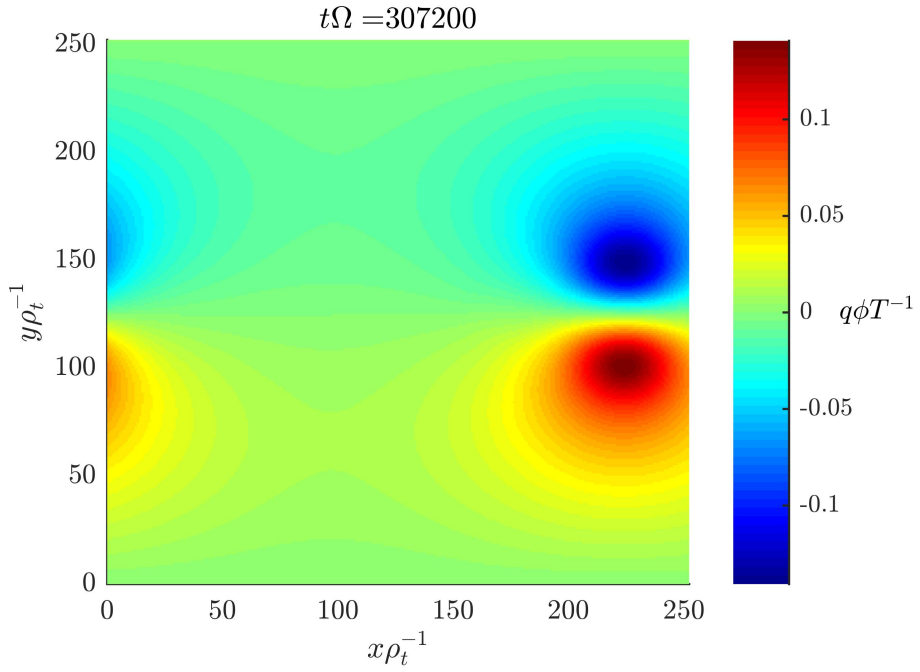


Figure 4.23: The weak-flow dipole fluctuating electrostatic potential blob model on the two-dimensional spatial domain late in gyrokinetic simulation. The simulation parameters are as in Subsection 4.2.

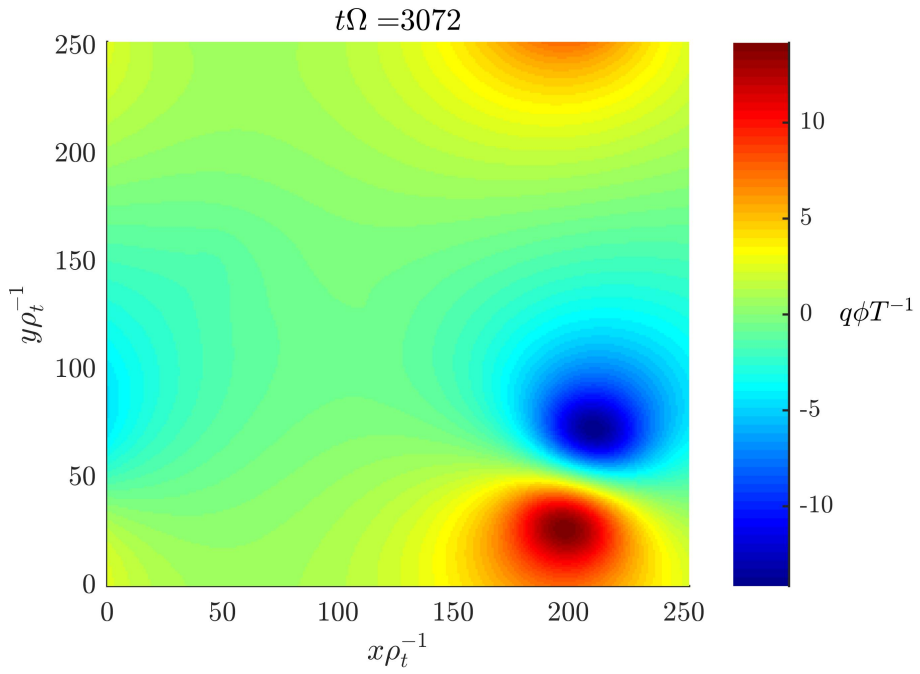


Figure 4.24: The strong-flow dipole fluctuating electrostatic potential blob model on the two-dimensional spatial domain late in the gyrokinetic simulation. The simulation parameters are as in Subsection 4.2.

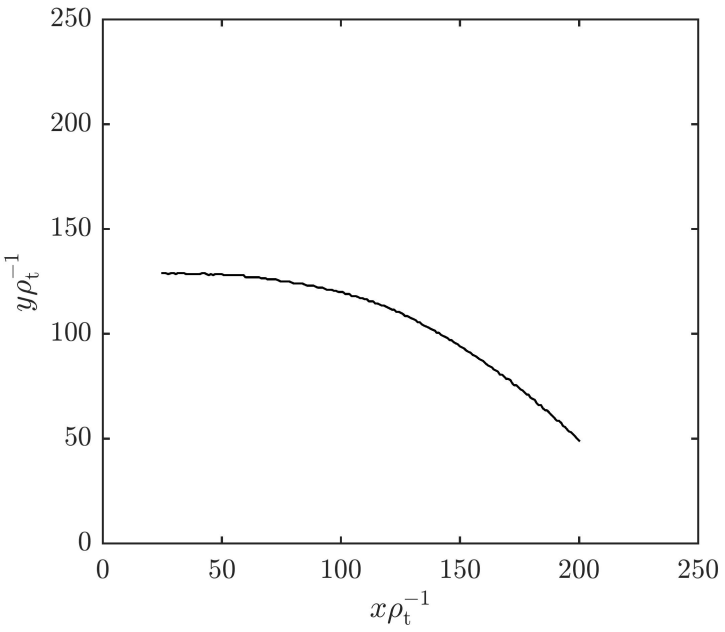


Figure 4.25: The path of the centre of the strong-flow dipole fluctuating electrostatic potential blob model on the two-dimensional spatial domain during the gyrokinetic simulation. The simulation parameters are as in Subsection 4.2.

# Chapter 5

# Conclusion

Gyrokinetics is a maximally optimal description of low-frequency magnetised plasma turbulence.

We have presented a generalisation of gyrokinetic theory that allows dynamic strong flows and is valid for arbitrary wavelength electrostatic potential perturbations in slab magnetic geometry. We have obtained a substantially simpler gyrocentre Lagrangian (2.25) than that of Dimits (2010a,b). We have presented a symplectic strong-flow generalisation of gyrokinetic field theory such that, unlike Dimits (2010a,b), our Vlasov-Poisson system (2.33, 2.34, 2.57, 2.69) is manifestly conservative as, ultimately, we obtain it as a whole, directly from our gyrocentre particle Lagrangian (2.25) (Scott and Smirnov, 2010). Despite the symplectic representation of our strong-flow theory, our Poisson equation (2.57) is consistent with that for weak flows (Hahm, 1988) at all wavelengths and the fluid equation (2.74) obtained from our Vlasov-Poisson system is consistent with fluid theory.

Again, despite our symplectic representation, we have demonstrated numerical tractability by solving implicit dependences using an iterative scheme. Weak- and strong-flow code verification have been performed in limits that admit analytic comparison.

Simulations show strong-flow symmetry breaking of the Kelvin-Helmholtz in-

stability of a shear layer and blobs that manifest as asymmetries in the growth rate and propagation, respectively, that depend on the sign of the parallel vorticity.

We discuss the future scope of this thesis in the next section.

## 5.1 Future scope

The implementation of the gyrokinetic theory presented here in global gyrokinetic codes such as ORB5 (Jolliet et al., 2007) would require a generalisation of the theory to allow the treatment of electromagnetic potential perturbations in general magnetic geometry. This is being pursued for the case with a velocity-independent $\bar{\boldsymbol{u}}$ (Sharma and McMillan, 2015b).

The Hamiltonian representation of the strong-flow theory of Miyato et al. (2009) admits proof of toroidal momentum conservation (Scott and Smirnov, 2010). A Hamiltonian formulation of our theory could be considered.

An improvement in our electron model and an extension of the code to three spatial dimensions would allow full drift instability simulations to be performed.

We have used a spectral method for our field solver. Alternatively, an intrinsically conservative, arbitrary-wavelength finite-element method may be used (Dominski et al., 2014).

Additionally, the iterative numerical scheme presented here may be generalised by incorporating $\delta\bar{F}'$ polarisation.

Finally, this thesis, and work derived from it, may lead to a fusion energy solution.

# Bibliography

Y. Andrew, N. C. Hawkes, T. Biewer, K. Crombe, D. Keeling, E. de la Luna, C. Giroud, A. Korotkov, A. Meigs, A. Murari, I. Nunes, R. Sartori, T. Tala, and J.-E. Contributors. Evolution of the radial electric field in a JET H-mode plasma. *EPL (Europhysics Letters)*, 83(1):15003, 2008. URL http://stacks.iop.org/0295-5075/83/i=1/a=15003.

M. Artun and W. M. Tang. Nonlinear electromagnetic gyrokinetic equations for rotating axisymmetric plasmas. *Physics of Plasmas (1994-present)*, 1 (8):2682–2692, 1994. doi: http://dx.doi.org/10.1063/1.870595. URL http://scitation.aip.org/content/aip/journal/pop/1/8/10.1063/1.870595.

A. J. Brizard. Nonlinear gyrokinetic Maxwell-Vlasov equations using magnetic co-ordinates. *Journal of Plasma Physics*, 41:541–559, 6 1989. ISSN 1469-7807. doi: 10.1017/S0022377800014070. URL http://journals.cambridge.org/article_S0022377800014070.

A. J. Brizard. *Nonlinear gyrokinetic tokamak physics*. PhD thesis, Princeton Univ., NJ (United States), 1990. URL http://academics.smcvt.edu/abrizard/phd_files/Dissertation.pdf.

A. J. Brizard. Nonlinear gyrokinetic Vlasov equation for toroidally rotating axisymmetric tokamaks. *Phys. Plasmas*, 2(2):459–471, 1995. doi: 10.1063/1.871465. URL http://scitation.aip.org/content/aip/journal/pop/2/2/10.1063/1.871465.

A. J. Brizard. Variational principle for nonlinear gyrokinetic Vlasov-Maxwell equations. *Physics of Plasmas (1994-present)*, 7(12):4816–4822, 2000. doi: http://dx.doi.org/10.1063/1.1322063. URL http://scitation.aip.org/content/aip/journal/pop/7/12/10.1063/1.1322063.

A. J. Brizard and T. Hahm. Foundations of nonlinear gyrokinetic theory. *Rev. Mod. Phys.*, 79(2):421–468, Apr. 2007. ISSN 0034-6861. doi: 10.1103/RevModPhys.79.421. URL http://rmp.aps.org/abstract/RMP/v79/i2/p421_1.

A. J. Brizard and N. Tronko. Exact momentum conservation laws for the gyrokinetic Vlasov-Poisson equations. *Physics of Plasmas (1994-present)*, 18(8):082307, 2011. doi: http://dx.doi.org/10.1063/1.3625554. URL http://scitation.aip.org/content/aip/journal/pop/18/8/10.1063/1.3625554.

J. Candy. GYRO code, Fusion Theory and Computational Sciences, General Atomics, August 2008. URL https://fusion.gat.com/theory-wiki/images/a/a4/Supertorus-hi-2.jpg.

J. R. Cary. Lie transform perturbation theory for Hamiltonian systems. *Physics Reports*, 79(2):129 – 159, 1981. ISSN 0370-1573. doi: http://dx.doi.org/10.1016/0370-1573(81)90175-7. URL http://www.sciencedirect.com/science/article/pii/0370157381901757.

J. R. Cary and A. J. Brizard. Hamiltonian theory of guiding-center motion. *Rev. Mod. Phys.*, 81:693–738, May 2009. doi: 10.1103/RevModPhys.81.693. URL http://link.aps.org/doi/10.1103/RevModPhys.81.693.

J. R. Cary and R. G. Littlejohn. Noncanonical Hamiltonian mechanics and its application to magnetic field line flow. *Ann. Phys. (N. Y).*, 151(1):1–34, Nov. 1983. ISSN 00034916. doi: 10.1016/0003-4916(83)90313-5. URL http://www.sciencedirect.com/science/article/pii/0003491683903135.

P. H. Diamond, S.-I. Itoh, K. Itoh, and T. S. Hahm. Zonal flows in plasma-

a review. *Plasma Physics and Controlled Fusion*, 47(5):R35, 2005. URL http://stacks.iop.org/0741-3335/47/i=5/a=R01.

A. M. Dimits. Gyrokinetic equations in an extended ordering. *Phys. Plasmas*, 17(5):055901, Mar. 2010a. ISSN 1070664X. doi: 10.1063/1.3327211. URL http://scitation.aip.org/content/aip/journal/pop/17/5/10.1063/1.3327211.

A. M. Dimits. Global gyrokinetic equations: extended orderings and second-order terms. *Gyrokinetics in Laboratory and Astrophysical Plasmas, Cambridge*, Aug. 2010b. URL http://www-thphys.physics.ox.ac.uk/research/plasma/ukgk_pdfs/dimits_wk4.pdf.

A. M. Dimits, L. L. LoDestro, and D. H. E. Dubin. Gyroaveraged equations for both the gyrokinetic and drift-kinetic regimes. *Phys. Fluids B*, 4(1):274, Jan. 1992. ISSN 08998221. doi: 10.1063/1.860444. URL http://scitation.aip.org/content/aip/journal/pofb/4/1/10.1063/1.860444.

J. Dominski, S. Brunner, B. F. McMillan, T.-M. Tran, and L. Villard. An arbitrary-wavelength solver for the gyrokinetic quasi-neutrality equation. *19th Joint EU-US Transport Task Force Meeting, Culham*, 2014. URL http://www.ttf2014.org/wp-content/uploads/2014/01/dominski_ttf2014.pdf.

D. H. E. Dubin, J. A. Krommes, C. Oberman, and W. W. Lee. Nonlinear gyrokinetic equations. *Phys. Fluids*, 26(12):3524, Dec. 1983. ISSN 00319171. doi: 10.1063/1.864113. URL http://scitation.aip.org/content/aip/journal/pof1/26/12/10.1063/1.864113.

EUROfusion. Fusion Electricity: A roadmap to the realisation of fusion energy, January 2013. URL http://www.euro-fusion.org/wpcms/wp-content/uploads/2013/02/JG12.356-web.pdf.

M. Frigo and S. Johnson. The Design and Implementation of FFTW3. *Proceedings of the IEEE*, 93(2):216–231, Feb 2005. ISSN 0018-9219. doi: 10.1109/JPROC.2004.840301. URL http://ieeexplore.ieee.org/xpl/articleDetails.jsp?arnumber=1386650.

X. Garbet, Y. Idomura, L. Villard, and T. Watanabe. Gyrokinetic simulations of turbulent transport. *Nuclear Fusion*, 50(4):043002, 2010. URL http://stacks.iop.org/0029-5515/50/i=4/a=043002.

O. E. Garcia. Blob Transport in the Plasma Edge: a Review. *Plasma and Fusion Research*, 4:019–019, 2009. doi: 10.1585/pfr.4.019. URL https://www.jstage.jst.go.jp/article/pfr/4/0/4_0_019/_pdf.

P. W. Gingell, S. C. Chapman, R. O. Dendy, and C. S. Brady. Transport and evolution of ion gyro-scale plasma blobs in perpendicular magnetic fields. *Plasma Physics and Controlled Fusion*, 54(6):065005, 2012. URL http://stacks.iop.org/0741-3335/54/i=6/a=065005.

T. S. Hahm. Nonlinear gyrokinetic equations for tokamak microturbulence. *Phys. Fluids*, 31(9):2670–2673, 1988. ISSN 00319171. doi: 10.1063/1.866544. URL http://scitation.aip.org/content/aip/journal/pof1/31/9/10.1063/1.866544.

T. S. Hahm. Nonlinear gyrokinetic equations for turbulence in core transport barriers. *Phys. Plasmas*, 3(12):4658, Dec. 1996. ISSN 1070664X. doi: 10.1063/1.872034. URL http://scitation.aip.org/content/aip/journal/pop/3/12/10.1063/1.872034.

T. S. Hahm, W. W. Lee, and A. Brizard. Nonlinear gyrokinetic theory for finite-beta plasmas. *Physics of Fluids (1958-1988)*, 31(7):1940–1948, 1988. doi: http://dx.doi.org/10.1063/1.866641. URL http://scitation.aip.org/content/aip/journal/pof1/31/7/10.1063/1.866641.

T. S. Hahm, L. Wang, and J. Madsen. Fully electromagnetic nonlinear gyrokinetic equations for tokamak edge turbulence. *Physics of Plasmas (1994-present)*, 16(2):022305, 2009. doi: http://dx.doi.org/10.1063/1.3073671. URL http://scitation.aip.org/content/aip/journal/pop/16/2/10.1063/1.3073671.

A. Hasegawa and K. Mima. Stationary Spectrum of Strong Turbulence in Magnetized Nonuniform Plasma. *Phys. Rev. Lett.*, 39:205–208, Jul 1977.

doi: 10.1103/PhysRevLett.39.205. URL http://link.aps.org/doi/10.1103/PhysRevLett.39.205.

R. Hatzky, T. M. Tran, A. Knies, R. Kleiber, and S. J. Allfrey. Energy conservation in a nonlinear gyrokinetic particle-in-cell code for ion-temperature-gradient-driven modes in $\theta$-pinch geometry. *Physics of Plasmas (1994-present)*, 9(3):898–912, 2002. doi: http://dx.doi.org/10.1063/1.1449889. URL http://scitation.aip.org/content/aip/journal/pop/9/3/10.1063/1.1449889.

E. Holzhauer, G. Dodel, M. Endler, J. Gernhardt, L. Giannone, M. Manso, K. McCormick, V. Mertens, H. Niedermeyer, A. Rudyj, F. Serra, A. Silva, G. Theimer, P. Varela, F. Wagner, and H. Zohm. The H-mode in the ASDEX tokamak. *Plasma Physics and Controlled Fusion*, 36(7A):A3, 1994. URL http://stacks.iop.org/0741-3335/36/i=7A/a=001.

W. Horton. Drift waves and transport. *Rev. Mod. Phys.*, 71:735–778, Apr 1999. doi: 10.1103/RevModPhys.71.735. URL http://link.aps.org/doi/10.1103/RevModPhys.71.735.

W. Horton and A. Hasegawa. Quasi-two-dimensional dynamics of plasmas and fluids. *Chaos: An Interdisciplinary Journal of Nonlinear Science*, 4(2):227–251, 1994. doi: http://dx.doi.org/10.1063/1.166049. URL http://scitation.aip.org/content/aip/journal/chaos/4/2/10.1063/1.166049.

ITER. Chapter 1: Overview and summary. *Nuclear Fusion*, 39(12):2137, 1999a. doi: http://dx.doi.org/10.1088/0029-5515/39/12/301. URL http://stacks.iop.org/0029-5515/39/i=12/a=301.

ITER. Chapter 2: Plasma confinement and transport. *Nuclear Fusion*, 39 (12):2175, 1999b. doi: http://dx.doi.org/10.1088/0029-5515/39/12/302. URL http://stacks.iop.org/0029-5515/39/i=12/a=302.

S. Jolliet. *Gyrokinetic particle-in-cell global simulations of ion-temperature-gradient and collisionless-trapped-electron-mode turbulence in tokamaks*. PhD

thesis, CRPP, EPFL, Lausanne, 2009. URL http://infoscience.epfl.ch/record/130837/files/EPFL_TH4326.pdf.

S. Jolliet, A. Bottino, P. Angelino, R. Hatzky, T. M. Tran, B. F. McMillan, O. Sauter, K. Appert, Y. Idomura, and L. Villard. A global collisionless PIC code in magnetic coordinates. *Comput. Phys. Commun.*, 177(5):409–425, Sept. 2007. ISSN 00104655. doi: 10.1016/j.cpc.2007.04.006. URL http://www.sciencedirect.com/science/article/pii/S0010465507002251.

N. Katz, J. Egedal, W. Fox, A. Le, and M. Porkolab. Experiments on the Propagation of Plasma Filaments. *Phys. Rev. Lett.*, 101:015003, Jul 2008. doi: 10.1103/PhysRevLett.101.015003. URL http://link.aps.org/doi/10.1103/PhysRevLett.101.015003.

G. Kawamura and A. Fukuyama. Refinement of the gyrokinetic equations for edge plasmas with large flow shears. *Physics of Plasmas (1994-present)*, 15 (4):042304, 2008. doi: http://dx.doi.org/10.1063/1.2902016. URL http://scitation.aip.org/content/aip/journal/pop/15/4/10.1063/1.2902016.

A. Kirk. EUROfusion, Jun 2012. URL https://www.euro-fusion.org/wpcms/wp-content/uploads/2012/06/MAST-ELM_web_2.jpg.

S. Krasheninnikov. On scrape off layer plasma transport. *Physics Letters A*, 283(56):368 – 370, 2001. ISSN 0375-9601. doi: http://dx.doi.org/10.1016/S0375-9601(01)00252-3. URL http://www.sciencedirect.com/science/article/pii/S0375960101002523.

J. A. Krommes. Nonlinear gyrokinetics: a powerful tool for the description of microturbulence in magnetized plasmas. *Physica Scripta*, 2010(T142):014035, 2010. URL http://stacks.iop.org/1402-4896/2010/i=T142/a=014035.

J. A. Krommes. The gyrokinetic description of microturbulence in magnetized plasmas. *Annual Review of Fluid Mechanics*, 44(1):175–201, 2012. doi: 10.1146/annurev-fluid-120710-101223. URL http://dx.doi.org/10.1146/annurev-fluid-120710-101223.

W. W. Lee. Gyrokinetic approach in particle simulation. *Physics of Fluids*, 26(2):556–562, 1983. doi: http://dx.doi.org/10.1063/1.864140. URL http://scitation.aip.org/content/aip/journal/pof1/26/2/10.1063/1.864140.

R. G. Littlejohn. Hamiltonian perturbation theory in noncanonical coordinates. *J. Math. Phys.*, 23(5):742, May 1982. ISSN 00222488. doi: 10.1063/1.525429. URL http://scitation.aip.org/content/aip/journal/jmp/23/5/10.1063/1.525429.

R. G. Littlejohn. Variational principles of guiding centre motion. *Journal of Plasma Physics*, 29:111–125, 2 1983. ISSN 1469-7807. doi: 10.1017/S002237780000060X. URL http://journals.cambridge.org/article_S002237780000060X.

J. Madsen. *Guiding-center models for edge plasmas and numerical simulations of isolated plasma filaments*. PhD thesis, Danmarks Tekniske Universitet, Ris Nationallaboratoriet for Bredygtig Energi, 2010. URL http://orbit.dtu.dk/fedora/objects/orbit:82342/datastreams/file_4894853/content.

J. Madsen. Private communication, 2011.

N. Miyato, B. D. Scott, D. Strintzi, and S. Tokuda. A Modification of the Guiding-Centre Fundamental 1-Form with Strong E×B Flow. *J. Phys. Soc. Jpn.*, 78(10):104501, 2009. doi: 10.1143/JPSJ.78.104501. URL http://dx.doi.org/10.1143/JPSJ.78.104501.

P. J. Morrison. Hamiltonian and action principle formulations of plasma physics. *Physics of Plasmas (1994-present)*, 12(5):058102, 2005. doi: http://dx.doi.org/10.1063/1.1882353. URL http://scitation.aip.org/content/aip/journal/pop/12/5/10.1063/1.1882353.

H. Nagano. Effect of finite ion Larmor radius on the Kelvin-Helmholtz instability. *Journal of Plasma Physics*, 20:149–160, 10 1978. ISSN 1469-7807. doi: 10.1017/S0022377800021450. URL http://journals.cambridge.org/article_S0022377800021450.

V. Naulin. Turbulent transport and the plasma edge. *Journal of Nuclear Materials*, 363365:24 – 31, 2007. ISSN 0022-3115. doi: http://dx.doi.org/10.1016/j.jnucmat.2006.12.058. URL http://www.sciencedirect.com/science/article/pii/S0022311506006301. Plasma-Surface Interactions-17.

H. Qin, R. H. Cohen, W. M. Nevins, and X. Q. Xu. Geometric gyrokinetic theory for edge plasmas. *Phys. Plasmas*, 14(5):056110, 2007. doi: 10.1063/1.2472596. URL http://scitation.aip.org/content/aip/journal/pop/14/5/10.1063/1.2472596.

E. Rafajłowicz and R. Schwabe. Halton and Hammersley sequences in multivariate nonparametric regression. *Statistics & Probability Letters*, 76(8):803 – 812, 2006. ISSN 0167-7152. doi: http://dx.doi.org/10.1016/j.spl.2005.10.014. URL http://www.sciencedirect.com/science/article/pii/S0167715205003895.

B. N. Rogers and W. Dorland. Noncurvature-driven modes in a transport barrier. *Physics of Plasmas (1994-present)*, 12(6):062511, 2005. doi: http://dx.doi.org/10.1063/1.1928250. URL http://scitation.aip.org/content/aip/journal/pop/12/6/10.1063/1.1928250.

B. Scott. Energetic Consistency and Symmetry in Gyrokinetic Field Theory. *15th European Fusion Theory Conference, Merton College, Oxford, UK*, 1, September 2013. URL http://www.eftc2013.org.uk/presentations_chad/Scott/EFTC13.pdf.

B. Scott and J. Smirnov. Energetic consistency and momentum conservation in the gyrokinetic description of tokamak plasmas. *Phys. Plasmas*, 17(11):112302, Nov. 2010. ISSN 1070664X. doi: 10.1063/1.3507920. URL http://link.aip.org/link/?PHPAEN/17/112302/1.

A. Y. Sharma and B. F. McMillan. A reanalysis of a strong-flow gyrokinetic formalism. *Physics of Plasmas (1994-present)*, 22(3):032510, 2015a. doi: http://dx.doi.org/10.1063/1.4916129. URL http://scitation.aip.org/content/aip/journal/pop/22/3/10.1063/1.4916129.

A. Y. Sharma and B. F. McMillan. Implementation and application of an elegant strong-flow gyrokinetic formalism. *42nd European Physical Society Conference on Plasma Physics*, O4.406, 2015b. URL http://ocs.ciemat.es/EPS2015ABS/pdf/O4.406.pdf.

H. Sugama. Gyrokinetic field theory. *Physics of Plasmas (1994-present)*, 7 (2):466–480, 2000. doi: http://dx.doi.org/10.1063/1.873832. URL http://scitation.aip.org/content/aip/journal/pop/7/2/10.1063/1.873832.

L. Wang and T. S. Hahm. Nonlinear gyrokinetic theory with polarization drift. *Physics of Plasmas*, 17(8):082304, 2010. doi: http://dx.doi.org/10.1063/1.3467498. URL http://scitation.aip.org/content/aip/journal/pop/17/8/10.1063/1.3467498.